A study of heavy flavour production at centre–of–mass energies between 183 and 207 GeV

E Brodet

DELPHI experiment, CERN

A thesis submitted for the
degree of Doctor of Philosophy
at the University of Oxford

2004

A study of $e^+e^- \to Z^0/\gamma \to q\bar{q}$ at centre–of–mass energies between 183 and 207 GeV

Eyal Brodet

Submitted for the degree of Doctor of Philosophy

at the University of Oxford

Trinity term, 2004

Abstract

The data used in this thesis are taken from the period LEP ran at centre-of-mass energies between 183 and 207 GeV. These data have been used to study the Forward-Backward asymmetry of b and c quarks through the process $e^+e^- \to Z^0/\gamma \to q\bar{q}$. The asymmetry measurements showed no deviations from the Standard Model expectations as can be seen from the results of a χ^2 fit between the asymmetry results and the Standard Model values(ΔA_{FB}):

$$\Delta A^b_{FB} = -0.089 \pm 0.076.$$

$$\Delta A^c_{FB} = -0.116 \pm 0.143.$$

The results obtained are used to set limits on possible forms of contact interactions.

Contents

Preface

The data used in this thesis are taken from the period LEP ran at centre of mass energies between 183 and 207 GeV. These data allow the Standard Model of particle physics, in particular the processes involving the production of quarks through the process $e^+e^- \rightarrow Z^0/\gamma \rightarrow q\bar{q}(\gamma)$, to be tested in regions not accessible before. This thesis is primarily concerned with the measurement of the Forward Backward asymmetry of b and c quarks, A^b_{FB} and A^c_{FB}. Chapter 1 is a short introduction to the Standard Model of particle physics, giving particular emphasis to the process $e^+e^- \rightarrow Z^0/\gamma \rightarrow q\bar{q}$ and the asymmetry in the quarks production.

Chapter 2 is a short description of the LEP accelerator and the DELPHI detector. The sub–detectors of DELPHI are described, with most discussion being given to those components of particular importance to this analysis. Chapter 3 describes how a hadronic sample of events is selected and how these are then enriched in b quarks.

Chapter 4 describes the A^b_{FB} measurement and explains how the analysis was optimized to obtain the best possible sensitivity. Chapter 5 describes the selection of c events and the A^c_{FB} measurement.

Chapter 6 presents a comparison of the A^b_{FB} and A^c_{FB} results with the Standard Model and also describes the use of the results in putting limits on new physics within the Contact Interactions formalism.

Acknowledgements

I would like to thank Guy Wilkinson for his invaluable guidance and input which were essential to the production of this thesis. I feel lucky to have worked with him. I would also like to thank to Louis Lyons who guided me through important steps in the analysis and constructively criticized previous drafts of this thesis.

I would like to thank Paula Collins for her help in the first stages of the $b\bar{b}$ analysis and for her good advices and further help along the way. I would to thank Gerald Myatt for always showing interest in my work and for giving useful comments to a previous draft of this thesis.

Special thanks to Daniel Jeans for useful discussions and his help in various aspects of data analysis.

Thanks to John Holt for his help in my early stages as a graduate student, in particular in the computing aspects of the data analysis. Thanks to Wolfgang Liebig for being an excellent collaborator in the DELPHI heavy flavour group.

1. Heavy quark production in high energy e^+e^- collisions

1.1 Introduction

This chapter describes the Standard Model theory for fundamental particles and their various forms of interactions. In particular the production of heavy flavour of quarks in LEP is discussed. A discussion of new physics in the form of contact interactions is presented at the end. [1],[2] and [3] have been referred to extensively in the writing of this chapter.

1.2 The Standard Model

The Standard Model describes the fundamental particles and their interactions. The constituents of the theory are the fermions and bosons. Table 1.1 and 1.2 presents a summary of their properties. The theory describes the Electromagnetic, Weak and Strong interactions of particles.

1.2.1 The Standard Model Structure

The key postulate behind the Standard Model(SM) is its invariance under local gauge transformations. This means that conserved physical quantities, such as electric charge, should be conserved in local regions of space and not just globally. This principle is assumed to have a predictive power and is used as a guide in the construction of the theory to explain particle behaviour. The mathematical form used to express particle behaviour is the Lagrangian formalism. This allows the extraction of the particle's equation of motion and requires the fulfillment of the local

1	**2**	**3**	T_3	Y	Q
$\begin{pmatrix}\nu_e\\ e^-\end{pmatrix}_L$	$\begin{pmatrix}\nu_\mu\\ \mu^-\end{pmatrix}_L$	$\begin{pmatrix}\nu_\tau\\ \tau^-\end{pmatrix}_L$	$\begin{pmatrix}+\frac{1}{2}\\ -\frac{1}{2}\end{pmatrix}$	-1	$\begin{pmatrix}0\\ -1\end{pmatrix}$
e_R	μ_R	τ_R	0	-2	-1
$\begin{pmatrix}u\\ d'\end{pmatrix}_L$	$\begin{pmatrix}c\\ s'\end{pmatrix}_L$	$\begin{pmatrix}t\\ b'\end{pmatrix}_L$	$\begin{pmatrix}+\frac{1}{2}\\ -\frac{1}{2}\end{pmatrix}$	$+\frac{1}{3}$	$\begin{pmatrix}+\frac{2}{3}\\ -\frac{1}{3}\end{pmatrix}$
u_R	c_R	t_R	0	$+\frac{4}{3}$	$+\frac{2}{3}$
d'_R	s'_R	b'_R	0	$-\frac{2}{3}$	$-\frac{1}{3}$

Table 1.1: The members and electro–weak quantum numbers of the three generations of fermions: T_3 = third component of weak isospin; Y = weak hypercharge; Q = electric charge.

Bosons	**q**	**t**	T_3	Mass	Interaction
Vector Boson					
W^+	+1		+1	80.41 ± 0.06 GeV[5]	Weak
Z^0	0	+1	0	91.12 ± 0.002 GeV[5]	Weak
W^-	-1		-1	80.41 ± 0.06 GeV[5]	Weak
γ	0	0	0	0	QED
g	0	0	0	0	QCD
Scalar Boson					
H	0	0	0	115^{+116}_{-66}GeV	Yukawa

Table 1.2: The properties of the fundamental carriers of force. It should be noted the Higgs boson, H, has not been directly observed yet. The mass given for the Higgs boson is in the bounds infered indirectly from the fits to predominately Z^0 high precision measurements.

invariance principle. The equation of motion is extracted from a Lagrangian density $\mathcal{L}$ by applying:

$$\frac{\partial}{\partial X_\mu}\frac{\partial \mathcal{L}}{\partial(\partial\phi/\partial X_\mu)} = \frac{\partial \mathcal{L}}{\partial \phi} \tag{1.1}$$

which is the Euler-Lagrange equation, where $\mathcal{L} = (\phi, \frac{\partial}{\phi}\partial X_\mu, X_\mu)$ and the field ϕ is a function of X_μ, which are the space-time coordinates.

The Standard Model aims to describe the 3 type of interactions between particles: the electromagnetic, weak and strong. This is done by finding the correct Lagrangian and applying the Euler-Lagrange equation. The gauge group of the Standard Model is SU(3) $\otimes$ SU(2) $\otimes$ SU(1). These are respectively the groups corresponding to Strong, Weak and Electromagnetic interactions.

1.2.2 The QED Lagrangian

The QED Lagrangian is a subset of the Electroweak Lagrangian. However it is presented first to explain more clearly the principle of gauge invariance.
Local gauge invariance requires that the particle wave equation transform as:

$$\phi(x) \rightarrow \exp^{i\alpha(x)} \phi(x) \tag{1.2}$$

where $i\alpha(x)$ depends on space and time. This invariance is not satisfied for the Lagrangian $\mathcal{L}$:

$$\mathcal{L} = i\overline{\phi}\gamma^\mu\partial_\mu\phi - m\overline{\phi}\phi \tag{1.3}$$

where the derivative of ϕ transforms as:

$$\partial_\mu\phi \rightarrow \exp^{i\alpha(x)} \partial_\mu\phi + i\exp^{i\alpha(x)} \phi \cdot \partial_\mu\alpha \tag{1.4}$$

and the $\partial_\mu \alpha$ term breaks the invariance.

In order to keep the local gauge invariance a new derivative D_μ is introduced such that:

$$D_\mu \phi \to \exp^{i\alpha(x)} D_\mu \phi \tag{1.5}$$

and

$$D_\mu = \partial_\mu - ieA_\mu, \tag{1.6}$$

where e is the electric charge and A_μ transform as:

$$A_\mu \to A_\mu + \frac{1}{e}\partial_\mu \alpha. \tag{1.7}$$

The requirement of a local gauge invariance introduces a new vector field A_μ. If this vector field is regarded as the physical photon field, a term corresponding to its kinetic energy must be added in the Lagrangian. This gives the QED Lagrangian:

$$\mathcal{L} = i\overline{\phi}\gamma^\mu \partial_\mu \phi - m\overline{\phi}\phi + e\overline{\phi}\gamma^\mu A_\mu \phi - \frac{1}{4}F_{\mu\nu}F^{\mu\nu} \tag{1.8}$$

where $F_{\mu\nu} = \partial_\mu A_\nu - \partial_\nu A_\mu$.

1.2.3 The Electroweak Lagrangian

The Electroweak Lagrangian is $SU(2)_L \otimes U(1)_Y$ gauge invariant. The theory is chiral which means it has a different coupling to the left and the right handed components of the fermion's wave function. The left handed components transform as doublets and the right handed as singlets under SU(2) weak isospin transformation. The local gauge transformations are:

$$\psi_L \to \exp^{(i\frac{g}{2}\sigma_j \beta^j + i\frac{g'}{2}Y_L \alpha(x))} \psi_L \tag{1.9}$$

$$\psi_R \rightarrow \exp^{(i\frac{g'}{2}Y_R\alpha(x))}\,\psi_R \tag{1.10}$$

where σ_i (i=1,2,3) are the Pauli spin matrices,g and g' are the coupling constants, and Y_L and Y_R are the weak hypercharges of the left and right handed components. The requirement of gauge invariance under $SU(2)_L \otimes U(1)_Y$ generates 4 new fields in an identical way to the QED case. These fields are related to the gauge bosons fields. A B field arises from the U(1) transformation and three W^i (i=1,2,3) fields are generated by the SU(2) transformation. The gauge invariant Lagrangian can be written:

$$\mathcal{L} = i\overline{\phi}\gamma^{\mu}\partial_{\mu}\phi - \overline{\phi_L}\gamma^{\mu}(\frac{g}{2}\sigma W^{\mu} + \frac{g'}{2}Y_L I B^{\mu})\phi_L - \overline{\phi_R}\gamma^{\mu}\frac{g'}{2}Y_R B^{\mu}\phi_R - \frac{1}{4}W^{\mu\nu}W_{\mu\nu} - \frac{1}{4}B^{\mu\nu}B_{\mu\nu} \tag{1.11}$$

where $W^{\mu\nu} = \partial^{\mu}W_i^{\nu} - \partial^{\nu}W_i^{\mu} - gW^{\mu} \times W^{\nu}$, and I is a unit matrix.
The charged W boson fields are given by:

$$W^{\pm} = \frac{1}{\sqrt(2)}(W_{\mu}^1 \pm W_{\mu}^2). \tag{1.12}$$

Since the Z couples to both left and right-handed fermions it is clear that the fields corresponding to the physical photon and Z are orthogonal linear combinations of the W and B fields:

$$A_{\mu} = \sin\theta_W W_{\mu}^3 + \cos\theta_W B_{\mu}, \tag{1.13}$$

$$Z_{\mu} = \cos\theta_W W_{\mu}^3 - \sin\theta_W B_{\mu}, \tag{1.14}$$

where θ_W is known as the Electroweak mixing angle. The relationship between the weak coupling of the W field g_W, the $g\prime$ coupling of the B field and the photon coupling g_e can be derived from the above:

$$g_W \sin\theta_W = g' \cos\theta_W = g_e. \tag{1.15}$$

The above lagrangian does not include mass terms to the gauge bosons the fermions. The mechanism that gives mass is called Spontaneous Symmetry Breaking, or the Higgs mechanism and proceeds by introducing an additional term to the lagrangian.

1.2.4 Renormalisability and Feynman rules

The calculations of quantities in the Standard Model are performed by making a perturbative expansion in powers of the coupling constants. Due to Feynman loop diagrams there could arise infinities in the expansion series. Renormalisability insures that any infinities arising are exactly cancelled by others. It was proved by t' Hooft[4] that the Standard Model is a Renormalisable theory.

1.3 The process $e^+e^- \to q\overline{q}(\gamma)$

The production of $q\overline{q}(\gamma)$ quark anti-quark pairs with a possible accompanying photon in the final state, at LEP proceeds at Born level through the Feynman diagrams shown in figures 1.1 and 1.2. The production occurs through a photon or a Z exchange and involves interference between the two. The total cross section peaks at the Z pole and drops rapidly with energy as can be seen in figure 1.4.

1.3.1 The Forward-Backward asymmetry

The differential cross section at Born level is built using the Feynman rules[5]:

$$M_\gamma = ie^2(\bar{e}\gamma^\mu e)\frac{1}{k^2}(\bar{q}\gamma_\mu q) \tag{1.16}$$

$$M_{Z^0} = \frac{ig^2}{4cos^2\theta_W}(\bar{e}\gamma^\mu(g_V^e - g_A^e\gamma^5)e)\frac{1}{k^2 - M_Z^2 + iM_Z\Gamma}(\bar{q}\gamma_\mu(g_V^q - g_A^q\gamma^5)q) \tag{1.17}$$

where M_γ and M_{Z^0} corresponds to the matrix elements of the γ and Z^0 exchange. k is the four momentum, M_Z and Γ are the Z^0 mass and width, g_V^e, g_A^e, g_V^q, g_A^q are the vector and axial coupling of the electron and the quarks, and $\bar{e}, e, \bar{q}, q$ are the Dirac spinors of the incoming e^+e^- and the outgoing q^+q^-. The differential cross section is proportional to the squared matrix element:

$$\frac{\mathrm{d}\sigma}{\mathrm{d}\cos\theta} \propto |M_\gamma + M_{Z^0}|^2 = e^4[F(s)(1+cos^2\theta) + G(s)cos\theta] \qquad (1.18)$$

where

$$\begin{aligned} F(s) = 1 & \qquad \gamma \text{ exchange} \\ + \ 2g_V^e g_V^q Re(\chi) & \qquad \gamma - Z^0 \text{ interference} \\ + \ ((g_V^e)^2 + (g_A^e)^2)((g_V^q)^2 + (g_A^q)^2)|\chi|^2 & \qquad Z^0 \text{ exchange} \end{aligned} \qquad (1.19)$$

$$\begin{aligned} G(s) = \ & 4g_A^e g_A^q Re(\chi) & \qquad \gamma - Z^0 \text{ interference} \\ + \ & 8g_V^e g_A^e g_V^q g_A^q |\chi|^2 & \qquad Z^0 \text{ exchange} \end{aligned} \qquad (1.20)$$

and

$$\chi = \frac{1}{4\cos^2\theta_W \sin^2\theta_W (s - M_Z^2 + iM_Z\Gamma_Z)} \qquad (1.21)$$

The $q\bar{q}$ production angle, Θ_q, is defined in figure 1.3 and is the angle between the outgoing quark and the incoming electron beam direction.

The forward and backward asymmetry, A_{FB}^q, is defined as:

$$A_{FB}^q = \frac{\sigma(F) - \sigma(B)}{\sigma(F) + \sigma(B)} \qquad (1.22)$$

where

$$\sigma(F) = \int_0^1 \frac{\mathrm{d}\sigma}{\mathrm{d}\cos\theta}\mathrm{d}\cos\theta \tag{1.23}$$

$$\sigma(B) = \int_{-1}^0 \frac{\mathrm{d}\sigma}{\mathrm{d}\cos\theta}\mathrm{d}\cos\theta \tag{1.24}$$

By integrating expression 1.23 and 1.24 we can see the forward and backward asymmetry, A^q_{FB}, is given by:

$$A^q_{FB} = \frac{3 \cdot G(s)}{8 \cdot F(s)}. \tag{1.25}$$

From equations 1.19 - 1.25 one can see that the forward-backward asymmetry arises from the Z^0 vector and axial coupling and the $Z^0 - \gamma$ interference. The difference between the expected value of A^q_{FB} for b and c quarks come from their different vector and axial coupling values. However, these differences do not have a large effect on the the general A^q_{FB} values and they are similar for both quarks. This is shown in figure 1.5 where the A^q_{FB} value is shown as a function of centre-of-mass energy for b and c quarks. This theoretical prediction is made using the ZFITTER[26] program and include high order corrections(discussed in the next section). One can see that the A^q_{FB} value does not change much at high energies for both quarks. At energies close to the Z^0 peak, however, there is a rapid variation in the value of the asymmetry due to the dominances of the Z^0 vector and axial coupling interference.

1.3.2 Radiative corrections

QED corrections

The QED corrections to the Born level $e^+e^- \to q\bar{q}$ process can be divided into initial and final state radiation, termed ISR and FSR respectively. Of these ISR is the dominant process.

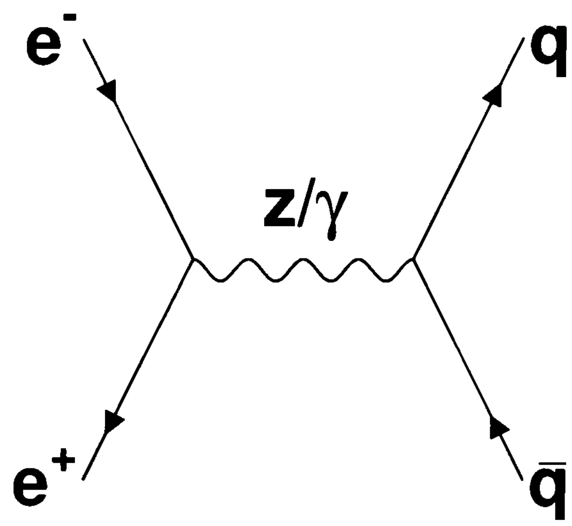

Figure 1.1: The Born level Feynman diagrams for the production of $q\bar{q}$

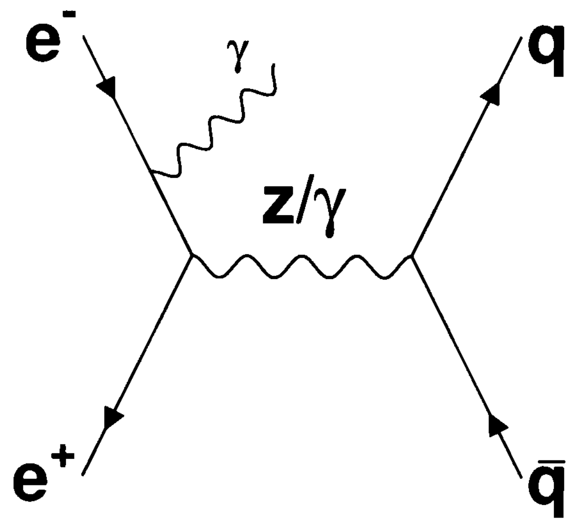

Figure 1.2: The Born level Feynman diagrams for the production of $q\bar{q}(\gamma)$

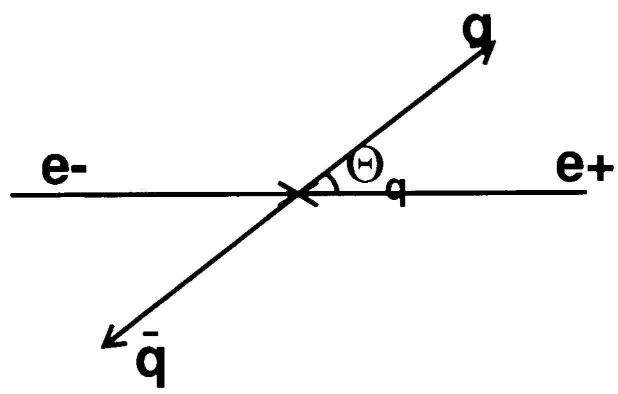

Figure 1.3: The $q\bar{q}$ production angle, Θ_q.

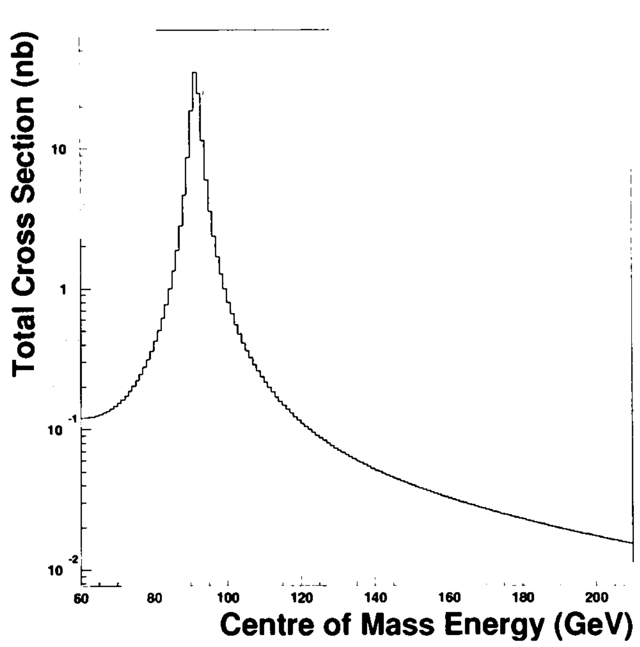

Figure 1.4: The cross section of the process $e^+e^- \to q\bar{q}$ as a function of centre-of-mass energy. This theoretical prediction is obtained using the ZFITTER[26] program for events with no initial state radiation.

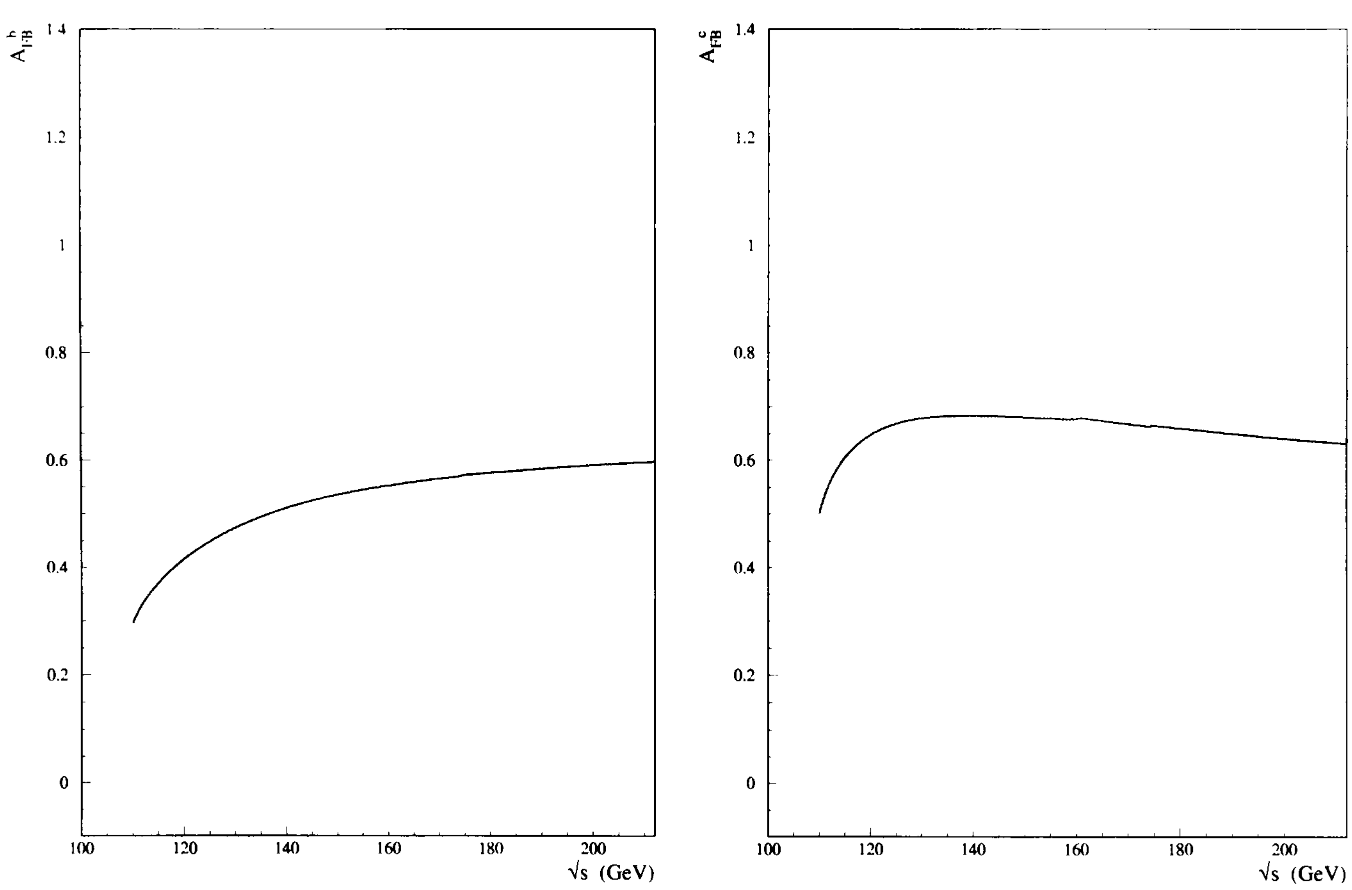

Figure 1.5: Left: The SM A_{FB} value as a function of centre-of-mass energy for $b\bar{b}$ events. Right: The SM A_{FB} value as a function of centre-of-mass energy for $c\bar{c}$ events. The theoretical prediction is obtained using the ZFITTER[26] program for events with no initial state radiation.

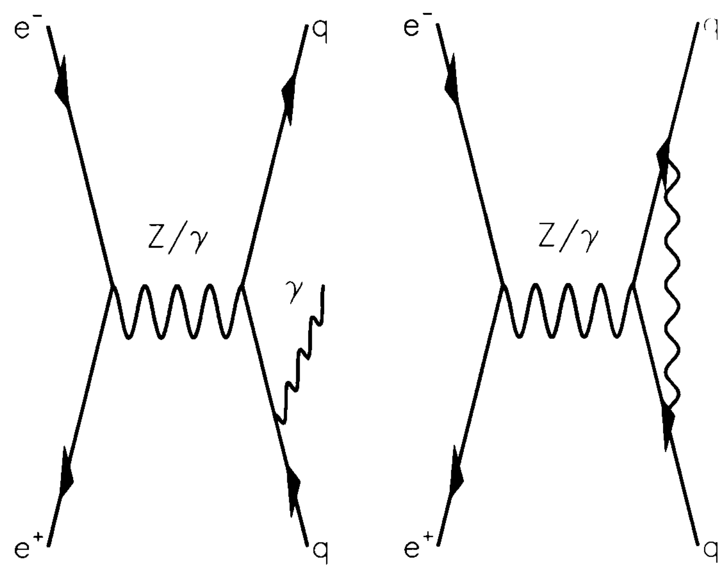

Figure 1.6: Final state radiation.

- **Initial state radiation**: Initial state radiation occurs when one of the electron or positron emits a photon effectively reducing the amount of energy available in the centre-of-mass of the incoming e^+e^- pair. This is shown in figure 1.2. For LEP2 energies the emitted ISR energy is often significant, leading to the so called radiative return process, whereby a large proportion of events radiate enough photonic energy to reduce the collision energy to that of the Z^0. This thesis is concerned with those events with little or no ISR.

- **Final state radiation**: Final state radiation occurs when a photon is emitted from one of the quarks. Examples are shown in figure 1.6 . This correction is less important than the ISR since it does not change the centre-of-mass energy.

Weak corrections

The Born level predictions also receive corrections through the weak diagrams. Weak corrections are subdivided into 3 classes: vertex , propagator and box. Figure 1.7

shows examples of these 3 classes:

- Vertex corrections: depend on the flavour of the initial and final state fermion.
- Propagator corrections: do not depend on the flavour of the initial and final state fermion.
- Box corrections correspond to the exchange of more than one Z^0 or $W^\pm$.

These corrections amount to a few percent of the total cross section at LEP2 energies[36].

1.4 Contact interactions

Possible physics beyond the SM include one or more additional heavy gauge bosons or structure in the 'fundamental' particles. Either of these could manifest themselves as deviations from the SM predictions for fermion pair production at high energy. Deviation from the standard model predictions to the process $e^+e^- \rightarrow q\bar{q}$ can be described model-independently in the form of effective four-fermion contact interactions. Contact interactions are parametrized by an effective Lagrangian[23] added to the SM Lagrangian of the form:

$$\mathcal{L}_{eff} = \frac{g^2}{\Lambda^2} \sum_{i,j=L,R} \eta_{ij}(\overline{e_i}\gamma_\mu e_i)(\overline{f_j}\gamma^\mu f_j), f \neq e \tag{1.26}$$

where e_i and f_j denote left and right handed spinors, Λ is the scale of the contact interaction and the coupling g is taken to be 1 by convention. Different models[24] which correspond to different helicity coupling $\eta_{ij} = \pm 1$ or 0 between initial and final state fermions can be explored. For example a coupling of two right-handed currents is given by $\eta_{RR} = \pm 1, \eta_{LR} = \eta_{RL} = \eta_{LL} = 0$. In this thesis we consider 8 of these models. These models have been chosen as they can produce the largest effects in the $e^+e^- \rightarrow b^+b^-$ production. The values of η_{ij} which define these models

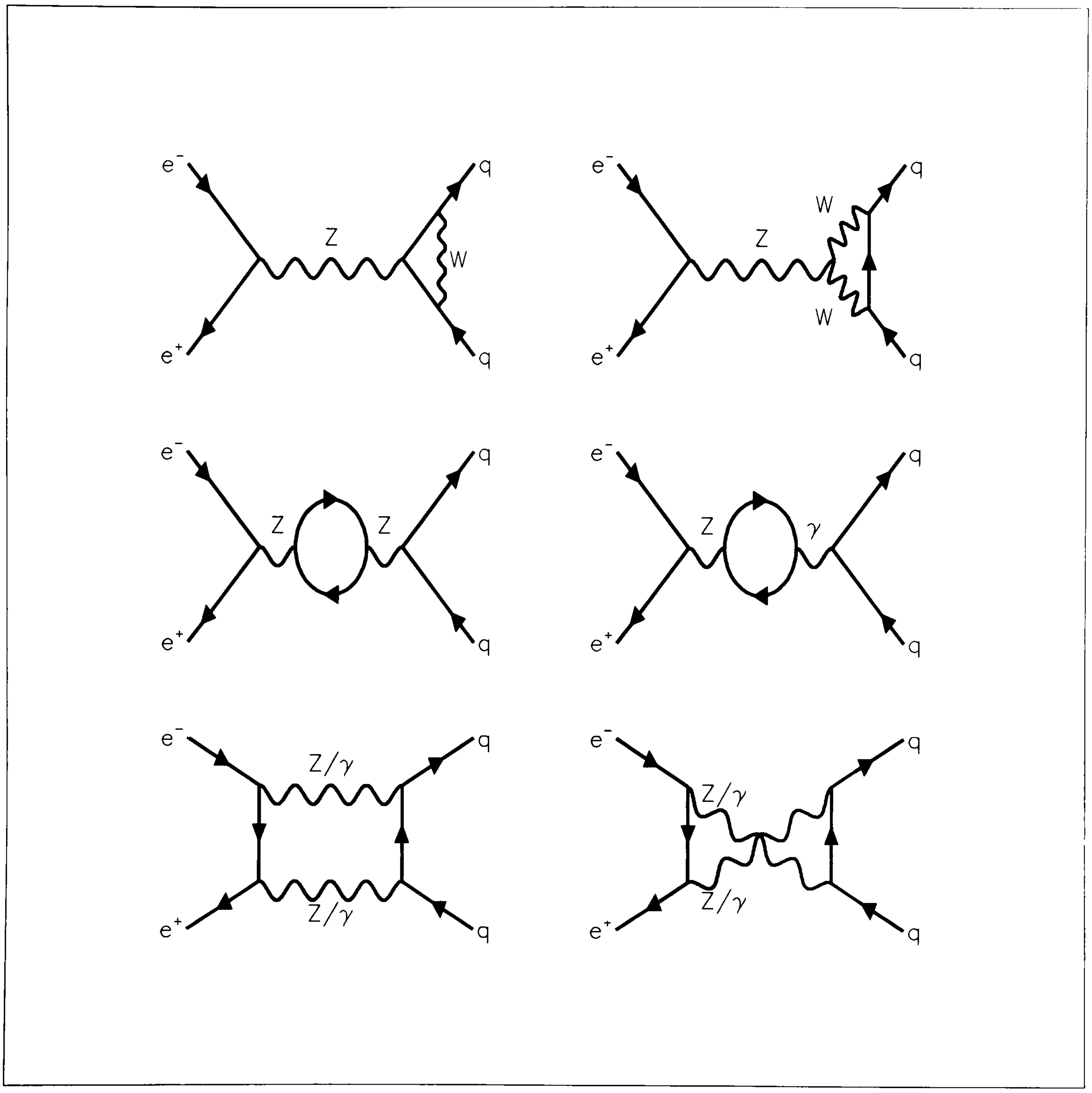

Figure 1.7: Weak corrections to $e^+e^- \to q\bar{q}$: top row - vertex; middle row - propagator; bottom row: box.

Model	η_{LL}	η_{RR}	η_{LR}	η_{RL}
$LL^{\pm}$	$1^{\pm}$	0	0	0
$RR^{\pm}$	0	$1^{\pm}$	0	0
$VV^{\pm}$	$1^{\pm}$	$1^{\pm}$	$1^{\pm}$	$1^{\pm}$
$AA^{\pm}$	$1^{\pm}$	$1^{\pm}$	$1^{\pm}$	$1^{\pm}$
$LR^{\pm}$	0	0	$1^{\pm}$	0
$RL^{\pm}$	0	0	0	$1^{\pm}$
$VO^{\pm}$	$1^{\pm}$	$1^{\pm}$	0	0
$AO^{\pm}$	0	0	$1^{\pm}$	$1^{\pm}$

Table 1.3: Values of η_{ij} for different contact interactions models.

are shown in table 1.3. Each model can have constructive (+) or destructive (-) interference with the SM Lagrangian.

The inclusion of contact interactions modifies both the total cross section and the angular distribution of quark pair production. In general the differential cross section can be written in terms of a parameter $\epsilon = \frac{g^2}{4\pi\Lambda^2}$ as:

$$\frac{d\sigma}{d\cos\theta} = \sigma_{SM}(s,t) + C_2^0(s,t)\epsilon + C_4^0(s,t)\epsilon^2 \tag{1.27}$$

where $t = -s(1-\cos\theta)/2$. The C_2^0 term describes the interference between the SM and the contact interaction, the C_4^0 term is a pure contact interaction contribution. The interference term depends linearly on η_{ij} parameters and thus can be constructive or destructive depending on their sign.

1.5 Experimental Considerations

This section presents the theoretical background behind several miscellaneous issues relevant for the measurement. These include 4-fermion backgrounds, the CKM matrix, B mixing and b hadronisation.

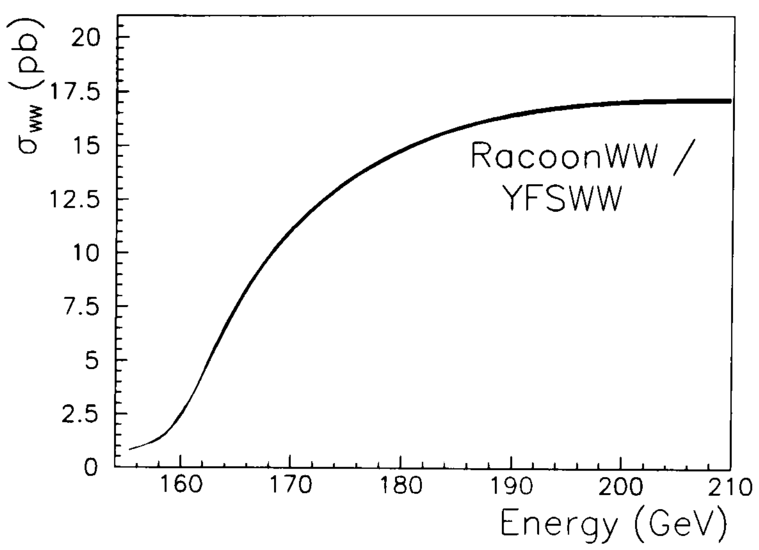

Figure 1.8: The W^+W^- production cross section. The SM predictions are obtained by using results of the Racoon[32] and YESWW[33] groups. This figure was obtained from [34].

1.5.1 4-fermion backgrounds

4-fermion backgrounds for $q\bar{q}$ production at high energy include W^+W^- and Z^0Z^0 events. The main backgrounds are W^+W^- events in which one or both W's decay hadronically. The W^+W^- cross section as a function of energy is shown in figure 1.8[34]. One can see the cross section does not change much at high energies and is significantly lower than the $q\bar{q}$ cross section shown in figure 1.4.

1.5.2 Quark mixing

It is an experimental fact that the quark mass eigenstates are rotated with respect to the flavour eigenstates in weak charged interactions. This rotation can be described by the CKM matrix[3,6]. At present, this is determined using experimental measurements and its elements can not be directly calculated by any current theory, though constraints can be inferred from the Standard Model. The existence and form of the matrix can be theoretically verified in $U(1)_Y \times SU(2)_L$ through the diagonalisation of the quark mass matrices, which imposes that the CKM matrix is unitary[6,7],

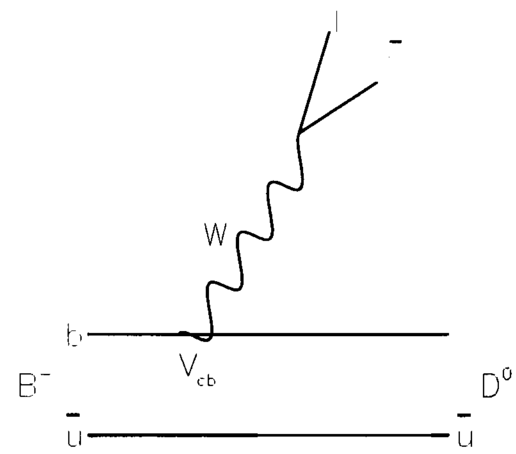

Figure 1.9: B^- decay into a charged lepton and a neutral D meson.

$$\begin{pmatrix} V_{ud} & V_{us} & V_{ub} \\ V_{cd} & V_{cs} & V_{cb} \\ V_{td} & V_{ts} & V_{tb} \end{pmatrix} = \begin{pmatrix} (0.974-0.976) & (0.217-0.224) & (0.002-0.004) \\ (0.217-0.224) & (0.974-0.975) & (0.036-0.042) \\ (0.004-0.013) & (0.035-0.042) & 0.999 \end{pmatrix} \quad (1.28)$$

The values of the CKM matrix elements, V, govern the decay of the W into quarks as they enter in the relevant matrix element.

The CKM matrix element which is of particular importance in this thesis is V_{cb}. For example, in the the decay of a B^- hadron to a D and a charged lepton shown in figure 1.9. The decay probability depends on V_{cb}^2. Its low value is responsible for the B hadron relatively long life time, a feature which enables us to experimentally separate b events from the rest of the background.

1.5.3 b mixing

An important process that occurs in the neutral B hadron system is the b mixing or oscillation. This process proceeds through the Feynman diagrams shown in figure 1.10 where through an intermediate box diagram a B^0 oscillates into a $\overline{B^0}$. The

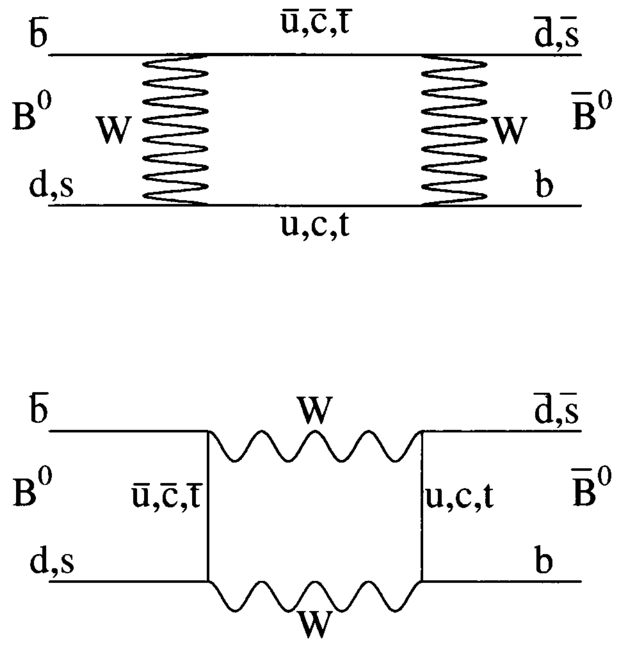

Figure 1.10: Box diagrams contributing to the neutral $B^0 - \overline{B^0}$ oscillation process.

probability of mixing is determined by the CKM elements in the box diagram and the masses of the virtual particles in the box. As diagrams involving the top quark are dominant the relevant CKM elements are V_{td} and V_{ts}. As these elements differ in magnitude, the probability of oscillation is different for a B_d^0 and B_s^0. It is usual however to define χ, the probability of a B hadron of any type to oscillate. The experimental measured value of χ is 0.118 ± 0.004[28]. The mixing process has an effect on the effort to assign the charge of the initial quarks in the event which is needed for the asymmetry measurement. This effect is discussed in chapter 4.

1.5.4 Heavy Quark Hadronisation

The process in which a quark evolves into a jet of hadrons is called hadronisation. The most widely model used to describe heavy quark hadronisation is the Peterson fragmentation model[8]. The fragmentation function for the process can be written as:

$$F(z) = \frac{N_Q}{z(1 - \frac{1}{z} - \frac{\epsilon}{1-z})^2}$$

where N_Q is a normalization constant, ϵ is the Peterson parameter and z is a measure of how much of the original energy and momentum parallel to the initial quark is carried by the b(c) hadron:

$$z = \frac{E_{b,c} + P_{dot}}{E_{b,c}^{had} + P_{b,c}}$$

where $E_{b,c}$ is the quark energy, $E_{b,c}^{had}$ is the b(c) hadron energy, $P_{b,c}$ is the quark momentum and P_{dot} is the dot product between the b(c) hadron momentum and the b(c) quark momentum.

The distribution of F(z) for the the b and c hadrons(using the values of the Peterson parameters as used in the MC in this thesis) is shown in figure 1.11.
It can be seen from figure 1.11 that both hadrons carry a large fraction of the initial quark energy. This sets the theoretical basis for the Jet Charge technique(discussed in chapter 4) for the separation of b(c) and $\bar{b}(\bar{c})$ jets, in which the inital charge of the primary quarks is inferred from the momentum weighted charges of the particles in the jet.

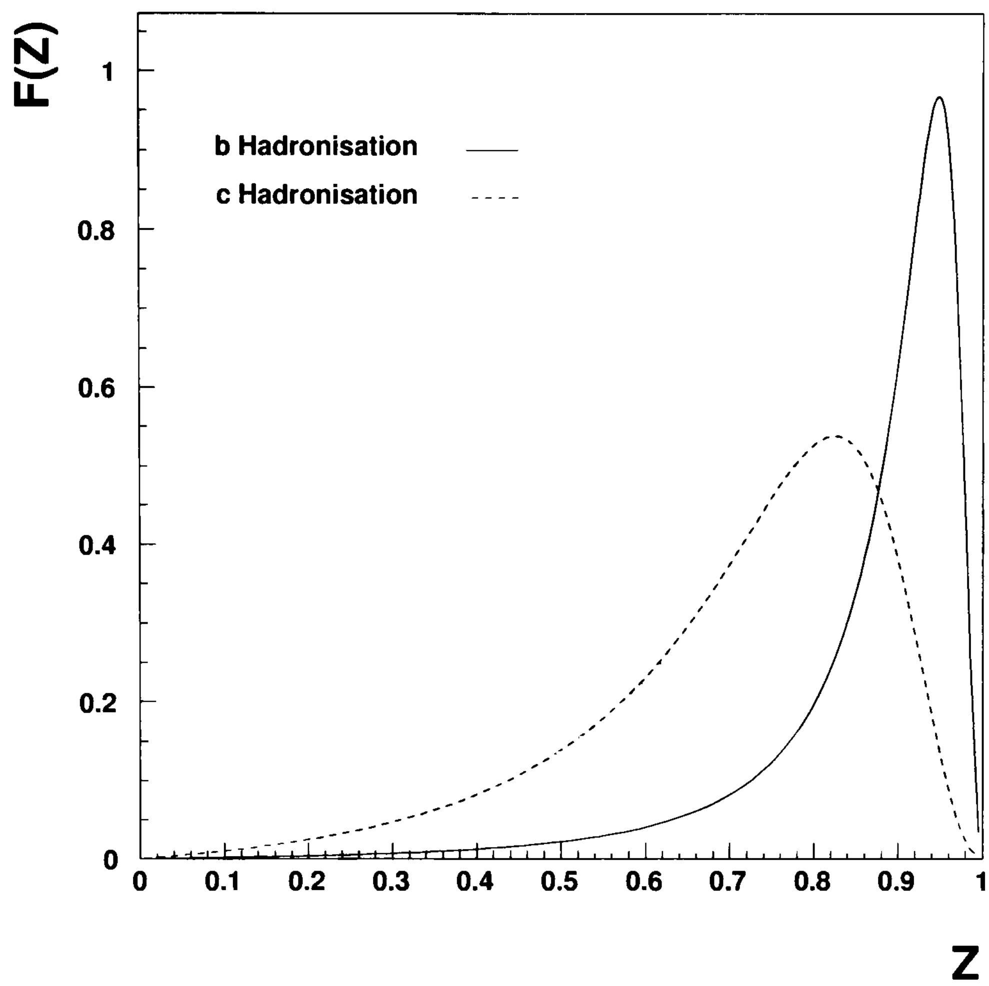

Figure 1.11: The Peterson fragmentation function for b and c hadrons. The graph shows that on average the b hadrons will have higher momentum than the c hadrons. These graphs are normalized to an arbitrary scale. The Peterson parameters values used for b and c are 0.00284 and 0.0372 respectively.

2. DELPHI Detector

2.1 Introduction

This chapter describes the LEP accelerator and the DELPHI detector, paying attention to those components of particular relevance to the subjects of this thesis.

2.2 The LEP accelerator

The LEP(Large Electron Positron) collider situated at CERN near Geneva, Switzerland consists of a tunnel 100m below the ground with a circumference of 26.7km. The ring is made of 8 straight sections and 8 arcs with 4 experiments(DELPHI, ALEPH, OPAL, L3) placed at the centre of each alternate straight section. The detectors are situated in the straight sections in order not to be exposed to the synchrotron radiation coming from the bending beams. The beams are accelerated using a set of super-conducting RF cavities placed along the straight sections. The beam energy is increased by the RF cavities from their initial value on entering from the injection chain of 20 GeV to that required for the desired collision energy. Then the RF cavities accelerate the beams only to compensate for the energy loss in the arcs: synchrotron radiation which is proportional to the E^4 and inversely proportional to the radius. Each beam consists of 4 bunches. In the curved sections the beams are guided using a set of dipole magnets. Containing the beam in a small volume is important for achieving high luminosity. The whole beam line is held in near vacuum in order to minimize interactions with gas particles. The time between the crossing of the beams is 22 μs.

LEP had two different operational periods: LEP1 where the beam energy corresponded to a centre-of-mass energy close or equal to the Z mass(91 GeV); LEP2

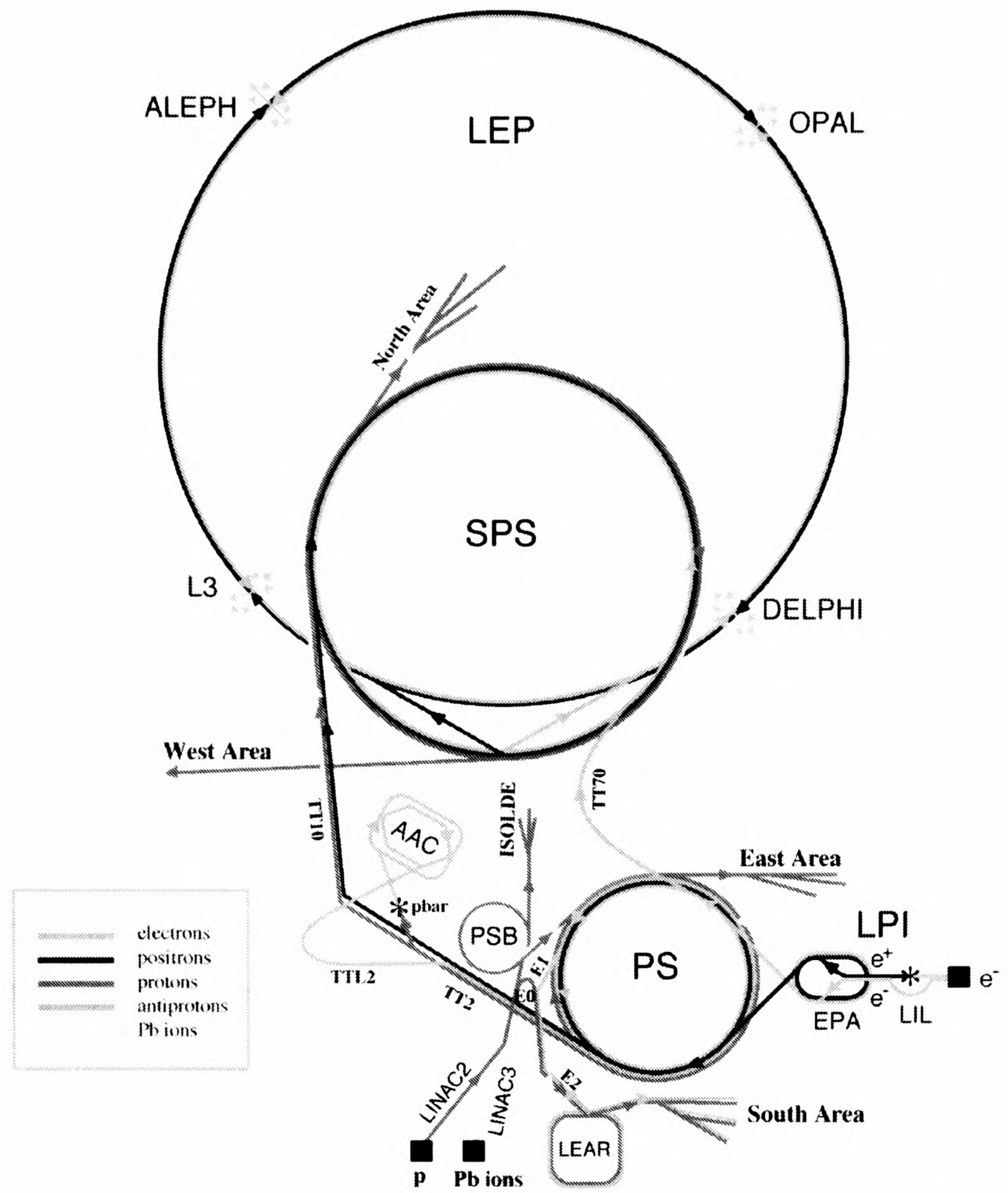

Figure 2.1: The CERN Accelerators. LEP: Large Electron Positron collider, SPS: Super Proton Synchrotron,PS : Proton Synchrotron, LPI: LEP Pre-Injector, EPA: Electron Positron Accumulator, LIL: LEP Injector Linac.

where the beam energy was gradually increased each year to correspond to centre-of-mass energies from 133 GeV to 208 GeV. The data analyzed in this thesis came from the LEP2 period.

2.2.1 Injector Chain

The acceleration setup of the e^+ and e^- beams before entering the LEP ring is shown in figure 2.1.

Year	1996	1997	1998	1999	2000
Energy (GeV)	161, 172	183	189	192, 196, 200, 202	205, 207
$\int \mathcal{L}dt$ (pb^{-1})	10, 10	52	154	26 , 77 , 84 , 41	82 , 136

Table 2.1: Integrated luminosities delivered in LEP2.

The production and acceleration of the beams follows these stages:

- A high intensity electron beam of 200 MeV bombards a tungsten target in the first LINAC(labeled as LIL in figure 2.1). This bombardment produces positrons through the creation of e^+e^- pairs. Electrons are produced using a separate, lower intensity gun.
- A second LINAC accelerates both these positrons and electrons, produced using a second lower intensity electron gun, up to 600 MeV.
- The beams are next stored in the EPA which injects them to the Proton Synchrotron (PS) where their energy is raised further to 3.5 GeV.
- The beams are then injected to the Super Proton Synchrotron (SPS) where they are accelerated to 20 GeV, and then injected into the LEP ring.

2.2.2 LEP2 Performance

The nominal centre-of-mass energies and the approximate integrated luminosities delivered by LEP2 to each experiment during the years are shown in table 2.1. The centre-of-mass energy was increased each year by adding more RF cavities. This strategy was followed in order to search for the Higgs boson and to study e^+e^- interactions at higher energies. Z^0 calibration runs were made each year for detector alignment purposes.

2.3 DELPHI Overview

The DELPHI(DEtector with Lepton, Photon and Hadron Identification) detector was one of the 4 detectors placed around the LEP ring. A schematic of the detector is shown in figure 2.2. Full details can be found in[9],[10]. The detector is designed to have good tracking from very close to the e^+e^- interaction point and calorimetry performance over almost the full solid angle. DELPHI also has hadron identification capabilities through the Ring Imaging CHerenkov(RICH) detectors based on Cherenkov light and the dE/dX information coming from the TPC(time projection chamber). Figure 2.3 shows the DELPHI coordinate system. The set of tracking detectors are placed inside a large super-conducting solenoid magnet which produces a 1.2T field along the z axis. Tracks bend in the magnetic field according to their charge which allows the determination of their momentum through $1/r \propto 1/p$ where r is the radius of curvature and p is the momentum.

2.4 Silicon Tracker

Separating heavy from light flavours of quarks can be performed by exploiting their relatively long life time. For example, a B hadron of proper lifetime of 1.6 ps and of momentum 50 GeV in the lab frame will travel 0.48 cm before decaying in a secondary vertex, which will be typically followed by an additional vertex close by from the accompanying D decay. In order to closely follow this decay topology one needs to have accurate tracking very close to the interaction point. This sets the motivation behind DELPHI's silicon tracker(ST) and makes the vertex detector(VD)[11] the most important experimental component for this thesis. Since the startup of LEP the VD was continuously upgraded. In 1991 a reduction in the beampipe radius made it possible to move from a two layer to a three layer geometry. In 1994 the capability was extended to 3-D measurements, providing a z coordinate along with the previously available $R\phi$ coordinate. At the same time the innermost layer was extended in length in anticipation of the final upgrade in 1996, which extended the barrel region to provide b tagging down to a polar angle of 25° and added forward end-caps to improve the tracking down to a polar angle of 11°. Figure 2.4 illustrates

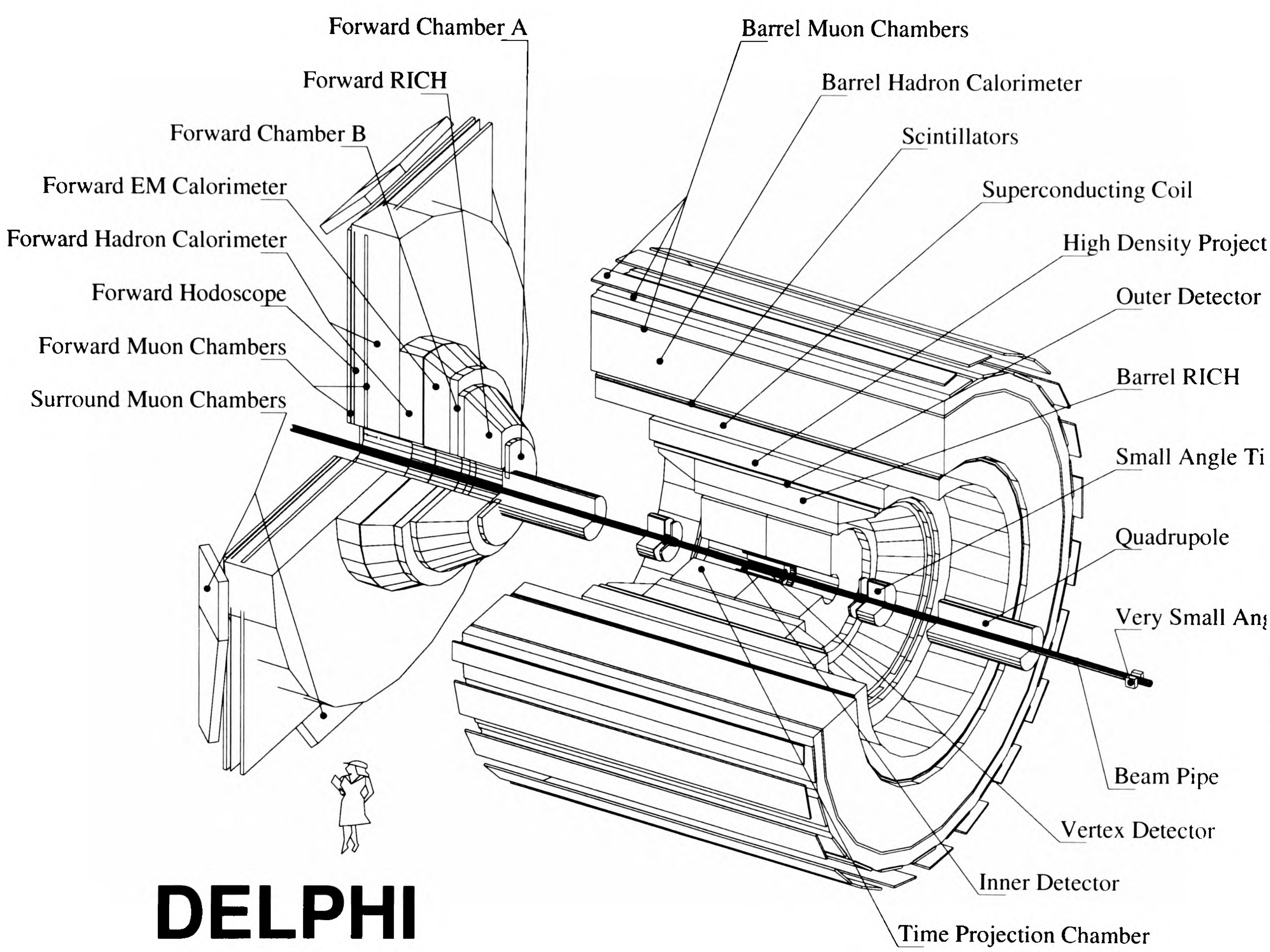

Figure 2.2: The DELPHI detector. An exploded cut-away view of the barrel and one end-cap is shown.

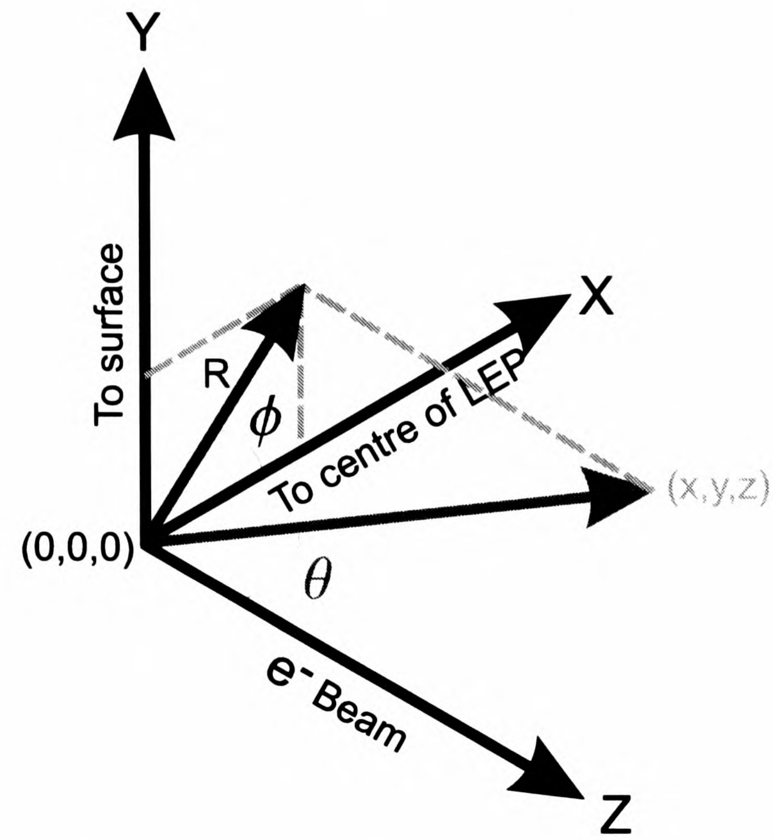

Figure 2.3: The DELPHI coordinate system.

this final version of the so called "Silicon Tracker", which is the one that was used for all the data analysis described in this thesis.

2.4.1 Silicon Tracker - Barrel Part

A cross section of the Silicon Tracker showing the barrel layers, which are most important for the b tagging, is shown in figure 2.6. The detector is designed in such a manner that the material budget is kept as low as possible, to reduce the multiple scattering error contribution for low momentum tracks. The first measured point is at the smallest possible radius, and the outermost measured point provides the greatest possible lever arm in the space available. The particles must first traverse the 1.45 mm thick beryllium beampipe, which gives a material contribution of 0.4% for perpendicular tracks. The barrel part extends down to a polar angle of 25° after which multiple scattering in the beam pipe degrades the b tagging performance. The first measured point on the track is in the so called closer layer, which lies at an average radius of 6.6 cm. This layer is double sided, giving an $r\phi$ and a z measurement so that the only material in the sensitive region comes from the 300μm thickness of the silicon itself. The double sided detector concept is illustrated in figure 2.5. The polar angle coverage is achieved with a ladder comprison of 4 silicon sensors long. The next two layers, called inner and outer layers, consist of ladders constructed of 8 standard length silicon sensors. The inner layer provides 2-D measurements in the central region and 3-d measurements in the outer region. The outer layer, where multiple scattering is less critical for the b tagging, gives a 3-D measurement by using single sided $r\phi$ and z measuring sensors mounted back to back, in the whole length of the ladder. Throughout the barrel part, the $r\phi$ measuring diodes have a pitch of 25μm and a readout pitch of 50μm while the readout pitch of the z measuring diodes is varied to match the polar angles of the tracks.

2.4.2 Silicon Tracker - Forward Part

The very forward part of the Silicon Tracker complements the tracking in the region down to 10.5 degrees and was implemented to improve the hermeticity of the DELPHI detector for LEP2 physics. The tracker consists of two layers of pixel detectors equipped with 330μm square pixels and and two layers of ministrip detectors equipped with 100μm pitch diodes with a readout pitch of 200μm. The modules overlap to give complete coverage in the forward region. The ministrip detectors provide track points and the pixel detectors help in the pattern recognition procedure.

2.4.3 VD alignment

The alignment procedure is a vital first step for the tagging of heavy flavour decays. The starting point for the alignment is the information from the optical and mechanical survey before installation. The alignment was defined from the information from tracks from Z decays, using a stand-alone procedure where the momentum of the tracks was the only information taken from the rest of the DELPHI detector.

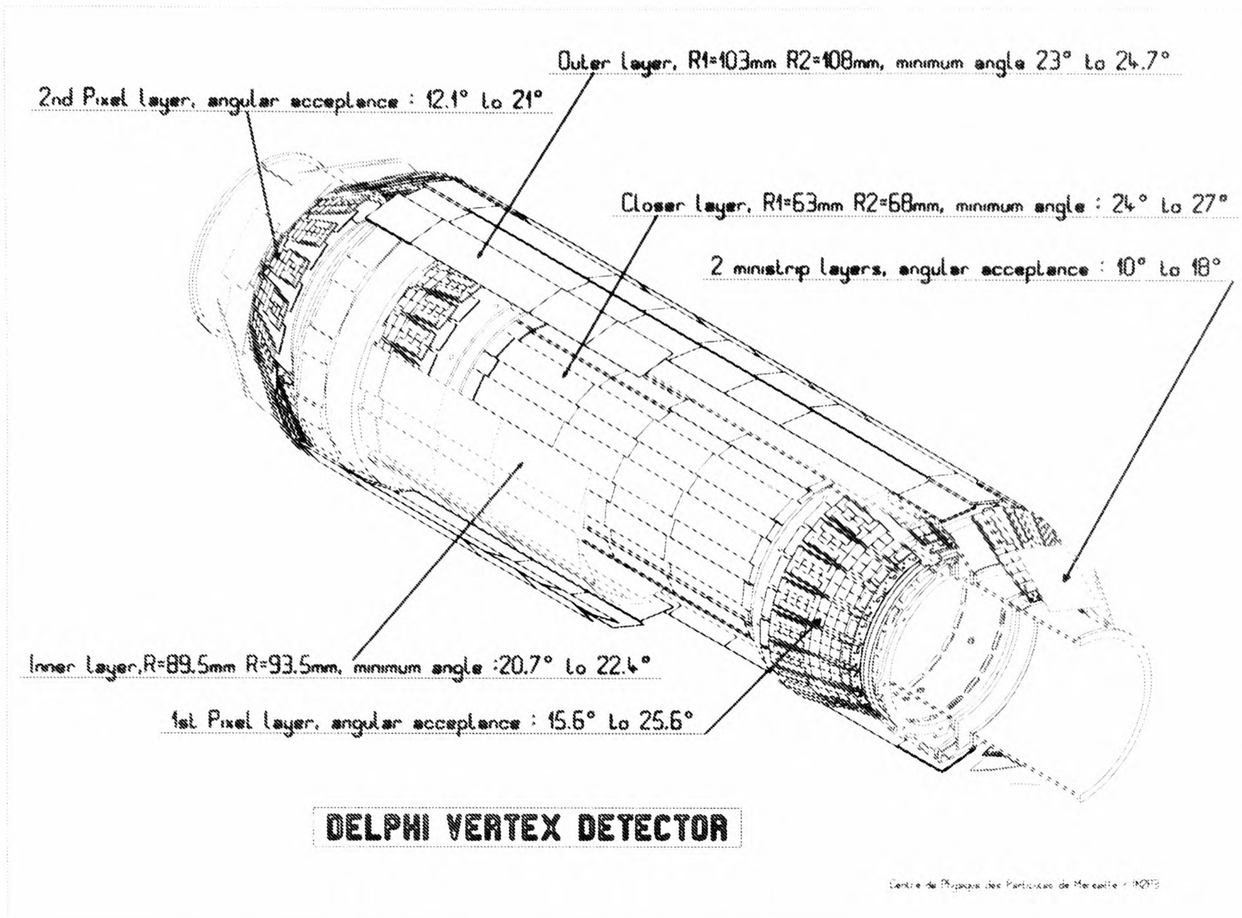

Figure 2.4: The DELPHI Silicon Tracker.

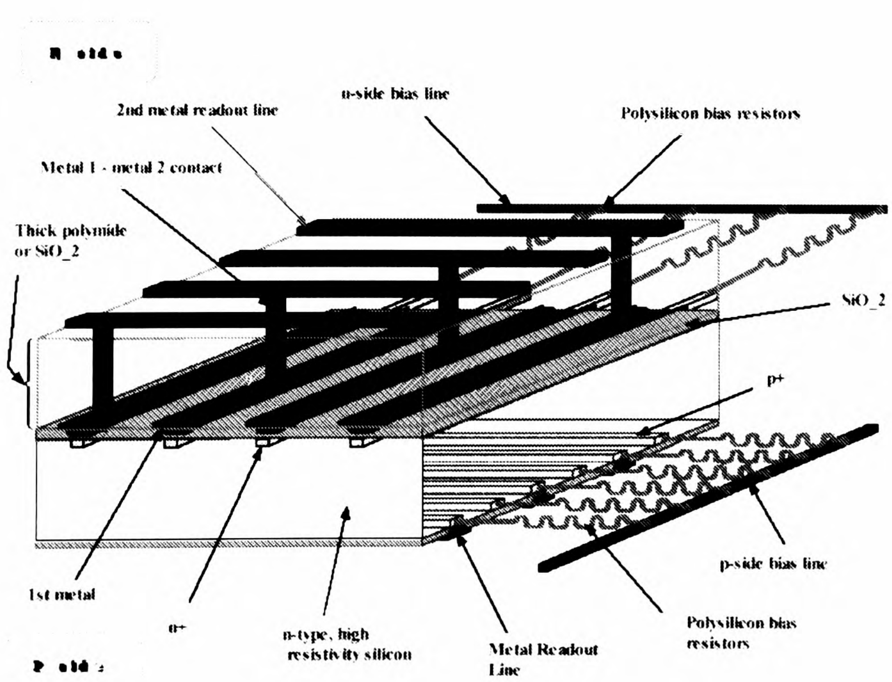

Figure 2.5: Individual double-sided silicon detector.

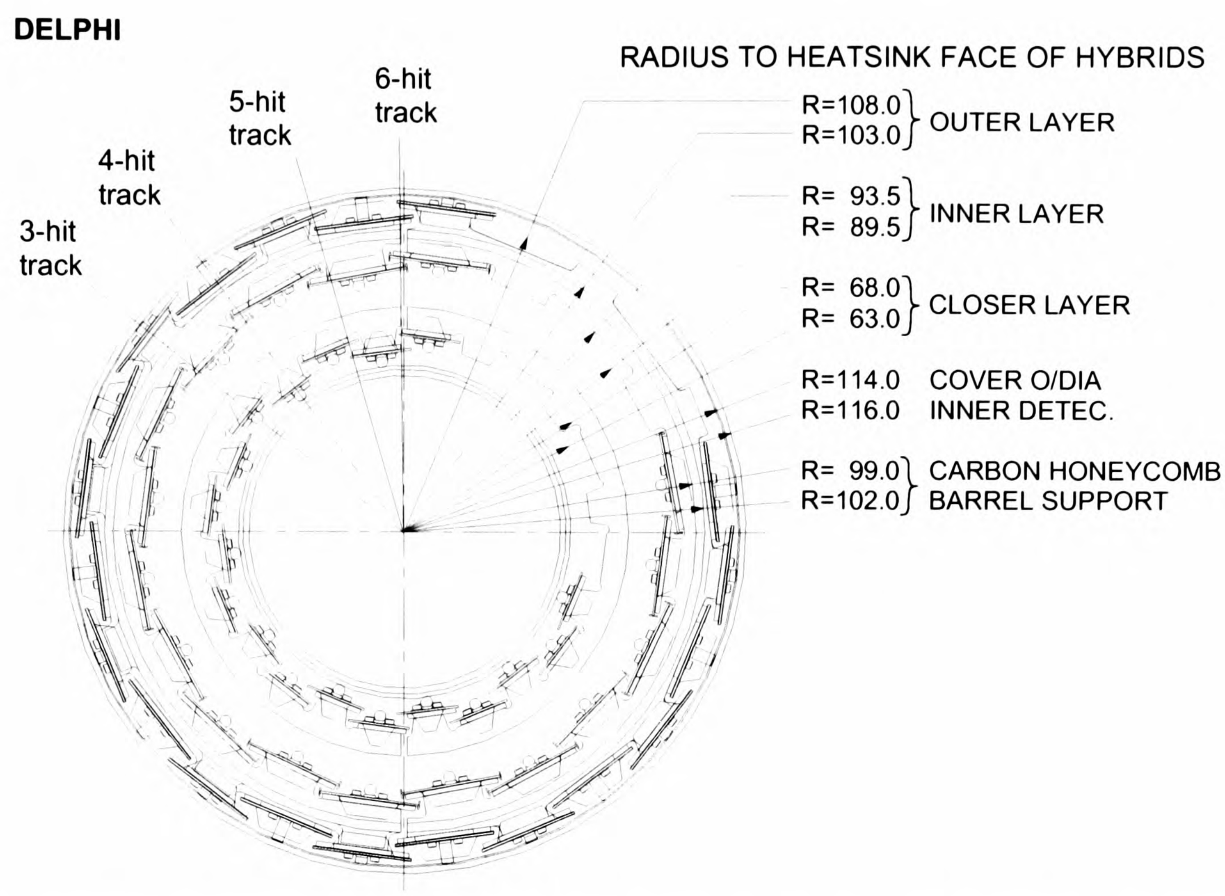

Figure 2.6: Schematic cross section of the barrel part of the Silicon Tracker.

The precision of the vertex detector hits has allowed a number of important effects to be identified, including some common to all LEP vertex detectors and certain previously un-measured properties of silicon detectors. They include:

- Coherent deformation, such as a torsion or shear of the entire structure.
- Bowing of the silicon modules due to the different response of the silicon and the module support to changes in temperature.
- Barycentric shift effects, whereby the centres of gravity of the charge clouds of electrons and holes in the silicon do not correspond to the mid-plane of the detector, nor to each other.
- Acollinearity of the LEP electrons and positrons beams leading to lepton pairs from Z decays which can not be assumed to be back to back in the alignment procedure.

More details can be found in [5].The main effects are corrected for in the alignment, allowing for the best possible Impact Parameter(IP) precision.

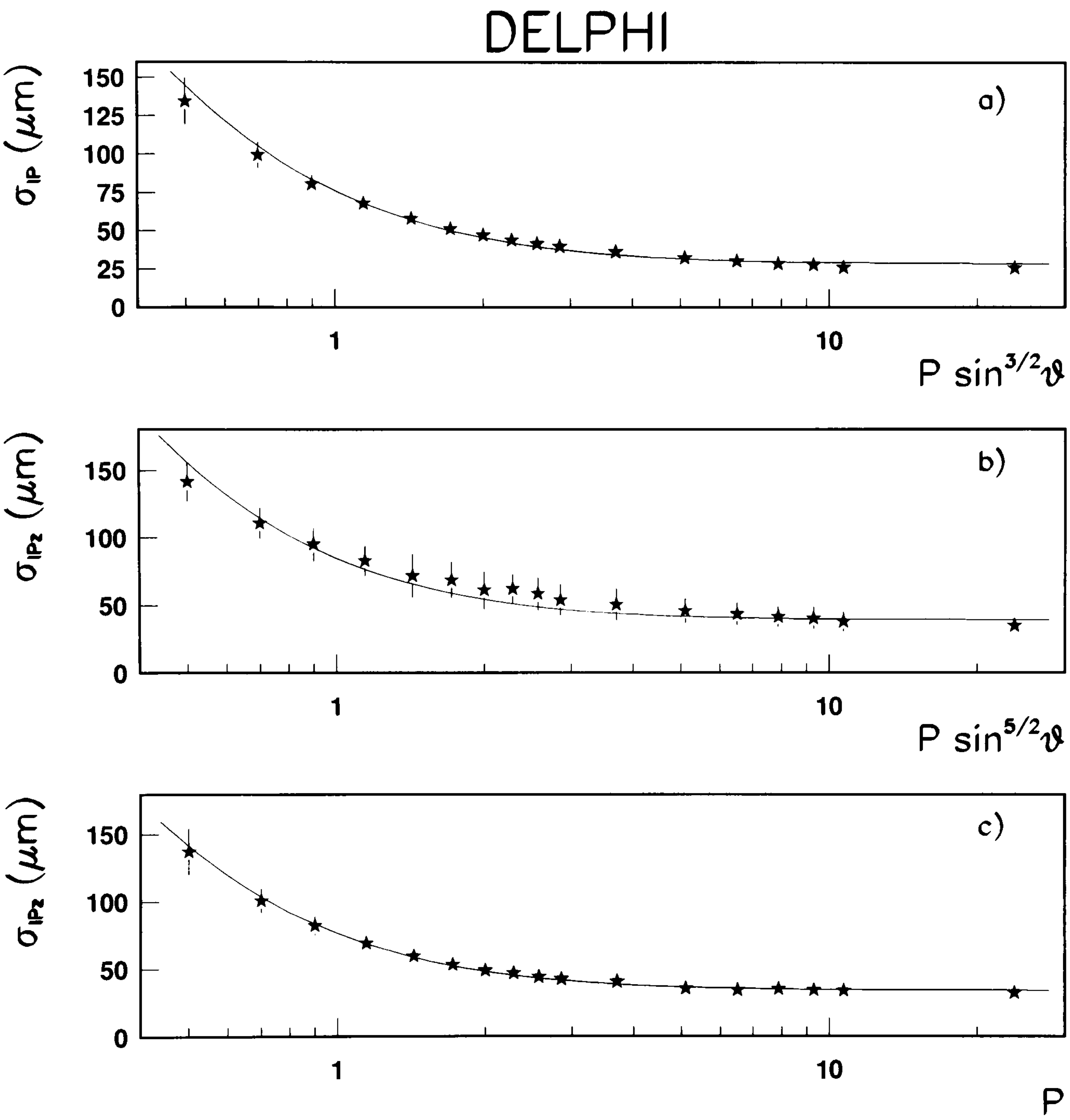

Figure 2.7: The resolution on the Impact parameter as a function of the p $\sin^{\frac{3}{2}}\theta$ (upper plot),the rz IP resolution as a function of p $\sin^{\frac{5}{2}}\theta$ (middle plot) and the rz IP resolution as a function of p for tracks with $\theta = [80° : 100°]$, i.e. perpendicular to the beam direction (lower plot). This figure was obtained from[21].

2.4.4 Silicon Tracker - Performance

The silicon tracker performance and the quality of the alignment can be assessed by looking at residuals between overlapping modules, track hit residuals, and impact parameter resolutions. Here we concentrate on the impact parameter resolution performance, which is of direct relevance for the tagging of heavy flavour decays. In figure 2.7 the impact parameter resolution in $R\phi$ is shown as a function of momentum. It is fitted with the function $28\mu\mathrm{m} \oplus 71/(\mathrm{p}\sin^{\frac{3}{2}}\theta)$, where p is the track momentum in GeV/c. Figure 2.7 shows the corresponding measurement in Rz and is shown for simplicity for perpendicular tracks only. It is fitted with the function $34\mu\mathrm{m} \oplus 69/(p\sin^{\frac{3}{2}}\theta)$. In both of these cases the first term is an asymptotic value which depends on how close(x) is the first layer of the VD to the interaction point and how far(d-x) is the furthest layer from the first layer. Ideally, x should be as small as possible and d-x as large as possible. The second term contains the effects of multiple scattering which depends on the normal component of momentum. Using the appropriate geometric factors effective hit precisions can be extracted of 8μm and 9μm in the $R\phi$ and z coordinate, respectively, which is close to what is expected.

2.5 Other aspects of the tracking system

The primary role of the ST in this thesis is in its heavy flavour tagging capabilities. Other tracking detectors are however equally important to the DELPHI performance, providing triggering, pattern recognition and enabling the momentum to be reconstructed. The essential characteristics of all the tracking detectors are given in table 2.2.

2.5.1 Inner Detector

The inner detector(ID) consists of two parts. The jet chamber and the trigger layer. The jet chamber consists of a drift volume filled with CO_2 and a small mixture of

Barrel	Radius (cm)	Polar Acceptance (°)	Resolution (μm)	Max No. of hit points
VD	$6.6, 9.2, 10.6$	> 21	$8(R\phi), \geq 10(z)$	6
ID				
– jet ch.	$12 \rightarrow 23$	> 15	$85(R\phi)$	24
– straws	$23 \rightarrow 28$	> 15	2300	5
TPC	$40 \rightarrow 110$	> 20	$250(R\phi), 880(z)$	3 [16] (space) 192 (dE/dx)
OD	$197 \rightarrow 206$	> 42	$110(R\phi)$, 3.5 cm(z)	5
MUB	$445 \rightarrow 485$	> 53	$1500(R\phi)$, 1 cm(z)	4
Forward	$\lvert z \rvert$ (cm)			
VFT		$10 \rightarrow 25$	100	4
FCA	160	$11 \rightarrow 32$	270	6
FCB	275	$11 \rightarrow 36$	300	12
MUF	$70 \rightarrow 480$	$9 \rightarrow 43$	1000	4

Table 2.2: DELPHI tracking and muon detectors. The symmetric polar acceptance in the other hemisphere is assumed.

isobutane. The drifted electrons are read out using a plane with 24 sectors of 15 ° in ϕ. Each sector has 24 sense wires which measure the drift time such that a particle may have up to 24 points in the $r\phi$ plane. The trigger layer consists of 5 cylindrical layers of straw tubes. Each tube contains 192 wires and 192 cathodes. The straws give $r\phi$ information and help resolve left-right ambiguities in the jet chamber.

2.5.2 Time Projection Chamber

The Time Projection Chamber(TPC) is DELPHI's main tracking chamber. It is a large chamber (R=120cm, L=2 × 150cm) filled with Ar and CH4 in a 4 to 1 mixture. It has a high voltage plate in the centre which supplies a uniform electric field parallel to the beam pipe direction of 150 V/cm and a drift velocity of 66.94 mm/μs. When a charged particle passes through the chamber it ionizes the gas mixture and liberates electrons which follow the field lines to the readout plane. The readout plane is divided into 6 sectors plates with 16 circular pad rows and 192 sense wires. The drifted electrons ionize the gas as they come very close to the wires. The ions produced then drift into the negatively charged pad placed 4 cm further away. The signal is transmitted by the TPC's 22464 electronic channels. There are 2304 channels for the wires and 20160 for the pads. By measuring the time taken for the electrons to reach the wires the distance in z can be calculated. The 3-D position of the track is determined using the position of the associated charged pad. A "dE/dX" measurement, which gives the particle's energy loss with distance and thereby contributes to the particle identification decision, is extracted from the amount of current produced in the wires along the $r\phi$ plane. This current is proportional to the number of incoming drifting electrons which depends on the particle's velocity.

2.5.3 Outer Detector

The outer detector(OD) is the tracking detector at furthest radius, positioned next to the first calorimeter detector and behind the RICH detector. It is designed to improve the momentum resolution of fast particles by adding more points further out in the particle's trajectory. The OD consists of 24 modules. Each module has 145 drift tubes in 5 layers. All layers provide $r\phi$ information and 3 also provide the z coordinate from the relative time of the signal arrival at both ends of the wire.

2.5.4 FCA

Forward chamber A(FCA) is mounted at both ends of the TPC. Each side consists of 3 chambers. A chamber is made out of 2 layers of drift tubes of 15×15 mm^2 in size operated in limited streamer mode. The chambers are rotated by 120° with respect to each other. The chambers provide 2×3 coordinates per track.

2.5.5 FCB

Forward chamber B(FCB) is made out of 4 modules, 2 on each side. It is positioned in a place analogous to that of the OD in the Barrel. Each module consists of 12 half discs sense-wires planes. The planes are positioned in 3 different orientations rotated 120 ° with respect to each other. The chambers provide 12 coordinates per track.

2.5.6 Momentum precision

The momentum precision of the tracking system in the barrel region is illustrated in figure 2.8(a) which shows the measured inverse momenta of muons from $Z \to \mu^+\mu^-$ decays. Here the in acollinearity of the two muons is required to be below 0.15° in order to remove radiative Z^0 decays. The tracks contain information from all the barrel detectors(VD,ID,TPC,OD).

The distribution can be fitted to the sum of two Gaussians. A width of:

$$\sigma(1/P) = 0.57 \times 10^{-3}(\mathrm{GeV/c})^{-1} \tag{2.1}$$

is obtained for the narrower Gaussian. The tails of the distribution require the wider Gaussian which accounts for 8% of all events and has a width of 1.04×10^{-3} $(\mathrm{GeV/c})^{-1}$.

A similar plot for muons in the forward region seen in at least the close layer of the VD and in FCB is shown in figure 2.8(b), where a precision of:

$$\sigma(1/P) = 1.31 \times 10^{-3}(\mathrm{GeV/c})^{-1} \tag{2.2}$$

is measured. Table 2.3 summarizes the momentum precision for dimuons events in different polar angle regions and with different combinations of tracking detectors included in the fitted track.

2.6 Calorimetry and Particle Identification

In this thesis, in chapter 5, the presence of isolated leptons is used to distinguish semi-leptonic W^+W^- events from $e^+e^- \to q\bar{q}(\gamma)$ production. The identification of

θ°	Detectors	$\sigma(1/P)(\text{GeV/c})^{-1}$
>42	VD+ID+TPC+OD	0.6×10^{-3}
>42	ID+TPC+OD	1.1×10^{-3}
>42	VD+ID+TPC	1.7×10^{-3}
<36	VD+FCB included	1.3×10^{-3}
25-30	FCB included	1.5×10^{-3}
<25	FCB included	2.7×10^{-3}

Table 2.3: Momentum measurement precision for 45.6 GeV/c muons.

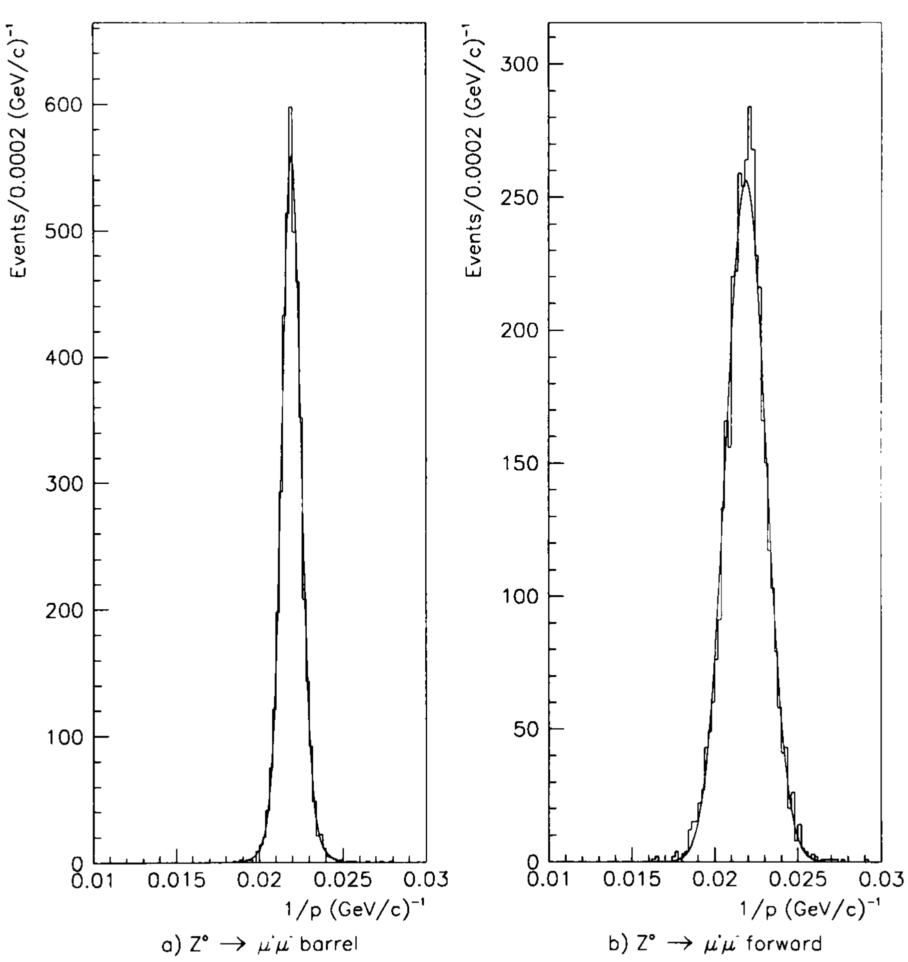

Figure 2.8: Inverse momentum distributions for collinear muons from $Z \rightarrow \mu^+\mu^-$ decays: (a) tracks containing hits from VD,ID,TPC and OD, (b) forward tracks containing hits from at least the VD and FCB. This figure was obtained from[10].

Barrel	Radius (cm)	Polar acceptance	typical resolution $\sigma(E)/E$ (E in GeV)
HPC	$208 \rightarrow 260$	$\geq 43°$	$0.043 \oplus 0.32/\sqrt{E}$
HCAL	$320 \rightarrow 479$	$\geq 43°$	$0.21 \oplus 1.12/\sqrt{E}$
Forward	$\|z\|$ (cm)		
FEMC	$284 \rightarrow 340$	$8 \rightarrow 35°$	$0.03 \oplus 0.12/\sqrt{E} \oplus 0.11/E$
STIC	$220 \rightarrow 260$	$1.7 \rightarrow 10.6°$	3% @ 45 GeV

Table 2.4: DELPHI calorimeters. The symmetric polar acceptance in the other hemisphere is assumed.

electrons, by electromagnetic calorimetry, and muons by the muon chambers and the hadron calorimeter is therefore very important. Calorimetry also provides information for the jet reconstruction.

The energy of electrons and photons can be measured through the Coulomb interaction of an electron with a nucleus and e^+e^- pair production. An electron decelerates in the Coulomb field, emitting a photon; the photon can pair produce and an electro-magnetic shower can evolve. In DELPHI there are individual electromagnetic calorimeters in both the barrel and the forward regions.

2.6.1 High Density Projection Chamber

The High Density Projection Chamber(HPC) is the barrel DELPHI electromagnetic calorimeter and consists of 144 modules arranged in 6 rings of 24 modules each. Each module is a trapezium shaped box with 41 layers of lead separated by gas gaps. When a particle makes an electro-magnetic shower in the lead, the gas in between the lead layers is ionized. The electrons drift along an electric field of 100 V/cm lines along the lead layers where they are collected by proportional wire chambers. This novel technique allows 3D space points to be reconstructed in a TPC-like manner with good precision which enables the shower evolution to be studied.

2.6.2 Forward Electromagnetic Calorimetry

The Forward Electromagnetic Calorimetry(FEMC) consists of 4532 blocks of lead glass. The blocks are truncated pyramids with inner (outer) face dimensions of 5.0x5.0 (5.6x 5.6) cm^2 and depths of 40 cm. The energy of a charged particle passing the block is determined by collecting the Cherenkov light it emits. The number of photons emitted is proportional to the particle's energy. More features about the FEMC and the other DELPHI calorimeters are shown in table 2.4.

2.6.3 Hadronic Calorimetry

The aim of the Hadronic Calorimetry(HCAL) is to measure the hadron's energy by stopping their motion and measuring the energy produced. Minimum ionising muons on the other hand leave a trail of energy. The HCAL covers the barrel and the end caps and is incorporated into the iron return yoke of the super-conducting solenoid magnet. There are 20 (19) layers of limited streamer mode detectors inserted into 2cm slots between 5cm iron plates in the barrel (forward) region. A streamer mode detector consists of a plastic cathode forming 8 cells of 0.9x0.9cm with one anode wire. The readout boards are segmented into pads; these pads are combined to form "towers" pointing to the interaction point. The HCAL readout geometry is illustrated in Figure 2.9.

2.6.4 Muon Chambers

The muon detection in DELPHI consists of three sub-detectors : the barrel, the forward and a component which covers the gap between the barrel and the end-cap regions, termed the 'surround'. The coverage and the resolution of the muon system is summarized in table 2.2.

Barrel Muon Chambers

The barrel muon detector(MUB) was built and maintained by the Oxford Group. The detector consists of three layers of muon chamber modules, and is divided into

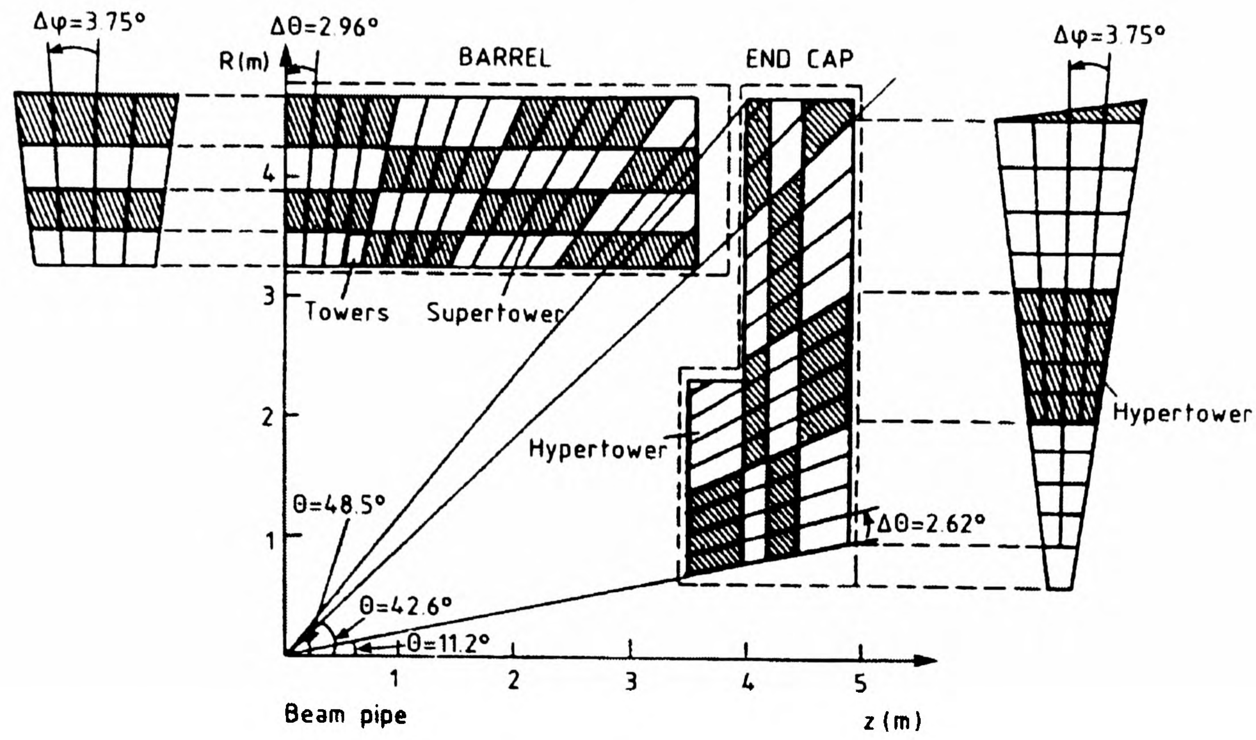

Figure 2.9: A diagram showing the readout geometry of the HCAL.

24 azimuthal sectors. A sector is arranged such that the inner modules lie 20 cm inside the iron of the Hadron Calorimeter, and the outer modules outside the iron. The peripheral modules are arranged to cover the gaps between the previous two layers of modules. Each module layer consists of 2 or 3 staggered layers of drift chambers, thus resolving the inherent left-right ambiguity of drift chambers. A diagram of a sector of the MUB is shown in figure 2.10.

Forward Muon Chambers

The forward muon detectors(MUF) consist of two detection planes, one 20cm inside the iron of the forward HCAL, the second outside. Each plane consists of two orthogonal layers of drift chambers. The anode signal timing provides one co-ordinate and the timing of a delay line signal is used to obtain the orthogonal co-ordinate.

Surround Muon Chambers

The surround muon chambers(MUS) cover the gap between the MUB and MUF chambers at a polar angle of around 45°. At each end of DELPHI eight chambers are attached in pairs to the edges of the end-caps. The chambers on the top and sides of the end-cap are inclined at 45° to obtain the maximum angular coverage.

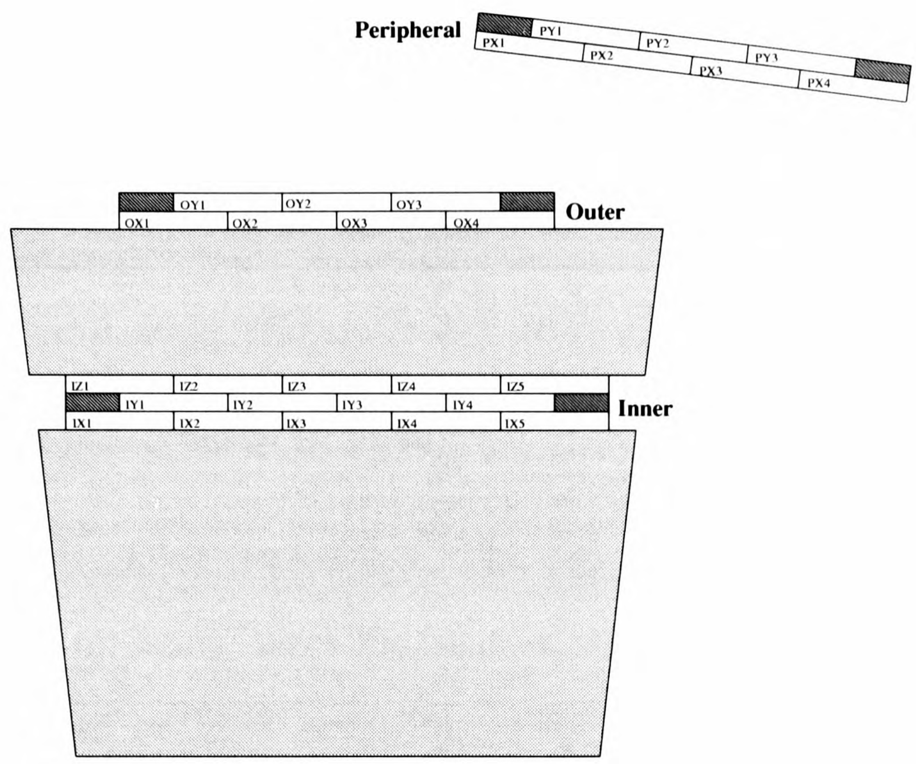

Figure 2.10: An azimuthal sector of the DELPHI barrel muon chambers. The dark part represents the iron of the Hadron Calorimeter and the figure shows how the modules are arranged.

Each module is comprised of two staggered layers of streamer tubes. The tubes are the same as those used in the HCAL.

2.6.5 Electron identification

Electrons are reconstructed using the REMCLU package[12]. This uses several approaches to electron identification, depending on the momentum and polar angle regions being considered.

In the barrel regions, tracks with a momentum less than 30 GeV are passed through the ELEPHANT[26] package. This uses the energy-momentum ratio, the energy loss(dE/dX) from the TPC, the shower profile from the HPC, and the matching between the shower and the track to identify electrons. Electrons are tagged as 'loose', 'standard' or 'tight' according to a combination of the above quantities.
For tracks with momentum greater than 30 GeV, photon candidates close to the track are associated to it as possible hard bremsstrahlung products. The energy of the HPC shower must exceed 10 GeV, and the ratio of the measured energy to the

Tag	Efficiency %	Misid. Prob %
Loose	80	1.6
Standard	55	0.4
Tight	45	0.2

Table 2.5: Electron identification efficiency and misidentification probabilities (P > 3 GeV) in multihadronic events for each tag in the barrel region. This table is obtained using real data and is taken from[10].

measured track momentum must exceed 0.5. The estimate of the electron energy uses a combination of the measured track momentum and the HPC energy. Electron candidates are tagged 'loose' or 'tight' according to the associated HCAL energy deposit.

In the forward region, the identification starts by clustering energy deposits in the FEMC crystal. If a track is found to give a good match with this cluster, it is identified as an electron, otherwise as a photon. The electron is tagged as 'tight' or 'loose', depending on the number of hits in the various subdetectors which are associated to the track. Table 2.5 shows typical efficiencies and misidentification probabilities.

2.6.6 Muon identification

The main tool used for the muon identification are the muon chambers. The MUFLAG[27] package matches muon chamber hits to tracks taking account of the expected multiple scattering in the HCAL iron of a minimum ionising particle. Depending on the number of muon chamber hits and the quality of the fit between them and the track, the track is flagged as a 'tight', 'standard', 'loose' or 'very loose' muon. Tracks which give an energy deposit in the HCAL consistent with that of a minimum ionizing particle are tagged as 'HCAL' muons: these do not necessarily have muon chamber hits associated to them. Further details can be found in [13]. Table 2.6 shows the muon efficiency and misidentification probabilities for the four tags[14].

Tag	Efficiency %	Misid. Prob %
Very loose	95	5.4
Loose	95	1.5
Standard	86	0.7
Tight	76	0.4

Table 2.6: Muon identification efficiency and misidentification probabilities for each tag. The identification efficiencies have been determined in $Z \to \mu^+\mu^-$ decays in the barrel region. This table was obtained from[10].

2.6.7 RICH Imaging Cherenkov Counter

The Ring Imaging Cherenkov counter(RICH) is designed to discriminate between particles through the imaging of the Cherenkov ring. This detector is situated between the TPC and the OD in the barrel region, and between forward chamber A and B in the endcaps. The RICH is not used for the analysis presented in this thesis.

2.7 Luminosity measurement

The luminosity is determined by counting the number of Bhabha scattering ($e^+e^- \to e^+e^-$) events at small angles. This is a good process to measure the luminosity since it is predominantly QED interaction with a small theoretical error and high cross-section. The electrons are detected using the Small angle Tile Calorimeter(STIC). The theoretical error and the systematic error due to detector effects on the measured luminosity are 0.25% and 0.50% respectively.

STIC

The STIC is made of 47 layers of 3mm lead and 3mm scintillator tiles. An electromagnetic shower arises in the lead and produces scintillation light. The scintillator layers are readout using a set of wavelength shifter fibers going through the lead/scintillator planes. The reconstruction of the shower direction is improved by

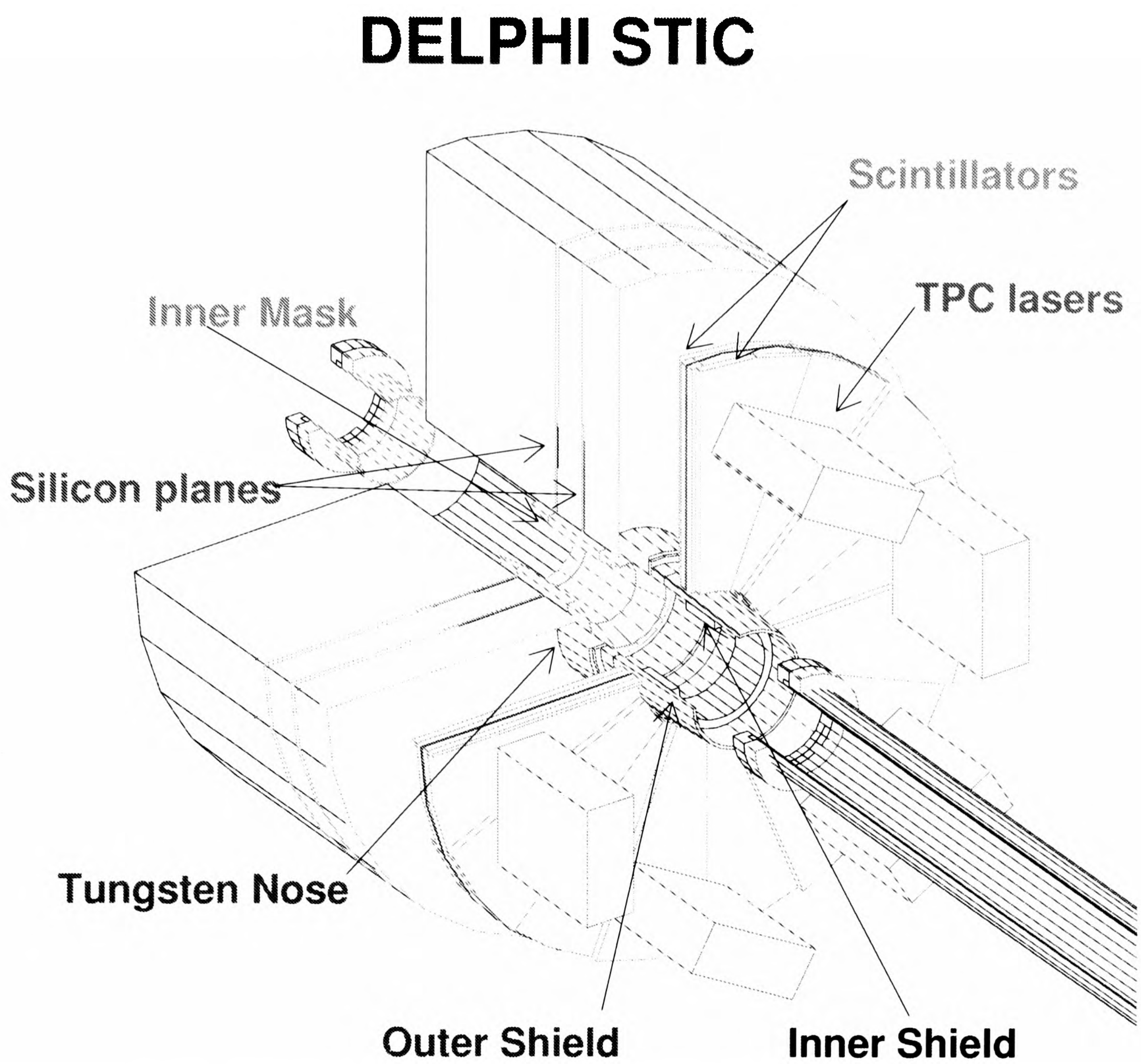

Figure 2.11: A cut-away diagram of the STIC.

adding two planes of silicon inside the calorimeter. A diagram of STIC is shown in figure 2.11. More features about the STIC can be found in table 2.4.

2.8 Trigger

The role of the DELPHI triggering system[15] is to select events with potential physics interest from out of the background. The beam crossing rate of 45,000 Hz has to be reduced to the desired readout and storage rate of a few Hz. The trigger system consists of 4 stages of increasing selectivity(T1 $\rightarrow$ T4). The T1 decision is taken 5 μs after the beams interact. The detectors contributing to T1 are the fast tracking detectors ID,OD,FCA,FCB , HPC scintillators, EMF,and MUB. A T2 decision is made after 39 μs and is based on TPC,HPC,MUF and also includes combinations from additional detectors. The trigger rate after T2 is typically 5 Hz. The third and fourth level triggers are software triggers, and are asynchronous with the beam crossing. The T3 stage repeats the T2 logic using more detailed detector information and halves the T2 trigger rate. T4 rejects events without tracks pointing to the interaction region or significant energy deposits in the calorimeters. This final trigger level again roughly halves the trigger rate. The trigger is estimated to be essentially 100% efficient for the processes of interest for this thesis[15].

2.9 Offline processing and Simulation

The raw data are written out by the data acquisition system. The raw data consist of the unprocessed digitized signals from each of the detectors for each event passing the trigger. The data are then processed by a program called DELANA[16] to make them suitable for physics analysis. DELANA processing consists of connecting hits in individual sub-detectors to make spatial points per tracks called track elements(TE's). A global track reconstruction is then performed by connecting the TE's from different sub-detectors. The principal algorithm starts with the TE's from the TPC and attempts to match them with TE's in the ID and OD. Other algorithms look for different detector combinations. The track found by the above search then passes the full track fitting, based on a Kalman filter technique, which takes into account multiple scattering and energy loss in the detector material.
Any calibration of the data is done at this stage. Preliminary classification into classes of events and particle(such as muon or electrons) and identification is also performed. The output of `DELANA` is a Data Summary Tape (DST) which is the starting point for the analysis presented in this thesis. The b tagging, central to this thesis, is run at the analysis stage on the DST.

Detector simulation

The DELPHI detector simulator program(DELSIM[17]) aims to simulate events passing through the DELPHI detector. Final state particles from the physics Monte

Carlo(MC) generator pass through the simulator in order to produce events as close as possible to the real data observed. The simulator propagates the events through the various parts of the detector and follows particle decays and secondary interactions with the detector material. The simulated responses are then passed through the usual DELANA program.

MC Generators

In the analysis, simulated data are used to model the real data observed. The resemblance of the final result to the real data reflects the theoretical knowledge of the physical processes occurring. The event generator produces a full set of particles for a given physical process. There are 3 stages in generating an event: the primary process, the fragmentation and the hadronisation processes. The primary process of importance for the analysis presented here is $e^+e^- \to q\bar{q}(\gamma)$. The generators used are PYTHIA[18] and KK2F[37] for the production of the $q\bar{q}$ pairs and JETSET[19] for the fragmentation and hadronisation processes. As a cross check the ARIADNE[35] MC is used. This MC has a different QCD cascade process and uses PYTHIA and JETSET for the rest.

3. Event Selection and the b tag

3.1 Introduction

This chapter describes the event selection of a non-radiative hadronic sample and subsequent isolation of b quark events, the main background and relevant detector performance. The event selection described here also sets the basis for the c selection discussed in chapter 5.

3.2 The data set

The starting point for analyzing the data set is the Data Summary Tapes(DST) produced by DELANA[16] from the basic detector signals. The SKELANA[38] program, which is another standard DELPHI software package, runs over the DST to produce common blocks containing information from the various sub-detectors and of the reconstructed tracks. In the event selection information from several common blocks was used. The data sets analyzed were taken during the 1997-2000 LEP2 operation.

3.2.1 Track and Hadronic selection

The initial cuts made are the track selection in the event. The purpose of this selection is to isolate well measured charged and neutral tracks suitable for physics analysis. For charged tracks the cuts are:

- Polar angle is between 11°-169°. This defines a volume with reliable tracking.
- The relative error on the momentum measurement is less then 100%. This is to exclude badly measured tracks.

and for neutral tracks:

- A minimum energy cut is applied, which is 0.3 GeV for the barrel electromagnetic and small angle calorimeters HPC and STIC, and 0.4 GeV for the electromagnetic calorimeters in the forward region, FEMC. This motivation these values was noise in the detector.

The next selection stage aims to select a sample enriched in high energy hadronic events. This is done by the set of cuts listed below:

- Require total charged energy in the polar range 10°-170° of greater than 15 GeV. This is to ensure that the event is contained in a region of the detector with good tracking performance.

- Require at least 7 charged tracks in the event. This is to insure a minimum number of particles in the event and to reduce tau-tau and $\gamma\gamma$ background.

- Require less than 85% of beam energy in the forward region. This is to reject bhabha scattering events in which most of the energy is contained near the beam pipe.

- Require that the $q\bar{q}$ production axis, as estimated by the thrust direction(discussed in more details in chapter 4) is between 25° and 155°. This is to ensure that the event is in the region of good detector operation.

3.2.2 Characteristics of $e^+e^- \to q\bar{q}(\gamma)$ and sources of background

The general characteristics of a $q\bar{q}(\gamma)$ event is two or more jets of hadrons. An example of such a hadronic event is shown in figure 3.1.

The main source of background is W^+W^- events but there is also a contribution from Z^0Z^0 and tau-tau events.

- **W^+W^- events**

  The significant background from W^+W^- events splits into two categories: fully hadronic and semi-leptonic decays. The fully leptonic decays are easily removed through multiplicity requirements. A W^+W^- pair, however, decaying into 4 quarks produces hadronic events that can superficially resemble a $q\bar{q}(\gamma)$ event. In a semi-leptonic W^+W^- decay the hadronic decay of one W may also be similar to a $q\bar{q}(\gamma)$ event.

- **Z^0Z^0 events**

  Z^0Z^0 events, in which one or two Z^0 bosons can decay into $q\bar{q}$ pair can present a hadronic background to $e^+e^- \rightarrow q\bar{q}(\gamma)$ events.

- **Tau-Tau**

  In such events the tau's may decay hadronically, also giving a two jet topology.

Other backgrounds from low multiplicity lepton events, $\gamma\gamma$ collisions and beam gas interactions are suppressed to negligible levels by the hadronic selection. This was established by applying the the hadronic cuts on a MC sample of these backgrounds.

3.2.3 W^+W^- rejection and jet clustering

Jet Clustering

The tracks in the event are arranged in groups of particles called jets. This is done in an attempt to associate together tracks which originated from the same quark. The motivation is to help in the W^+W^- rejection, discussed here, and to provide input for the b tag, discussed in section 3.3. The $\sqrt{S'}$ reconstruction described in section 3.2.4, also uses jets, but with a separate clusterisation algorithm.

The basic procedure in the clusterisation is to link tracks according to some distance

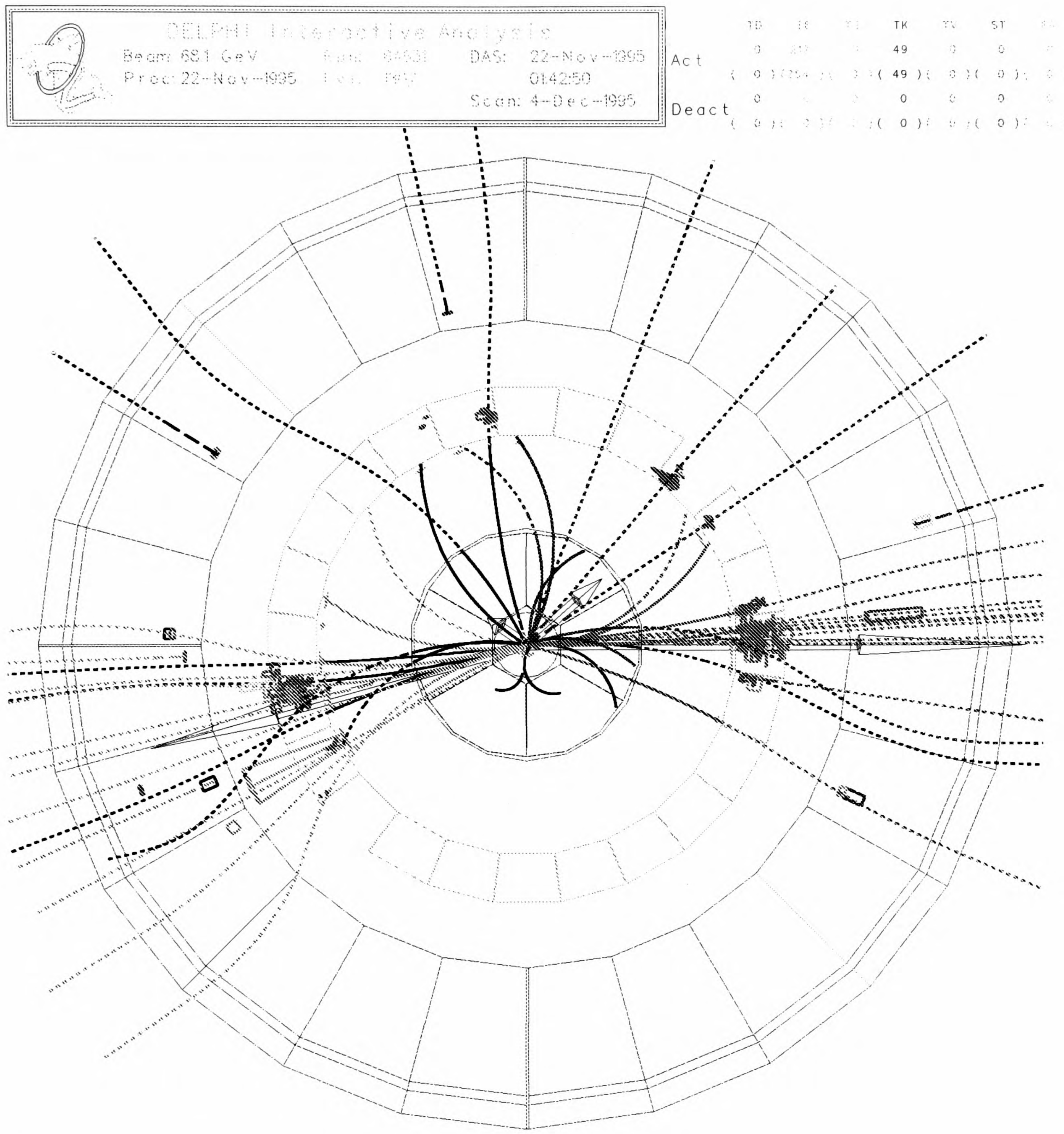

Figure 3.1: A $q\bar{q}$ event in the rϕ view. One can see the reconstructed particles path.

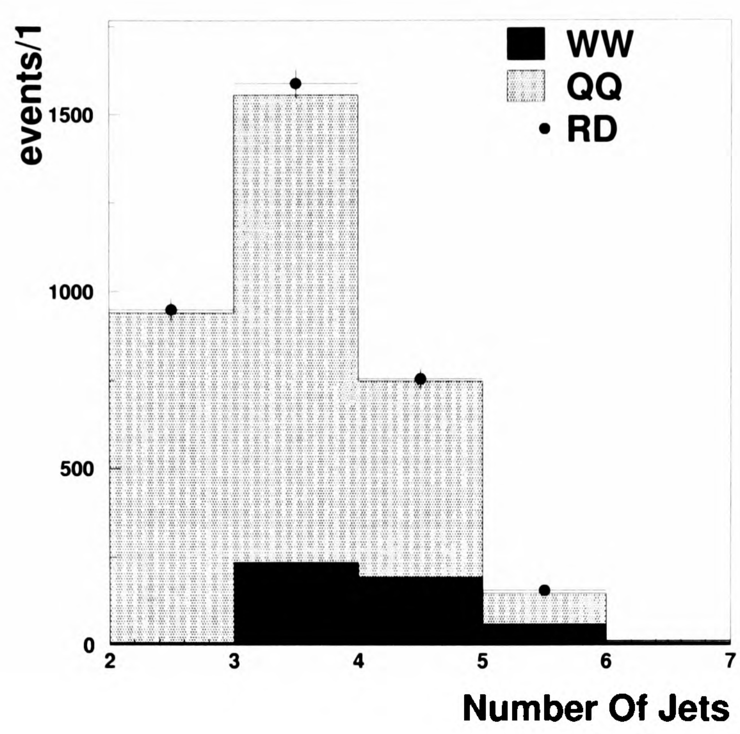

Figure 3.2: The number of jets per event clustered using the LUCLUS[19] algorithm for 1998 data. RD refer to Real data events.

definition; if the distance is below some cut-off value the tracks are associated together in the same jet. The jet is seeded from the pair with the minimum distance of separation and the associating procedure continues until all tracks satisfying the cut-off value are included. The jet clustering algorithm used in this analysis is the LUCLUS[19] algorithm. The distance between tracks i and j is defined as d_{ij}^2 where:

$$d_{ij}^2 = \frac{4|p_i|^2|p_j|^2\sin^2(\theta_{ij}/2)}{(|p_i|^2 + |p_j|^2)}, \tag{3.1}$$

where p is the track's momentum and θ is the angle between the two tracks. Both charged and neutral tracks participate in this procedure. The distance cut-off value used in the analysis presented here is $d_{ij}^2 = 5$ GeV^2. Most of the events are clustered into 2 or 3 jets but there are also events with 5 or more jets. The distribution of the number of jets clustered is shown in figure 3.2 for the 1998 data set.

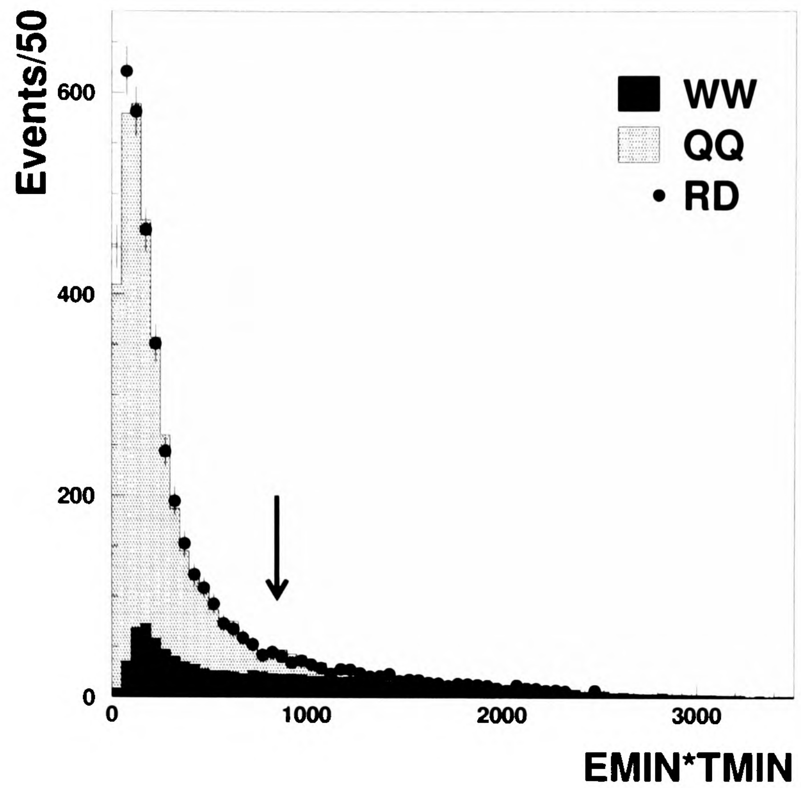

Figure 3.3: Distribution of $E_{min} * \theta_{min}$ for 1999 data set. The arrow shows the cut above which events were rejected.

Anti W^+W^- cut

In order to suppress some of the W^+W^- events a cut on $E_{min} * \theta_{min}$ is applied. This cut is made with the jet of minimum energy in the event and the minimum angle between that jet and the other jets. This cut is aimed to suppress W^+W^- events where the jets are well separated, from $q\overline{q}(\gamma)$ events with hard gluon radiation in which the gluon jet is less isolated and is less energetic than the other jets. This variable is shown in figure 3.3 together with the cut above which events were rejected. This cut is equally effective in suppressing Z^0Z^0 background.

3.2.4 Selection of non-radiative events

In a large fraction of the events a photon is emitted from the initial electron or positron(ISR) reducing the energy available for the $q\overline{q}$ pair. An example radiative event is shown in figure 3.4 where the ISR photon can be clearly seen, and the two jets are no longer back to back. The photon often travels undetected inside the beam pipe.

This thesis is concerned with $b\bar{b}$ and $c\bar{c}$ events at high energy, so events in which the ISR significantly reduces the effective energy left for the quarks need to be rejected.

Estimating the centre of mass energy($\sqrt{S\prime}$) is done in several stages. Firstly, each event is forced into 2 jets by adjusting the value of the parameter d_{join} in the LUCLUS[19] clusterisation algorithm. The value of $\sqrt{S\prime}$ is derived from the polar angles of the jet directions (θ_1, θ_2), assuming that a single ISR photon was emitted along the beam pipe. In this topology the reduced centre of mass energy is given by the following expression:

$$S\prime = S - 2E_\gamma\sqrt{S} \tag{3.2}$$

where E_γ is the ISR photon energy:

$$E_\gamma = \frac{|\sin(\theta_1 + \theta_2)|\sqrt{S}}{\sin\theta_1 + \sin\theta_2 + |\sin(\theta_1 + \theta_2)|} \tag{3.3}$$

When an isolated energetic photon is reconstructed in the electromagnetic calorimeters the value of $\sqrt{S\prime}$ is computed from the measured photon energy. Figure 3.5 shows the distribution of $\sqrt{S\prime}$ / $\sqrt{S}$. The distribution shows that in about half of the events the effective centre-of-mass energy is reduced back to the Z^0 energy and hence not useful for the high energy analysis presented here.

The selection of events for the high energy analysis presented here is performed by applying a cut on the measured centre of mass energy $\sqrt{S\prime}$ such that $\sqrt{S\prime} > 0.85\sqrt{S}$.

Table 3.1 shows the real data and MC number of events selected after the hadronic, W^+W^- rejection and $S\prime$ cuts. The numbers in the table indicate that there are

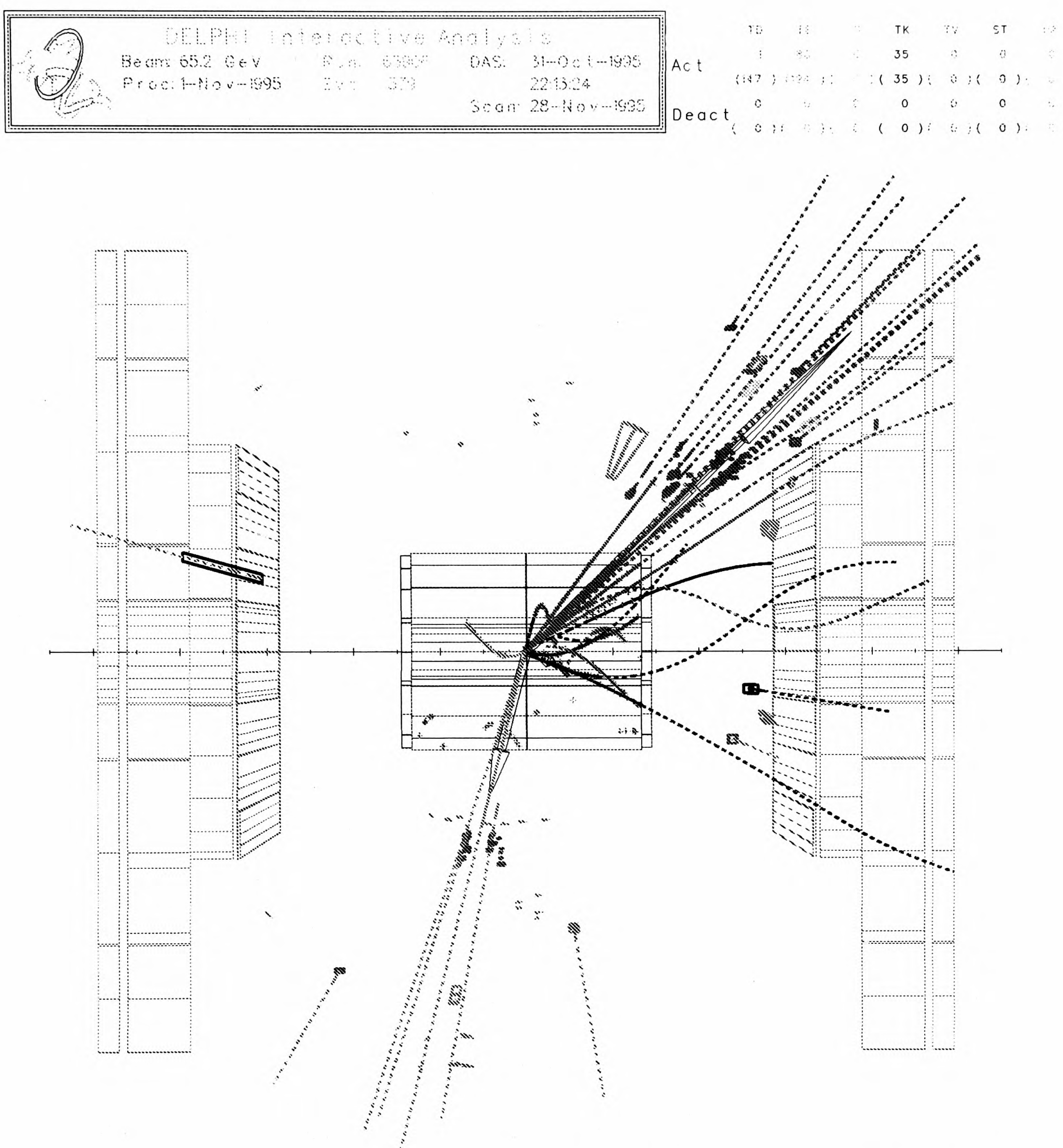

Figure 3.4: A $q\overline{q}(\gamma)$ event with ISR. The ISR photon can be seen in the left end cap. Against it we can see the two jets which are no longer back to back.

3% more data than expected. This is not inconsistent with the findings of the LEP wide average(40) which also sees an excess of this level. After all selection steps the agreement is good to 2%. This is acceptable for an asymmetry analysis as the A^b_{FB} measurement is not expected to be very sensitive to such a disagreement; furthermore in section 4.5.3 these data/MC discrepancies are allowed for by assigning conservative uncertainties in the background sources in the asymmetry measurement.

Table 3.2 shows the composition of the hadronic sample selected obtained from MC. We can see that the fraction of b events is about 0.15 of the entire sample and that the W^+W^- fraction increases with energy. This is due to the decrease of the $q\bar{q}$ cross section and the stability of the W^+W^- cross section with energy. The contamination from Z^0Z^0 events is very small and amounts to 1% of the final hadronic sample in all the years. The contamination from tau-tau events after all the cuts amounts to 0.3% of the sample(verified using MC) and is considered to be negligible.

3.2.5 Detector Inefficiency during 2000 data taking

During the last third of the data taking in 2000, corresponding, to an integrated luminosity of 58.01pb^{-1}, a twelfth of the main tracking detector(TPC) was not operational due to a short between the sense wires. As a consequence, although tracks in that angular region could still be reconstructed from hits in the other tracking devices, the track finding efficiency and track resolution were degraded in that sector[20]. In order to assess this effect a special simulation was generated for that period. Figure 3.6 shows the polar angle(Θ) of charged tracks. The Θ angle of the dead sector is between 270° - 330°, where a drop in the track efficiency can indeed be observed. The MC describes well the efficiency loss seen in the data.

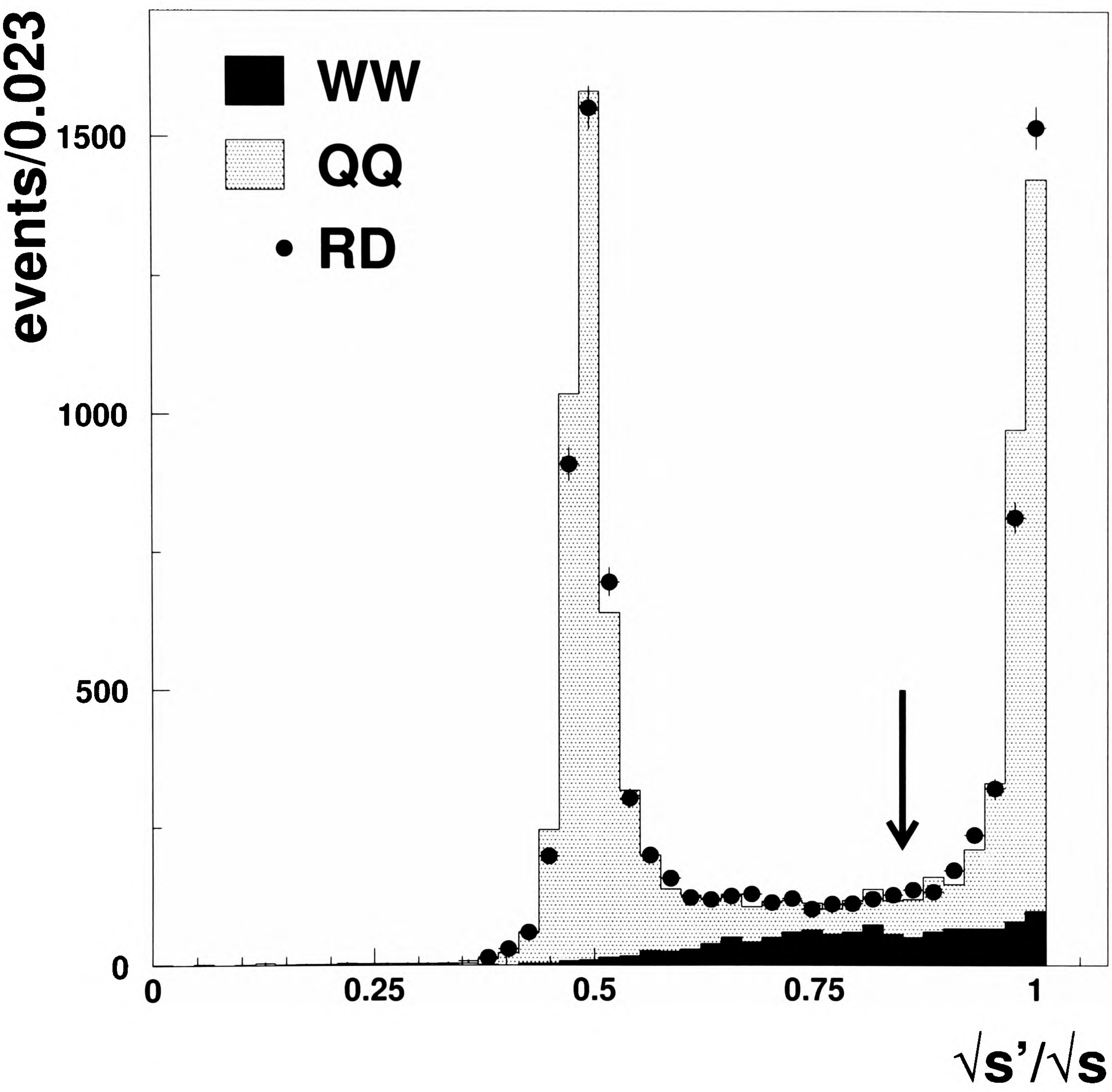

Figure 3.5: The distribution of $\sqrt{S\prime}$ / $\sqrt{S}$ for the 1998 data set. The arrow indicates the cut below which events are rejected.

	Int. Lum	Events after:			
	(pb^{-1})	hadronic cuts	W^+W^- rejec.	S' cut	b tag cut
RD 1997	53.67	4301	3735	1353	119
MC 1997		4049	3524	1285	129
RD 1998	154.99	10634	9251	3570	358
MC 1998		10738	9264	3462	382
RD 1999	228.33	14359	12275	4681	497
MC 1999		13327	11269	4483	441
RD 2000 (G)	161.88	8930	7513	3033	299
MC 2000 (G)		8562	7191	2961	278
RD 2000 (B)	58.01	3005	2544	1057	85
MC 2000 (B)		3038	2541	1088	91
Tot RD/MC		1.038 ± 0.007	1.045 ± 0.008	1.031 ± 0.012	1.024 ± 0.040

Table 3.1: Events remaining after successive stages in the event selection. The MC has been normalized to the data integrated luminosity. (G) and (B) refer to the good and bad TPC operation periods during 2000.

	Z^0Z^0	W^+W^-	uds fraction	c fraction	b fraction
1997	0.010 ± 0.000	0.135 ± 0.003	0.496 ± 0.004	0.214 ± 0.003	0.142 ± 0.003
1998	0.011 ± 0.000	0.144 ± 0.003	0.488 ± 0.004	0.214 ± 0.003	0.140 ± 0.003
1999	0.012 ± 0.000	0.176 ± 0.002	0.476 ± 0.003	0.204 ± 0.003	0.138 ± 0.002
2000 (G)	0.013 ± 0.000	0.192 ± 0.003	0.459 ± 0.004	0.210 ± 0.003	0.136 ± 0.003
2000 (B)	0.013 ± 0.000	0.190 ± 0.003	0.461 ± 0.004	0.204 ± 0.002	0.135 ± 0.003

Table 3.2: The hadronic sample composition in the 1997-2000 data sets according to the MC. (G) and (B) refer to the good and bad TPC periods during 2000. This is after all the stages in the event selection, apart from the b tag.

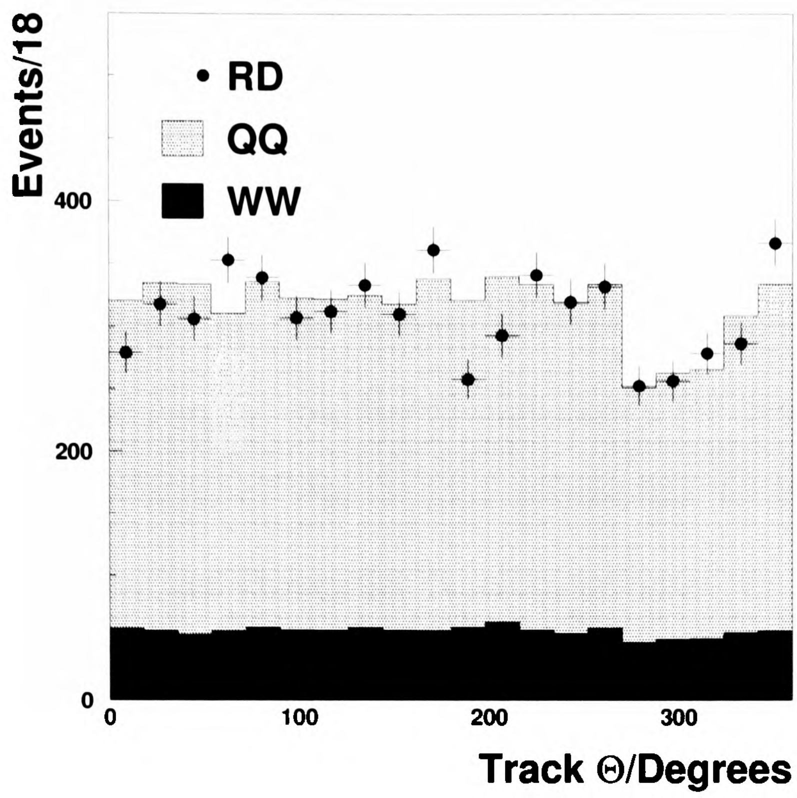

Figure 3.6: The polar angle(Θ) of charged tracks in the last period of 2000 running. A drop in the track efficiency is seen in both data and MC in the angular region between 270° - 330° where the dead TPC sector is.

3.3 b Tagging

After selecting a non-radiative hadronic sample it is now necessary to enhance the b composition. This section introduces the key variables used to separate b events, describes the common DELPHI technique[21] for optimally tagging b events, and shows data and MC comparisons.

3.3.1 Raw variables

The secondary decay of particles within jets can be studied using the vertex detector information. For events with evidence of a secondary vertex discriminating variables are constructed. This enables us to use the specific properties of the long lived b-hadrons and to separate their decay products from other tracks in the b event or from non-b events. In cases where a secondary vertex was not found the discriminating power of the variables was significantly reduced.

Before introducing the variables it is necessary to discuss some of the key quantities which serve as the building blocks of this analysis.

The track impact parameter

The impact parameter (IP) of a track has a very important role in heavy flavour physics. It is defined as the closest distance between the track path and the primary vertex, and can be calculated separately for the rϕ and rz planes as shown in figure 3.7. The sign of the impact parameter is defined from the projection with respect to the jet direction it is associated to. In principle the impact parameter should be zero for tracks that come directly from the primary vertex and non zero with a positive sign for tracks coming from secondary decays. In practice, since the detector reconstruction is not perfect and due to multiple scattering, the reconstructed impact parameter can be non-zero also for tracks coming from the primary vertex and thus is a measure of the detector resolution. Hence, with the above limitation, the impact parameter of a track can indicate if the track came from the primary vertex or from a displaced vertex. The track's significance is defined as the ratio between the IP and its assigned error(as discussed in chapter 2). Figure 3.8 shows the significance distribution in the rϕ plane for 2000 data. The b events have higher values than the background in this distribution.

The track probability

The track's significance is used to construct a quantity called a track probability. It is defined separately for the rϕ and rz planes using the significance distribution of tracks with negative sign IP. The distribution of tracks with negative IP contains mostly tracks originating from the Primary Vertex which were inaccurately measured or scattered in the detector material.

The track probability, P(S^0), is the probability, assuming the track came from the Primary Vertex, to have a significance S^0 or larger. P(S^0) is defined as:

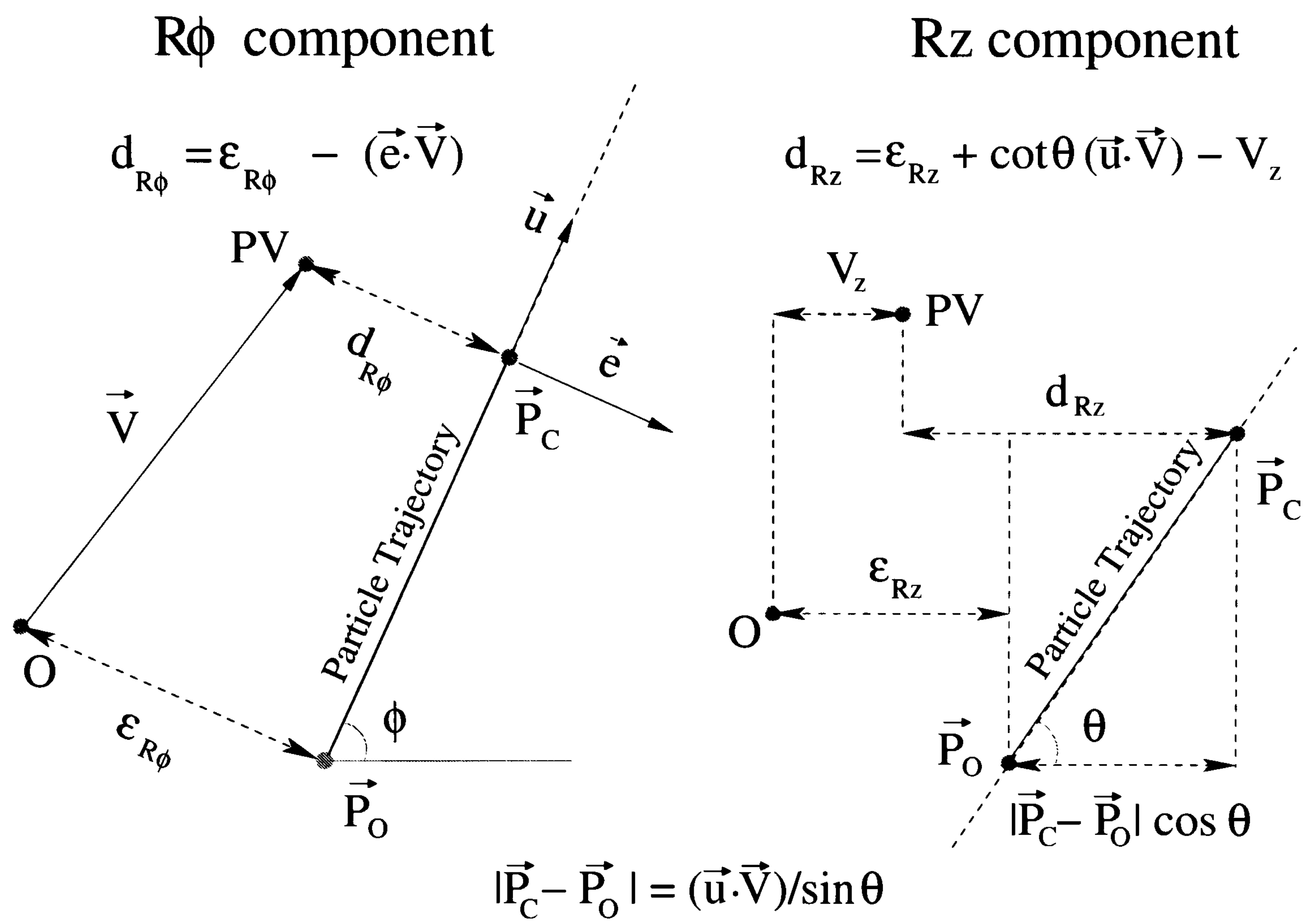

Figure 3.7: The impact parameter of a track is defined for the rϕ plane ($d_{r\phi}$) and z (d_z). O is the origin of the DELPHI coordinate system, PV is the position of the primary vertex on this coordinate system. $\vec{u}$ is a unit vector along the track direction, $\vec{e}$ is a unit vector perpendicular to $\vec{u}$ in the $r\phi$ plane, $\vec{v}$ is a vector from the origin to PV.

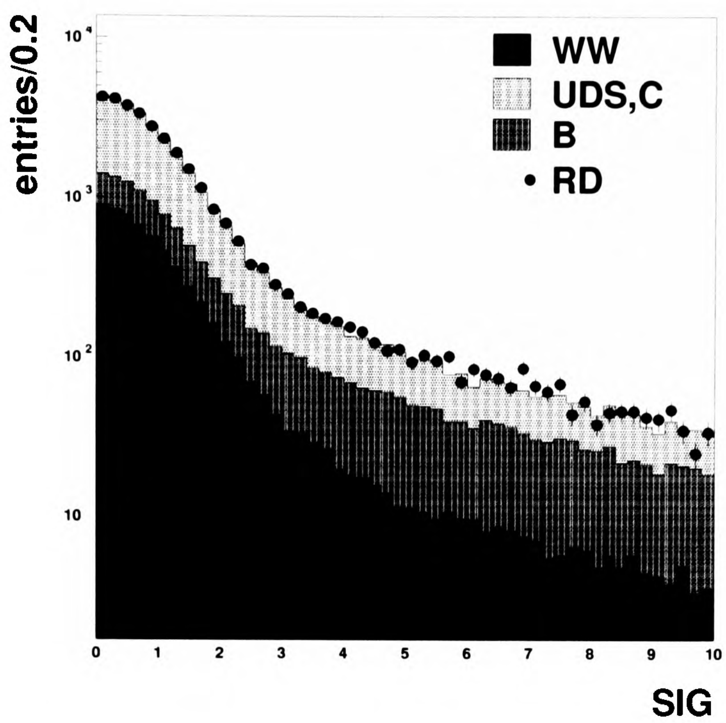

Figure 3.8: The distribution of the positive Impact Parameter significance in the rϕ plane for the 2000 data.

$$P(S^0) = \int_{S^0}^{\infty} f(S)dS \tag{3.4}$$

where f(S) is a fitted function to the negative IP significance distribution. f(S) is however assumed to be symmetric for both signs of IP. By definition, tracks originating from the primary vertex with positive and negative IP sign have a flat probability distribution. Figure 3.9 shows the track probability in rϕ and rz planes. The distributions shows spikes close to zero where b content is enhanced.

3.3.2 Reconstruction of Secondary Vertices

The event is split into two hemispheres according to the direction of the thrust axis. A search for a secondary vertex(SV) is then performed in each hemisphere separately. The secondary and primary vertex positions are simultaneously fitted in three dimensions, using the event primary vertex as a starting point and constrained to the flight direction of the b hadron. Here, the flight direction is obtained from the vector sum of tracks with rapidity(discussed in section 3.3.3) greater than 2.0.

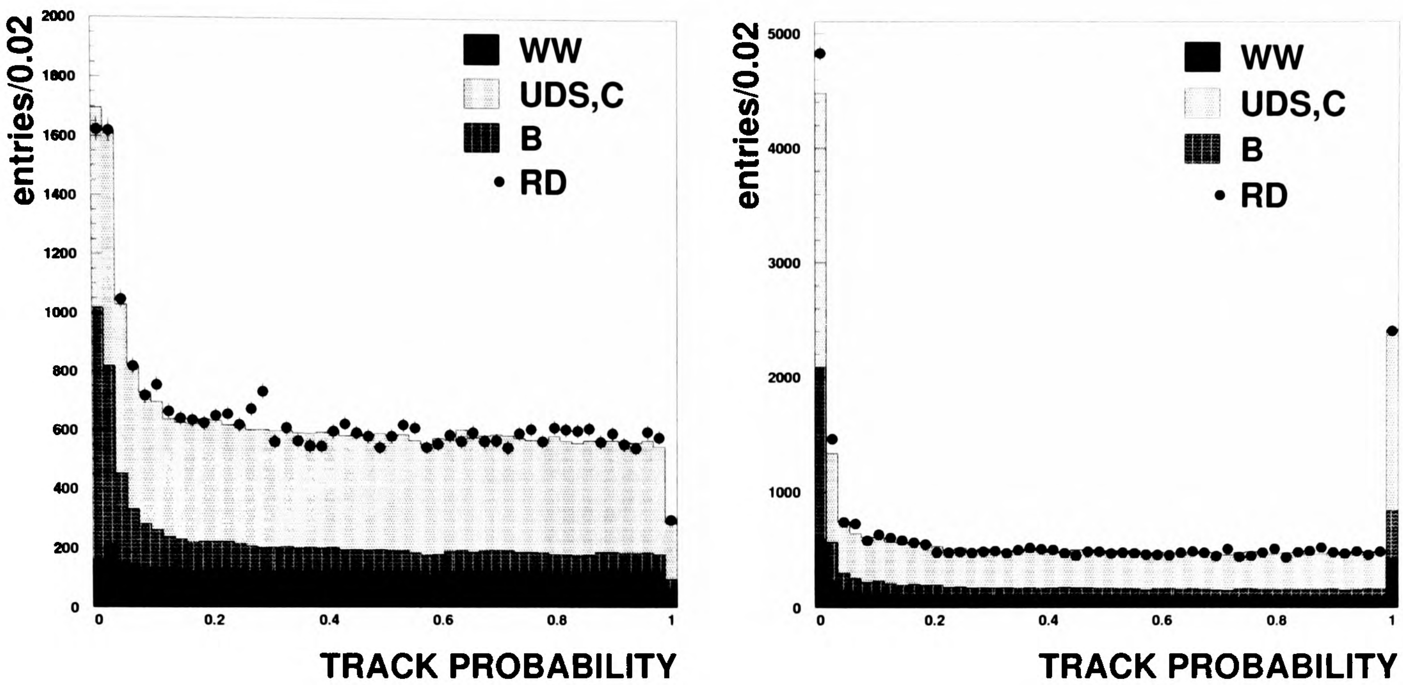

Figure 3.9: On the left hand is the track probability distribution for rϕ plane. On the right hand side is the track probability distribution for the rz plane. These distributions are for the 2000 data.

If the fit does not pass certain convergence criteria, the track making the largest χ^2 contribution is ignored and the fit is repeated in an iterative procedure.

The distribution of the number of SV produced is shown in figure 3.10 for the 1998 data. As can be seen, the b events produce more SV candidates than the background classes.

3.3.3 Compound discriminating variables

The compound discriminating variables used exploit the b hadron long life time and make use of the raw variables discussed above, as well as the high mass of the b quark.

- The Jet lifetime probability (P_N^+) is constructed from positively signed track probabilities of rϕ and rz included in a jet, and corresponds to the probability that a group of tracks coming from the primary vertex is equal or larger than the observed value. It is calculated for each jet separately and defined as:

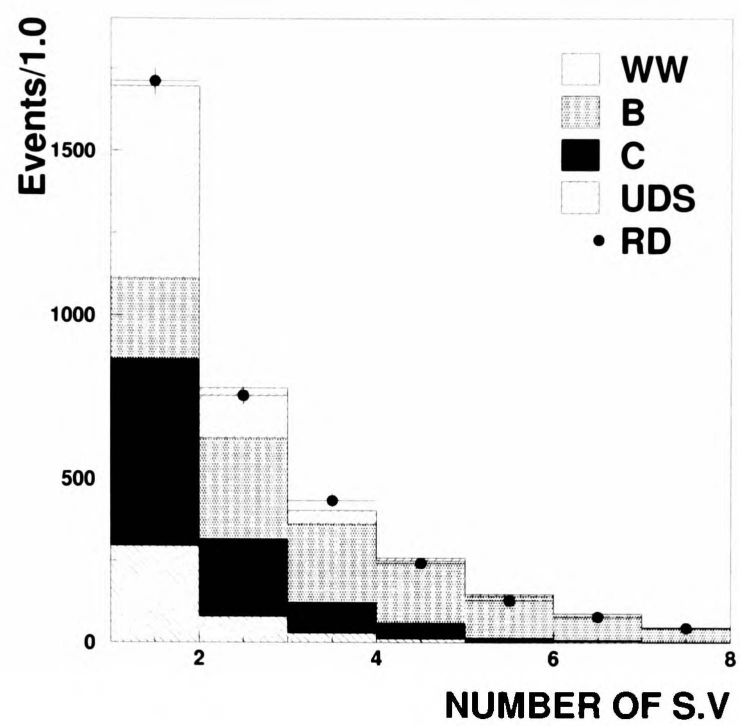

Figure 3.10: The number of found Secondary Vertices in b,c,uds and W^+W^- events for the 1998 data set.

$$P_N^+ = \prod \cdot \sum_{j=0}^{N_{r\phi}+N_z-1} (-\log \prod)^j / j! \tag{3.5}$$

where $\prod = \prod_{i=1}^{N_{r\phi}} P(S_{r\phi}^i) \cdot \prod_{i=1}^{N_z} P(S_z^i)$, $P(S_{r\phi}^i)$, $P(S_z^i)$ are the track probabilities and $N_{r\phi}$, N_z are the number of tracks used in the rϕ and z planes.

The idea behind this combination is to multiply the individual track probabilities in order to give the group probability. This is seen in the log term. Since the values of the individual track probabilities are between 0 and 1, multiplying them will yield a small number even for a group of tracks with large track probabilities(say above 0.5). Therefore it is necessary to separate the small values better. The factorial factor makes the small values even smaller and therefore by summing over the different factorial terms and eventually taking the log of P_N^+ a better separation is achieved between the smaller probabilities values and the larger ones.

For jets with a b hadron this probability is very small due to the significant impact parameters of tracks coming from the b hadron decay. Jets containing a c quark also have small values due to the non-negligible lifetime of the D meson. The distribution of $-log_{10}(P_N^+)$ for the different quark flavor is shown in figure 3.11. The b events are clearly separated from the background.

- The distribution of the effective mass in the reconstructed secondary vertex, M_s, is shown in figure 3.12. It is calculated from the invariant mass of the tracks associated to the secondary vertex. This exploits the heavier mass of the b hadron. The background from c events due to the mass of the D meson stops above 1.8 GeV.

- The track rapidity is defined as:

$$R = \frac{E + P_l}{E - P_l} \tag{3.6}$$

where E is the tracks energy and P_l is the track's momentum along the jet direction. The distribution of the track rapidity variable is shown in figure 3.13. In the case a jet contains a reconstructed secondary vertex the track rapidity is calculated with respect to the direction of the line connecting the secondary vertex and the primary vertex. In the case there is no secondary vertex the rapidity is calculated with respect to the jet direction. The c and b events get the highest values in figure 3.13. This is due to their hadronisation properties and the high b and c hadron multiplicities.

3.3.4 Tagging Technique

The above discriminating variables are combined together in a single event b tag variable. The optimal combination means that the resulting variable gives the best possible background suppression for a given efficiency of signal selection. Consider a single discriminating variable x which has a different distribution for signal and

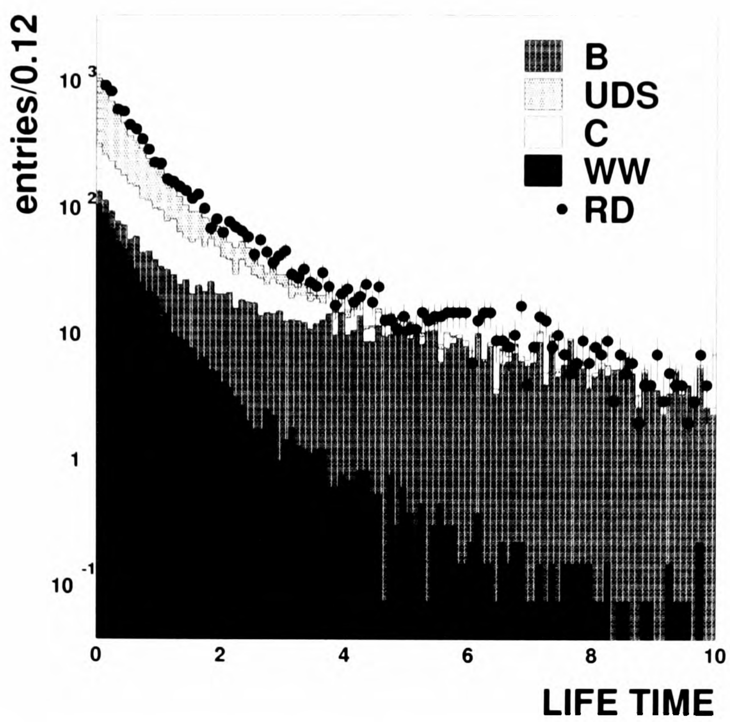

Figure 3.11: The distribution of the jet lifetime variable for 2000 data.

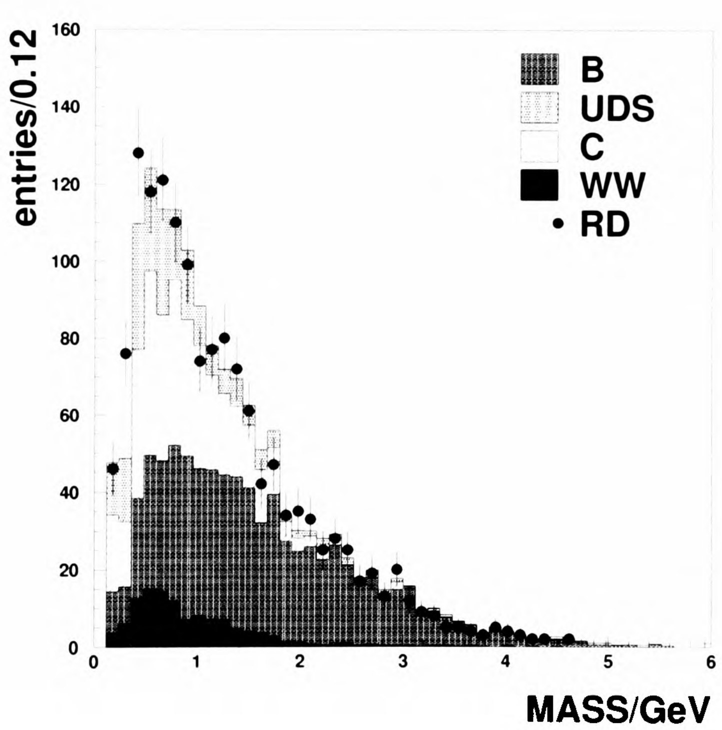

Figure 3.12: The distribution of the mass variable for 2000 data. This variable is available only in events where a SV was reconstructed.

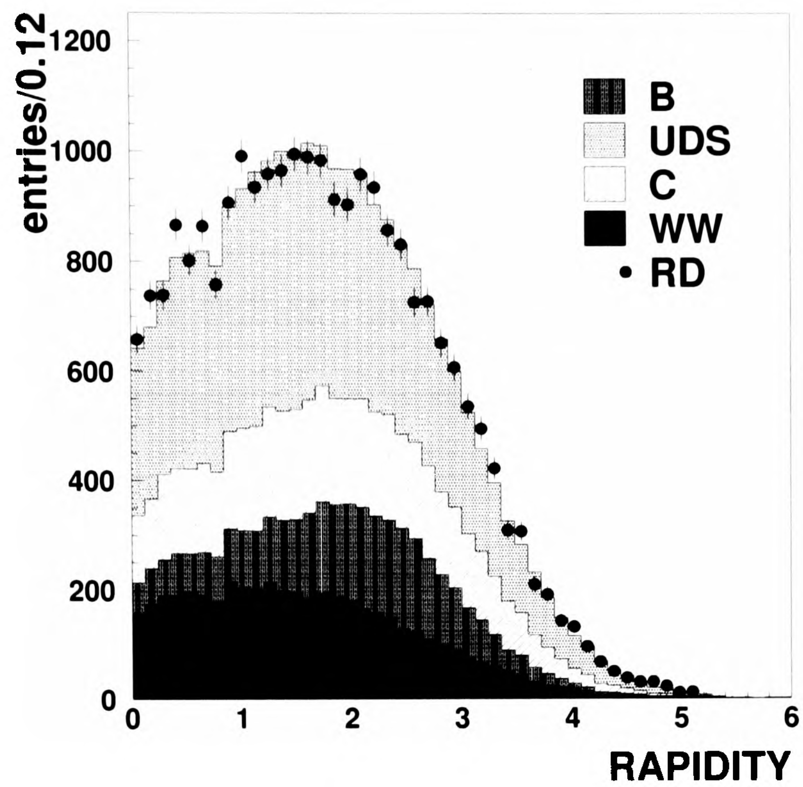

Figure 3.13: The distribution of the track rapidity for the 2000 data.

background events. Let the probability density function for the signal be $F^s_{(x)}$ and for background be $F^b_{(x)}$. If we suppose that the ratio $y = F^b_{(x)}/F^s_{(x)}$ is a monotonically decreasing function for increasing x, we can select events by making a cut $x > x_2$. We can extend to the general case where we have a number of discriminating variables $x_1........x_n$:

$$y = \frac{F^b_{(x_1....x_n)}}{F^s_{(x_1.....x_n)}} \tag{3.7}$$

where $F^b_{(x_1....x_n)}$ and $F^s_{(x_1....x_n)}$ are the multi dimensional probability density functions for background and signal respectively.

In the case of independent variables expression 3.7 becomes:

$$y = \prod_{i=1}^{n} \frac{F^b_{(x_i)}}{F^s_{(x_i)}}. \tag{3.8}$$

The tagging procedure defined can include any number of discriminating variables. The jet rapidity variable which is initially available for each track in the jet is obtained by applying equation (3.8) on the individual tracks in the jet and then combine with the other jet variables. In practice the variables are not independent and definition (3.7) should be used. Although this gives the optimal tagging it is difficult to define for large n. Consequently the discriminating variables are chosen which have minimal correlation, and are combined as explained above supposing they are independent. This is not absolutely optimal because of the residual correlations but is a good practical solution. The resulting quantity obtained from the above technique is called the b tag variable.

3.3.5 Performance

The distribution of the combined b tag made from the above variables is shown in figures 3.14 - 3.18 for all the data sets analyzed. The b events are clearly separated and there is a good data and MC agreement in all the years. The b efficiency as a function of the cosine of the polar angle of the event thrust axis is shown in figure 3.19 for events with a b tag variable > 1. The figure shows the event loss at low angles due to the poor detector performance in these angular regions. This efficiency drop motivated the cut on the thrust axis, $\cos_t < 0.9$. The 'efficiency-purity' curve, as determined from 2000 MC at a mean centre-of-mass energy of 205 GeV, is shown in figure 3.20 for $q\bar{q}$ events. One can see that for a b efficiency of 60% the purity is 95%. The b tag performance degrades with centre-of-mass energy. For example in the 1997 data set at a mean centre-of-mass energy of 183 GeV, for a purity of 95% the efficiency is 68%. This degradation effect will be discussed further in section

3.3.6. The b tag working point for the analysis presented in this thesis is a b tag cut of 1. This choice will be justified in chapter 4. The number of data and MC events passing this b tag cut for each of the data sets used is shown in table 3.1.

3.3.6 Efficiency measurement from the Z^0 data

The b efficiency for high energy as taken from the MC can be directly compared with a measurement made from the data at Z^0 energies. The very precise measurement of R_b, defined as the fraction of b events out of the total $q\bar{q}$ cross section, made at LEP1 ($R_b = 0.2167 \pm 0.0007$[28]) allows equivalent measurements made with data collected in LEP2 Z^0 calibration runs to be inverted and the b efficiency calculated directly from the data. The resulting value can be used as a correction to the MC efficiency value used at high energy. The b efficiency(e_b) is given by:

$$e_b = \frac{R_{tg} - E_c(R_c/r_{c(BIAS)}) - E_{uds}(1 - (R_b/r_{b(BIAS)}) - (R_c/r_{c(BIAS)}))}{R_b/r_{b(BIAS)}} \qquad (3.9)$$

where R_{tg} is the ratio of b tagged events to the total hadronic sample, E_c and E_{uds} are the c and uds efficiencies, R_c and R_b are the c and b ratios from the unbiased hadronic sample and $r_{c(BIAS)}$ and $r_{b(BIAS)}$ are small corrections due to the effect of the hadronic cuts. They are calculated using $r_{b,c(BIAS)} = \frac{R'_{b,c}}{R_{b,c}}$ where $R'_{b,c}$ is the b(c) ratio after the hadronic cuts and are obtained from MC. This is done in order to eliminate any bias caused by these cuts on the number of b events. This is expected to decrease the R_b value after the hadronic cuts. In this measurement the anti W^+W^- cuts are removed from the event selection procedure described at the beginning of this chapter as they are not relevant for the Z^0 energy . Table 3.3 shows the measured and MC b efficiency and purity for the different years of data taking. There is reasonable agreement between the data and MC values. One can see that while the purity remains fairly constant, the efficiency drops from 0.64 to 0.52 from

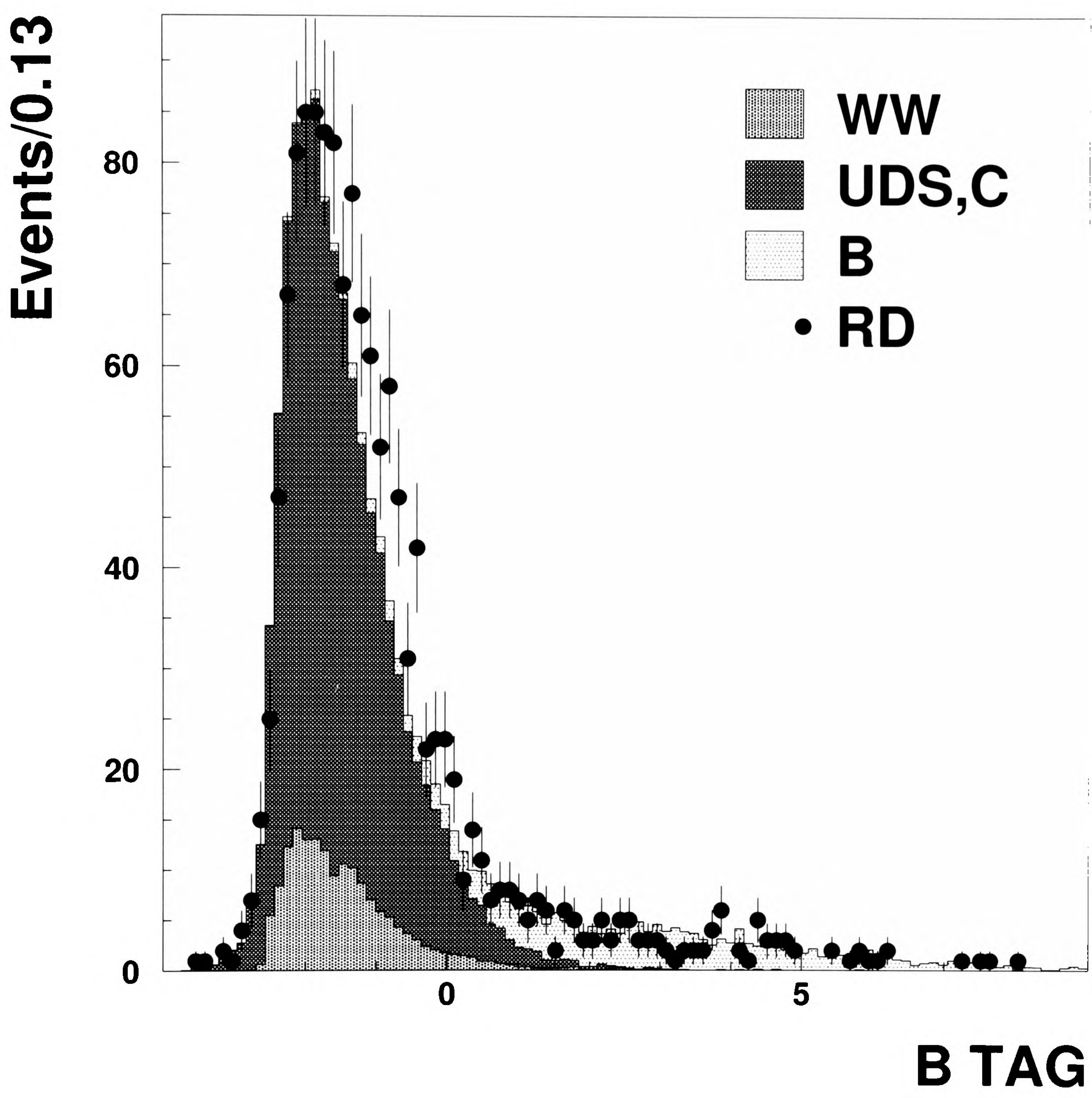

Figure 3.14: The distribution of the b tag variable per event for signal and background for the 1997 data set.

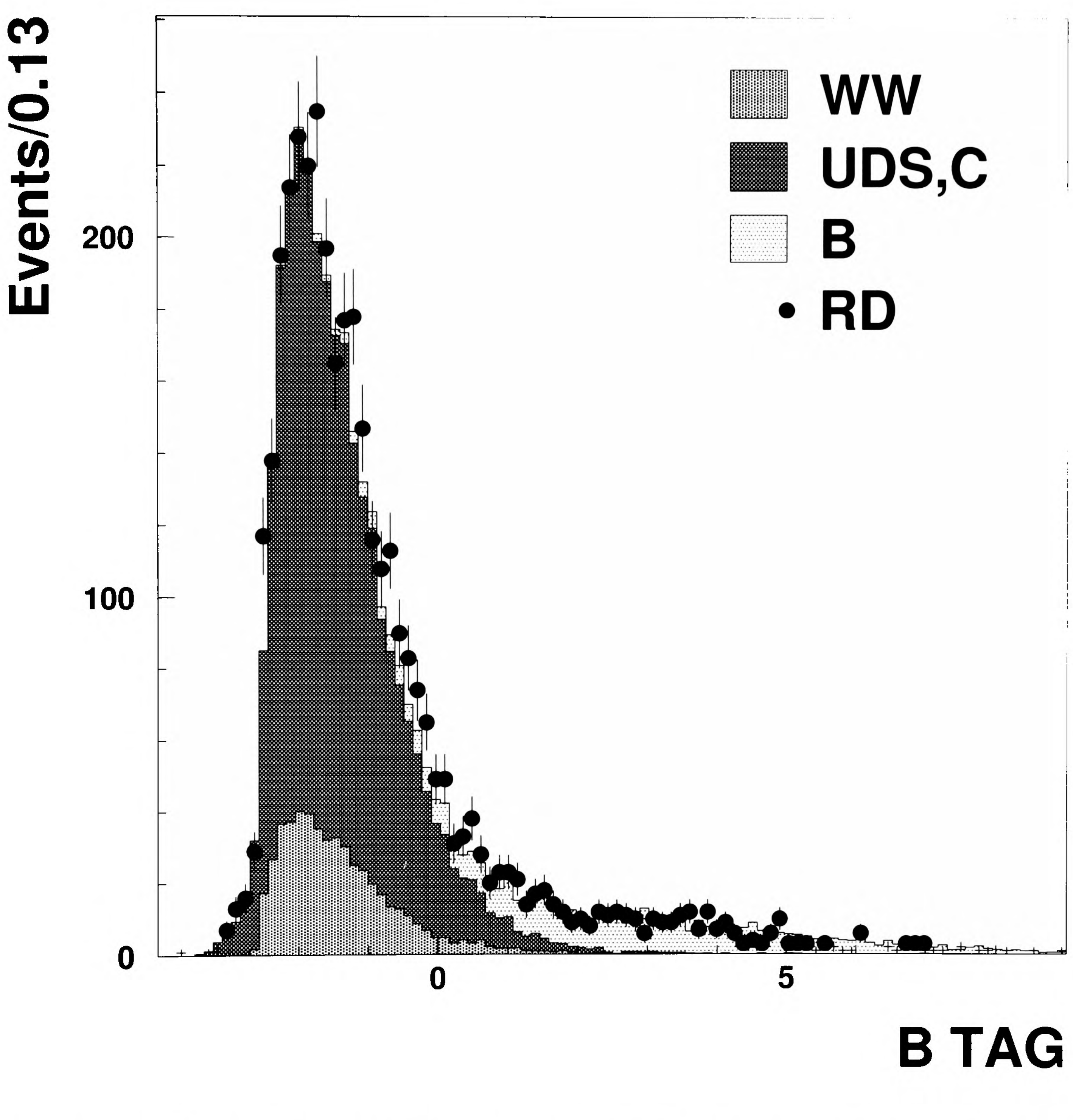

Figure 3.15: The distribution of the b tag variable per event for signal and background for the 1998 data set.

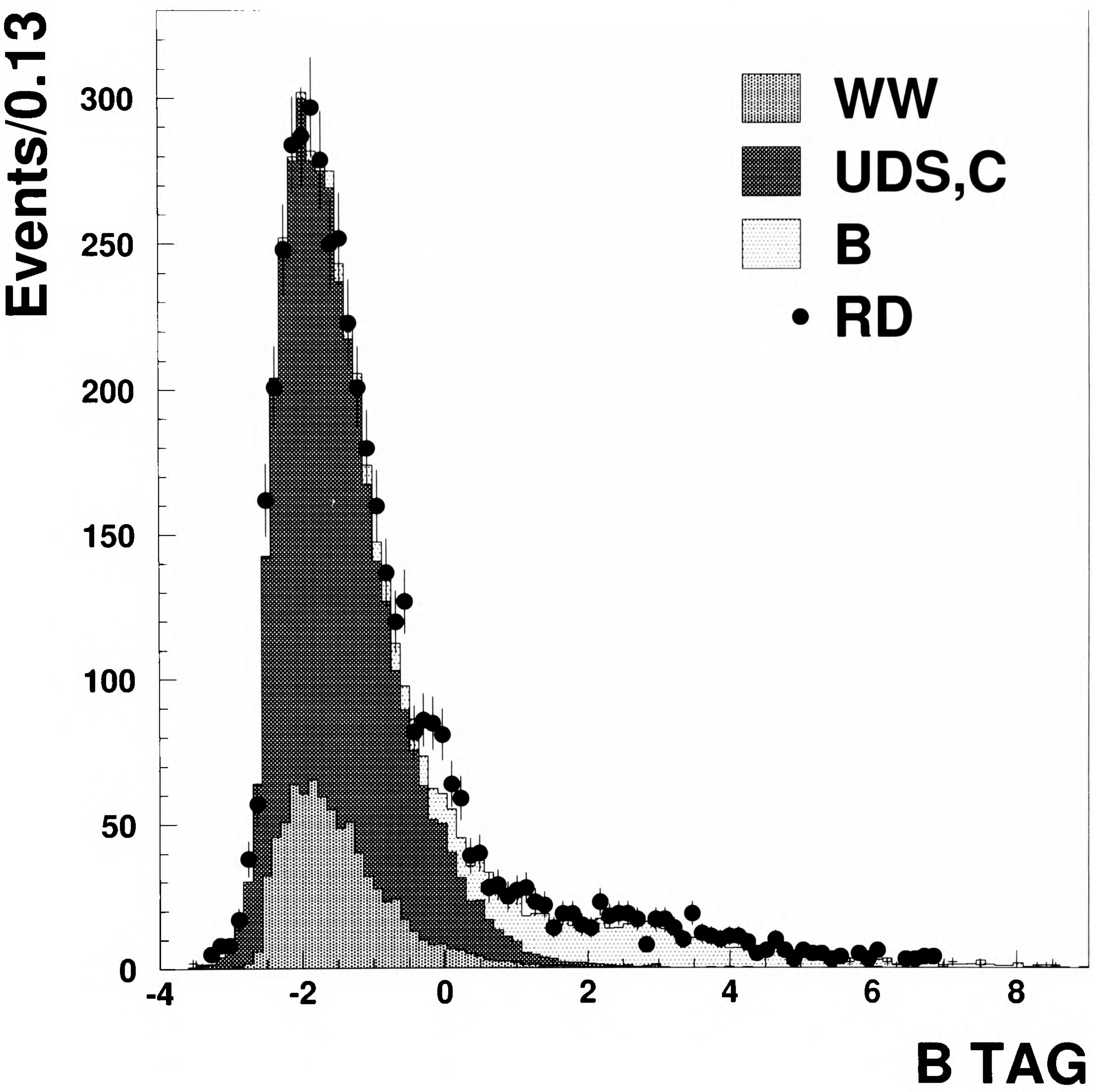

Figure 3.16: The distribution of the b tag variable per event for signal and background for the 1999 data set.

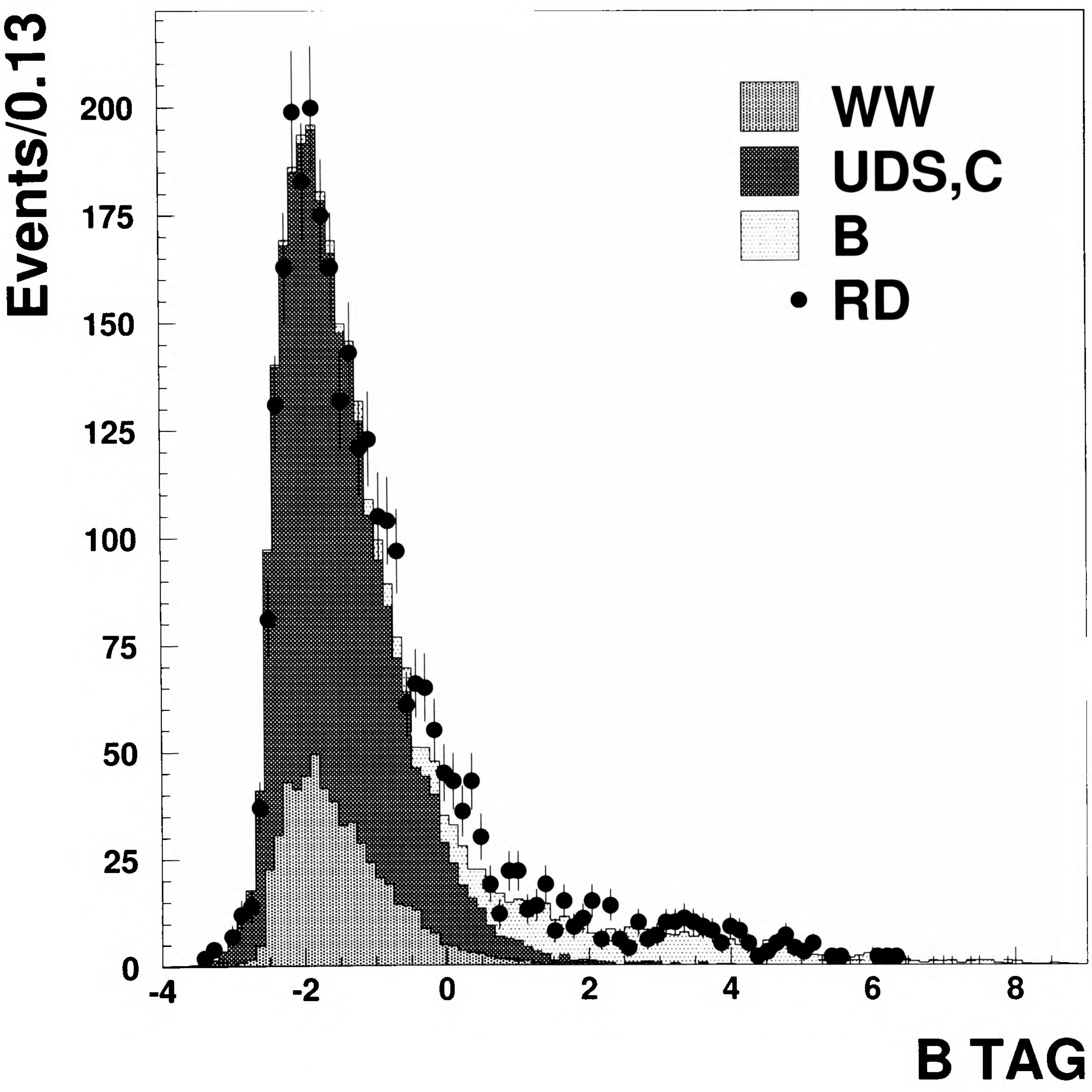

Figure 3.17: The distribution of the b tag variable per event for signal and background for the 2000 good TPC data set.

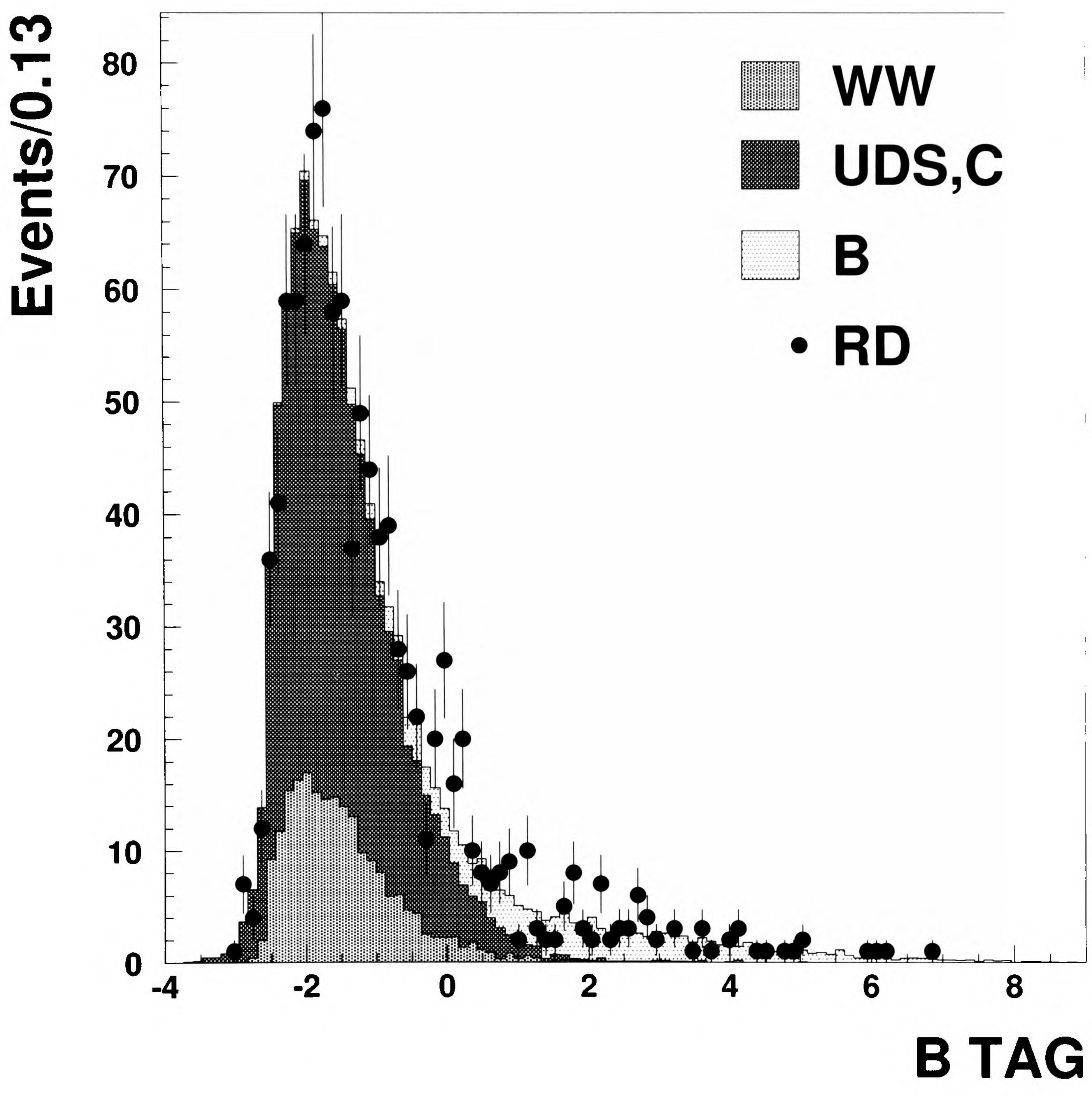

Figure 3.18: The distribution of the b tag variable per event for signal and background for the 2000 bad TPC data set.

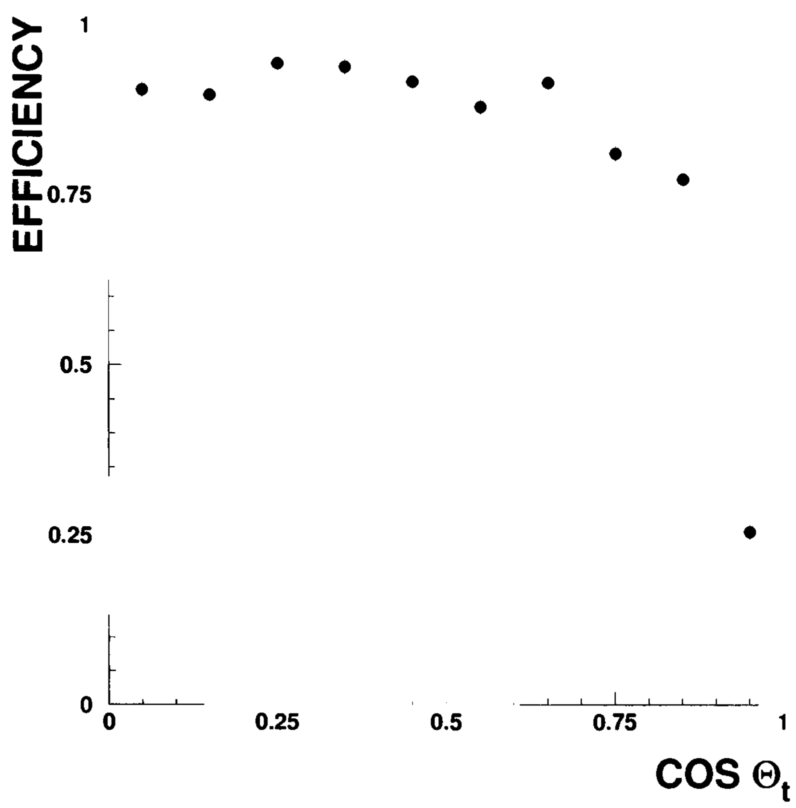

Figure 3.19: The b efficiency as a function of the cosine of the event thrust axis for 1998 MC.

1997 to 2000 data. This is not well understood but may be related to silicon aging. The correction factor used for the high energy efficiency is calculated from the ratio of the real data and MC efficiencies on the Z^0. One can see that this ratio vary from year to year. This was noted but not studied further as the final corrections to the measurement from these efficiency corrections are small(discusses in chapter 4). The idea behind this efficiency correction is that by definition we trust a good data measurement more than MC and therefore if we can correct the MC from the data we should do do. Since we generally trust the MC to describe the data equally well for Z^0 energy and high energy, a correction made on the Z^0 is applicable to High energy.

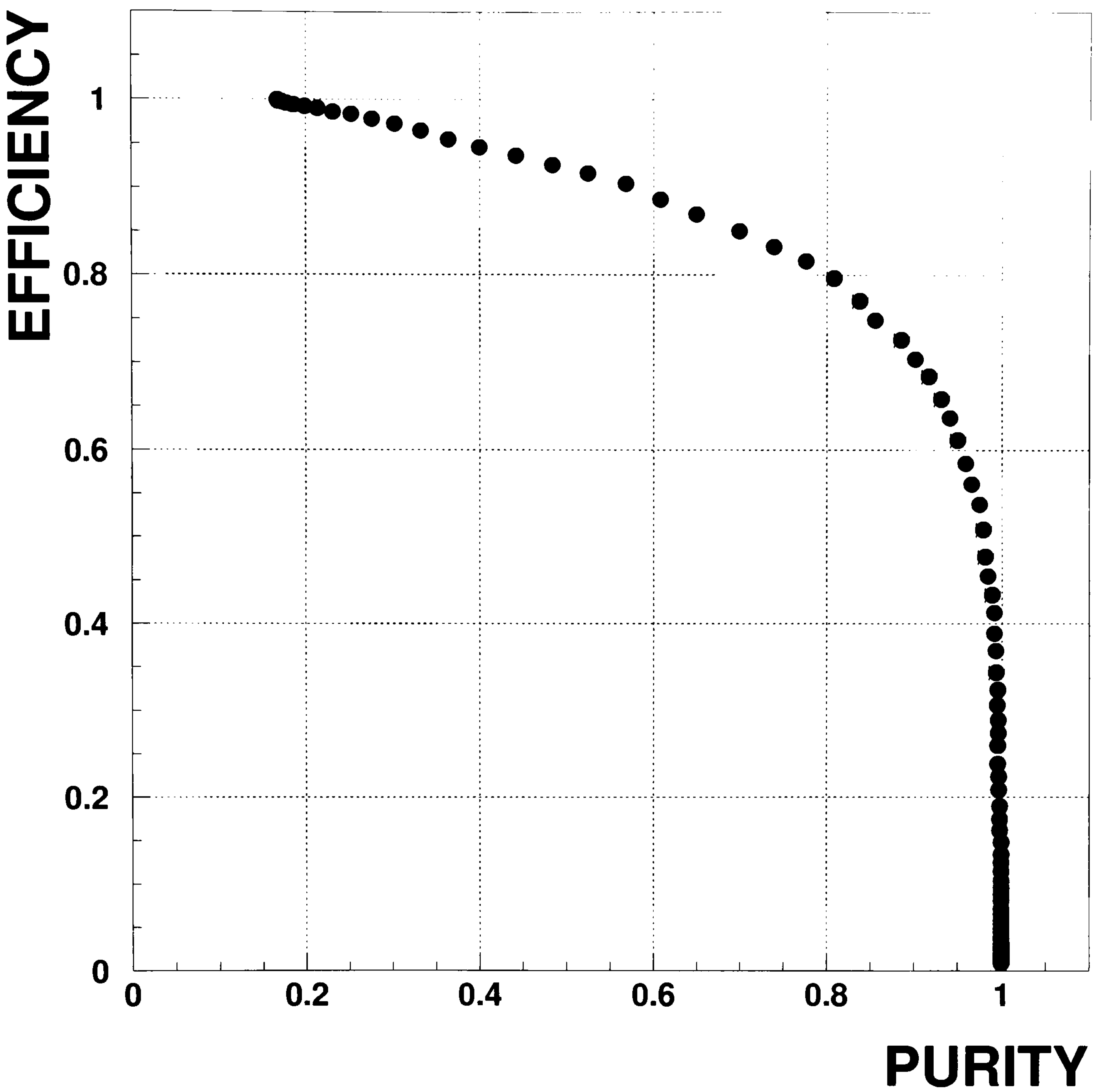

Figure 3.20: The b efficiency versus purity curve for $q\bar{q}$ events in the 2000 MC.

	number of events	Efficiency in RD	Efficiency in MC	Purity in MC
1997	3239	0.607 ± 0.008	0.644 ± 0.006	0.978 ± 0.002
1998	4008	0.677 ± 0.007	0.653 ± 0.006	0.972 ± 0.003
1999	2867	0.554 ± 0.009	0.584 ± 0.005	0.983 ± 0.002
2000 (G)	4263	0.577 ± 0.007	0.526 ± 0.006	0.989 ± 0.005
2000 (B)	3500	0.578 ± 0.008	0.531 ± 0.004	0.982 ± 0.003

Table 3.3: The b efficiency in data and MC for 1997-2000 data sets as measured at the Z^0. The number of events are after the b tag cut. (G) and (B) refers to the good and bad TPC periods during 2000.

4. The A^b_{FB} measurement

4.1 Overview

This chapter describes the $b\bar{b}$ forward-backward asymmetry measurement made using an unbinned log likelihood fit. After introducing the basic method, refinements are then discussed in order to extract maximum information from the data. The procedure for arriving at the optimal working points for the analysis is presented. The components in the systematic error assignment are described at the end of the chapter.

4.2 Reconstruction of the b production angle

In order to experimentally measure the b asymmetry it is necessary to identify in each event the direction of the b quark. This introduces an experimental difficulty as in the hadronisation process, the initial b quark fragments into a jet of hadrons with no clear correspondence to the initial quark charge.

The analysis is concerned with high $\sqrt{S}'$ production, that is events with little or no initial state radiation. In these events the expected event shape is two back to back jets. The production axis, $\hat{n}$, of the $b\bar{b}$ orientation in these events is obtained by maximizing the thrust, T defined as:

$$T = \frac{\sum_i |p_i \cdot \hat{n}|}{\sum_i |p_i|} \tag{4.1}$$

where p_i is the track's momentum, $\hat{n}$ is a unit thrust vector and the sum runs over all well measured charged tracks in the event. Figure 4.1 shows the angular distribution of the event thrust axis for the 2000 data set. This is made for the event sample

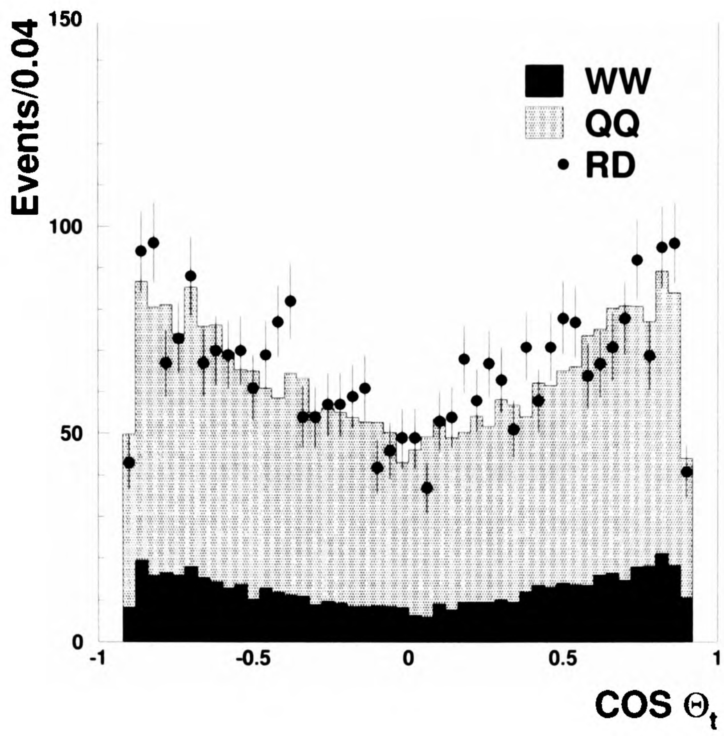

Figure 4.1: The distribution of the event thrust axis for hadronic events of 2000 data set.

that passed the set of event selection cuts described in chapter 3. This is a close approximation to the real $b\bar{b}$ production axis as is shown in figure 4.2 where the difference of the cosine of the real b production axis and the thrust axis is taken.

After obtaining the thrust axis, it is necessary to distinguish between the directions of the b and $\bar{b}$ quarks. This may be done using the jet-charge method. In the hadronisation process the b hadron gets a large fraction of the centre of mass energy compared to the other hadrons produced(about 0.8 of the energy on average as can be seen in figure 1.11). Thus in general, the energetic tracks in the event are more likely to belong to the decay of the B hadron and therefore contain more information about the charge of the quark inside the hadron. In most cases this will enable the charge of the quark at production to be deduced. In cases where the hadron is neutral and has oscillated, however, the wrong result will be inferred. This information can be used to calculate a quantity that corresponds to the b charge called a momentum weighted jet charge($Q_{F(B)}$) from the tracks in the forward(F) and backward(B) hemispheres. This variable is constructed to give more weight to the charge of tracks from the b decay.

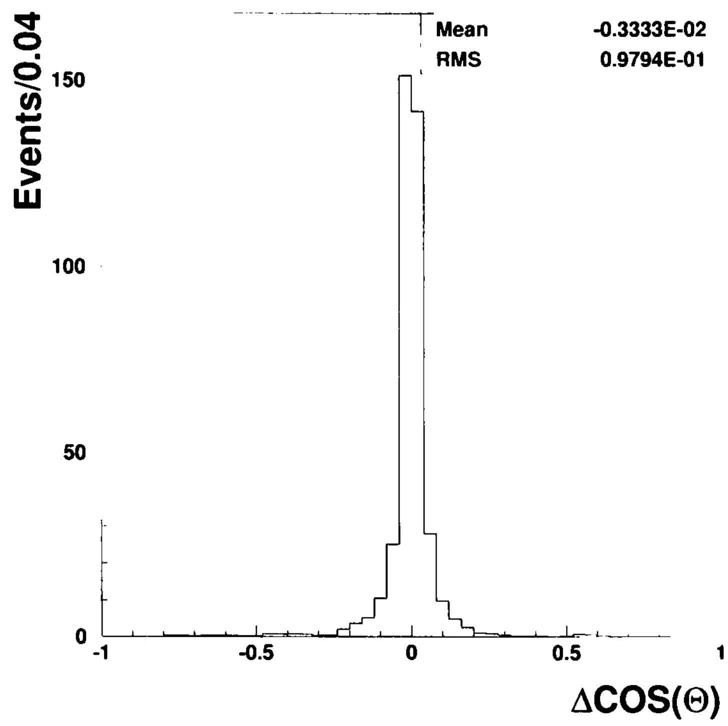

Figure 4.2: The difference of the cosine of the real $\bar{b}$ production axis and the thrust axis for the 2000 MC.

$$Q_{F(B)} = \frac{\sum_i |p_i \cdot \hat{n}|^{\kappa} q_i}{\sum_i |p_i \cdot \hat{n}|^{\kappa}} \tag{4.2}$$

where κ is an empirical parameter chosen to maximize the technique's performance, q_i is the track charge, $\hat{n}$ is the unit thrust vector in the hemisphere with the positive z axis(defined to be the forward hemisphere) and the sum runs over all well measured charged tracks in the event. The tracks contributing to the forward/backward jet charge have $p_i \cdot \hat{n} > 0$, $p_i \cdot \hat{n} < 0$ respectively.

Q_F and Q_B may be combined together into two single event variables. The first of these is $Q_F + Q_B$ which contains no information about the $q\bar{q}$ direction, but rather characterises the detector response. The second is $Q_{FB} = Q_F - Q_B$ which combines together the flavour information in both hemispheres into a single variable with maximum discrimination.

Figures 4.3-4.7 show the $Q_F + Q_B$ distributions for data and MC for all the years analyzed individually, and in figure 4.8 for all years combined. The mean of the combined $Q_F + Q_B$ distribution seen in figure 4.8 is $0.4 \pm 8.1 \cdot 10^{-3}$ which is consistent with zero. There is good agreement between data and MC in this variable for all the distributions indicating that the detector resolution on the jet charge is resonably well described.

Figures 4.3-4.7 also show the data and MC distribution of Q_{FB}. The distributions are generally biased towards negative values, indicating that the b is produced more often in the forward hemisphere. This is a direct evidence of a finite value of the b asymmetry(A^b_{FB}). The mean value of the combined Q_{FB} distribution for all years is -0.0614 ± 0.0089.

Because the jet charge algorithm does not always select the tracks from the primary quark's decay, and because of $B^0_{d,s}$ oscillations, the sign of Q_{FB} does not always correctly indicate the b quark direction. The b direction is correctly assigned in 68% of the cases according to the MC averaged over all years.

It is important to check the data and MC agreement in two key variables that affect the jet charge: The event charged track multiplicity, which is shown in figure 4.9, and the track momentum shown in figure 4.10. There is a reasonable agreement in the most important regions of both distributions. The areas of discrepancy are considered in the systematic error assignment.

The Q_{FB} information can be combined with the obtained thrust axis for each event by defining the variable $\cos^{rec}_b$:

$$\cos^{rec}_b = S \cdot |\cos\theta_t| \tag{4.3}$$

where $S = +1$ if $Q_{FB} < 0$. This gives the reconstructed angular distribution of the b quark. Figure 4.11 shows the $\cos^{rec}_b$ variable distribution for the 1999 data. The distribution shows a clear asymmetry in the reconstructed angular distribution of the b quark. It is also seen that there are less data in the region $\cos^{rec}_b = \pm 1$. This is due to the detector inefficiency at these angles.

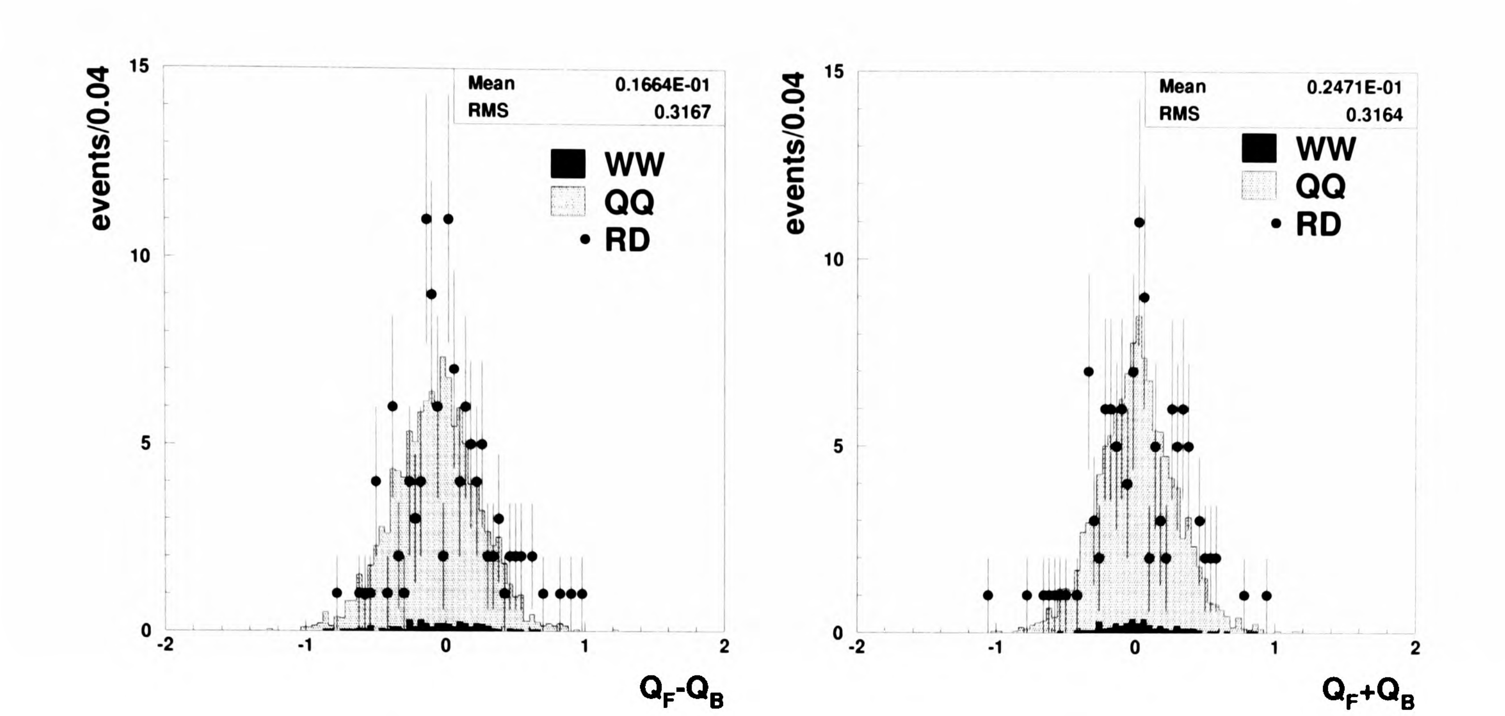

Figure 4.3: 1997 jet charge distributions. Left:Distribution of $Q_F - Q_B$. Right: Distribution of $Q_F + Q_B$.

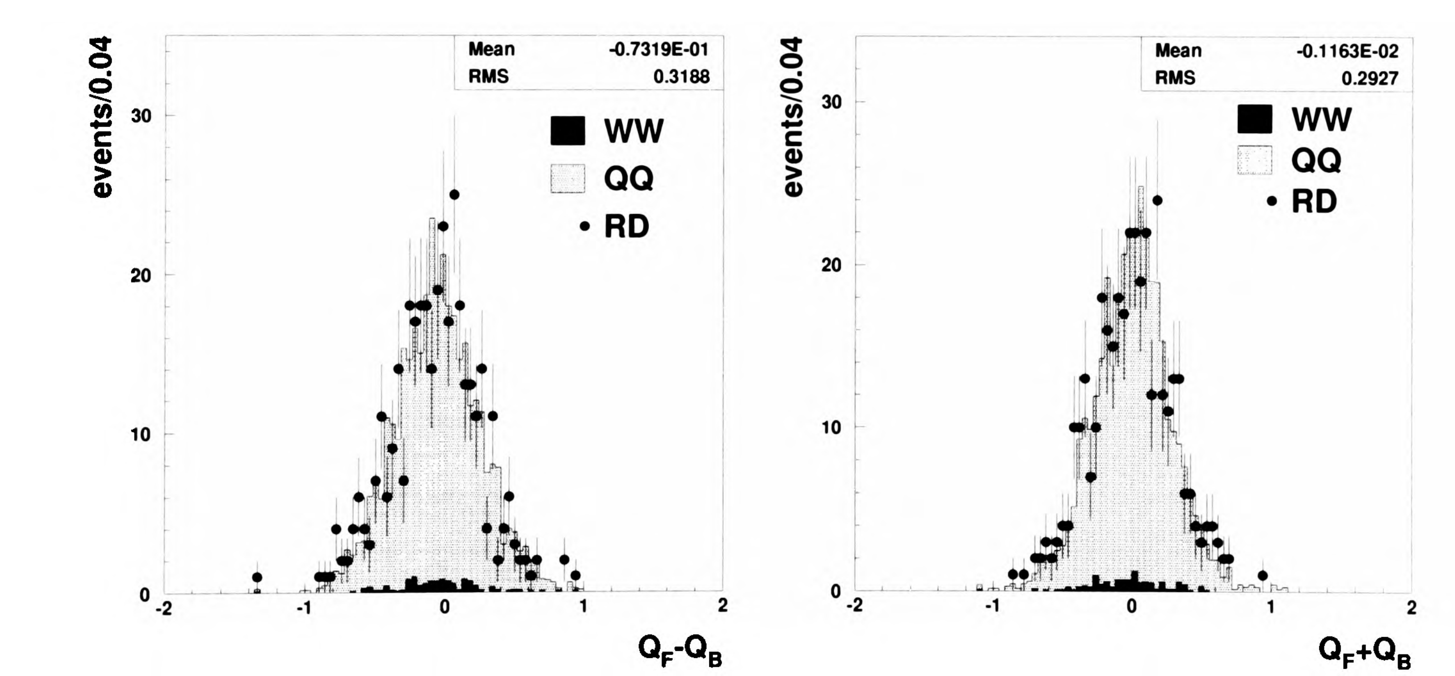

Figure 4.4: 1998 jet charge distributions. Left:Distribution of $Q_F - Q_B$. Right: Distribution of $Q_F + Q_B$.

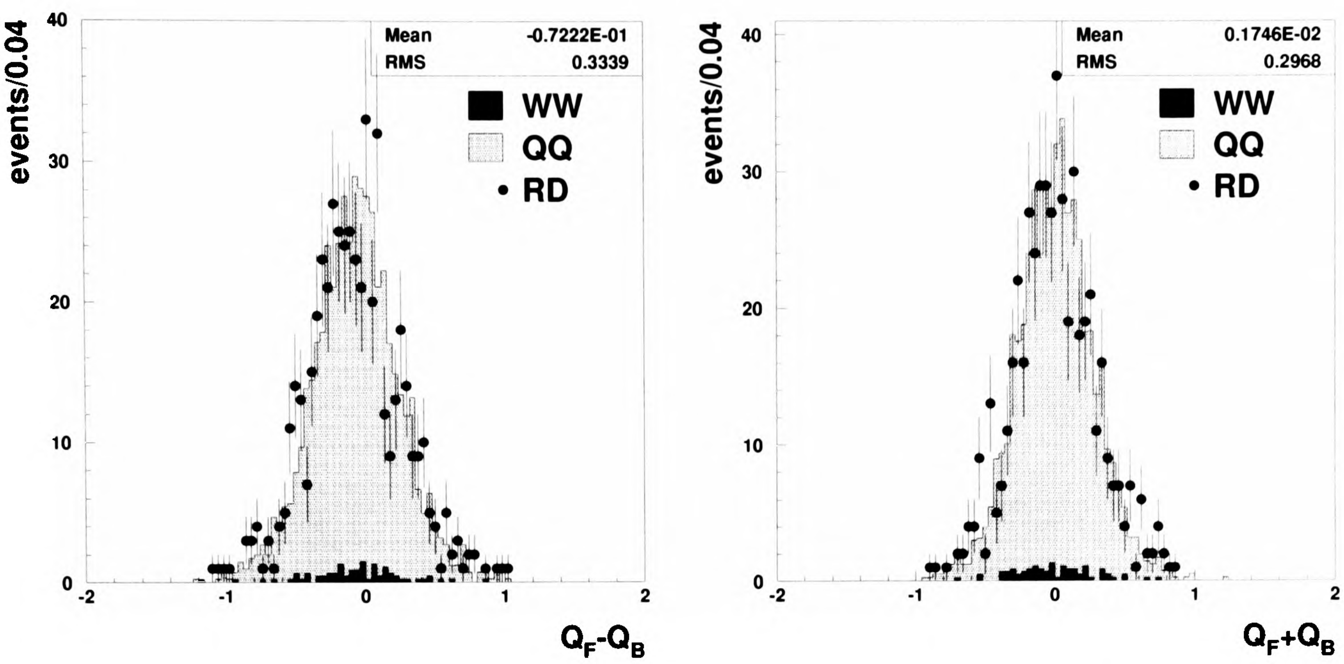

Figure 4.5: 1999 jet charge distributions. Left:Distribution of $Q_F - Q_B$. Right: Distribution of $Q_F + Q_B$.

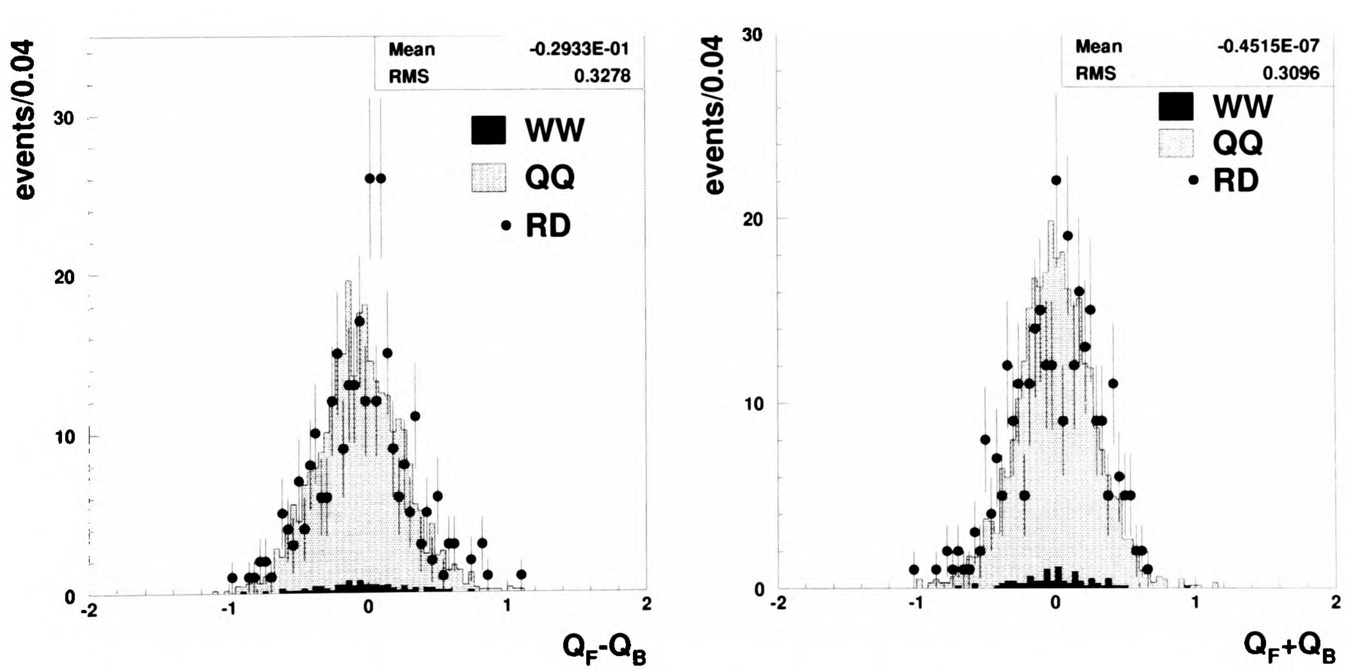

Figure 4.6: 2000 TPC good jet charge distributions. Left:Distribution of $Q_F - Q_B$. Right: Distribution of $Q_F + Q_B$.

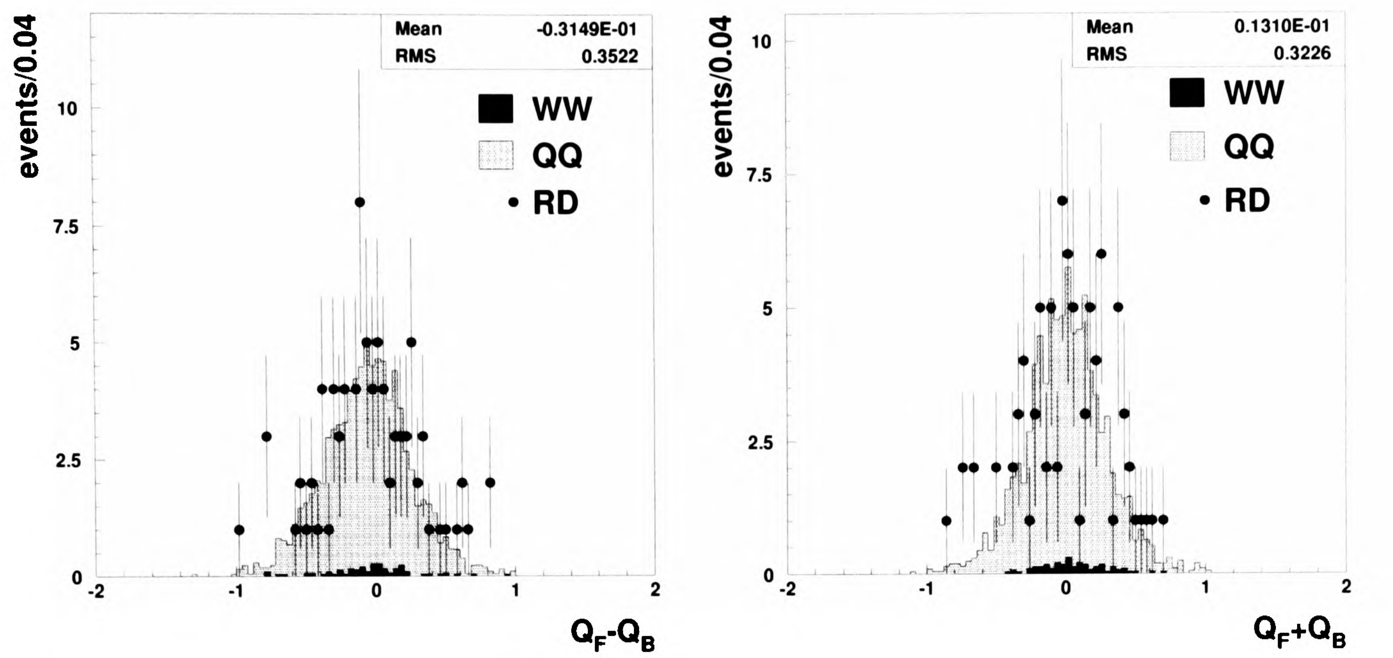

Figure 4.7: 2000 TPC bad jet charge distributions. Left:Distribution of $Q_F - Q_B$. Right: Distribution of $Q_F + Q_B$.

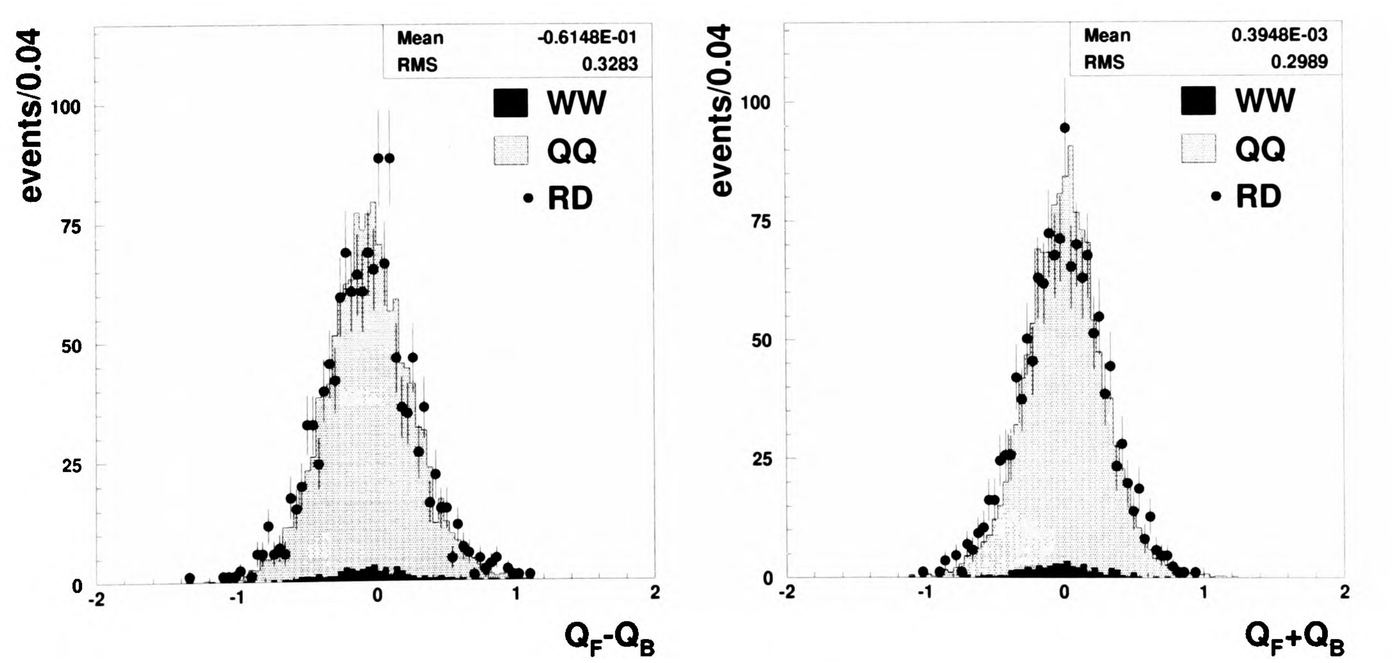

Figure 4.8: All data jet charge distributions. Left:Distribution of $Q_F - Q_B$. Right: Distribution of $Q_F + Q_B$.

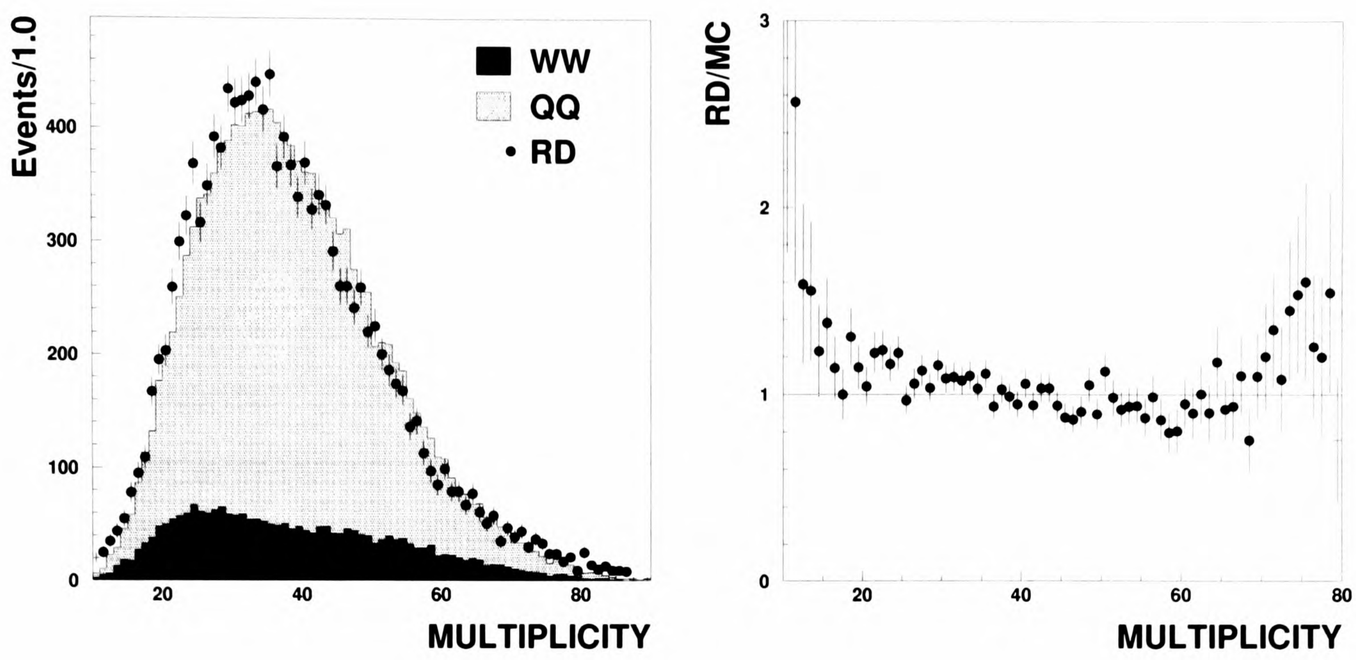

Figure 4.9: Left: event charged track multiplicity for all data sets combined. Right: ratio of data and MC for charged tracks multiplicity.

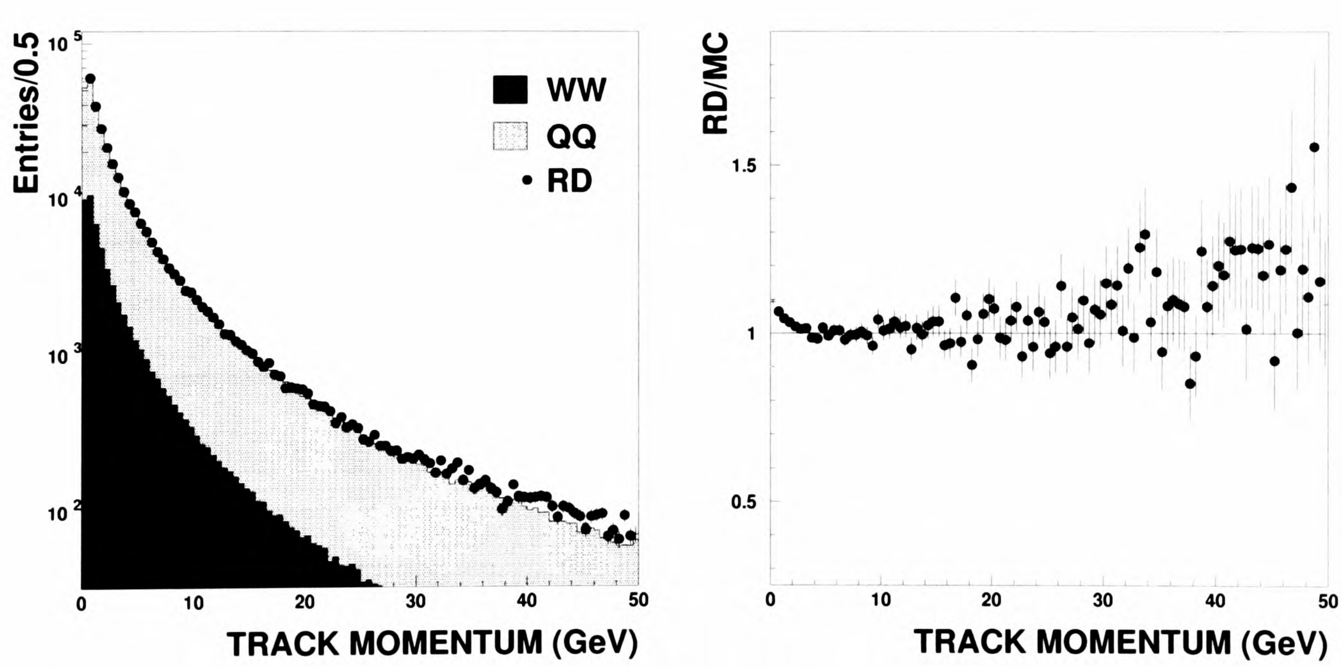

Figure 4.10: Left: track momentum for all data sets combined. Right: ratio of data and MC in this variable.

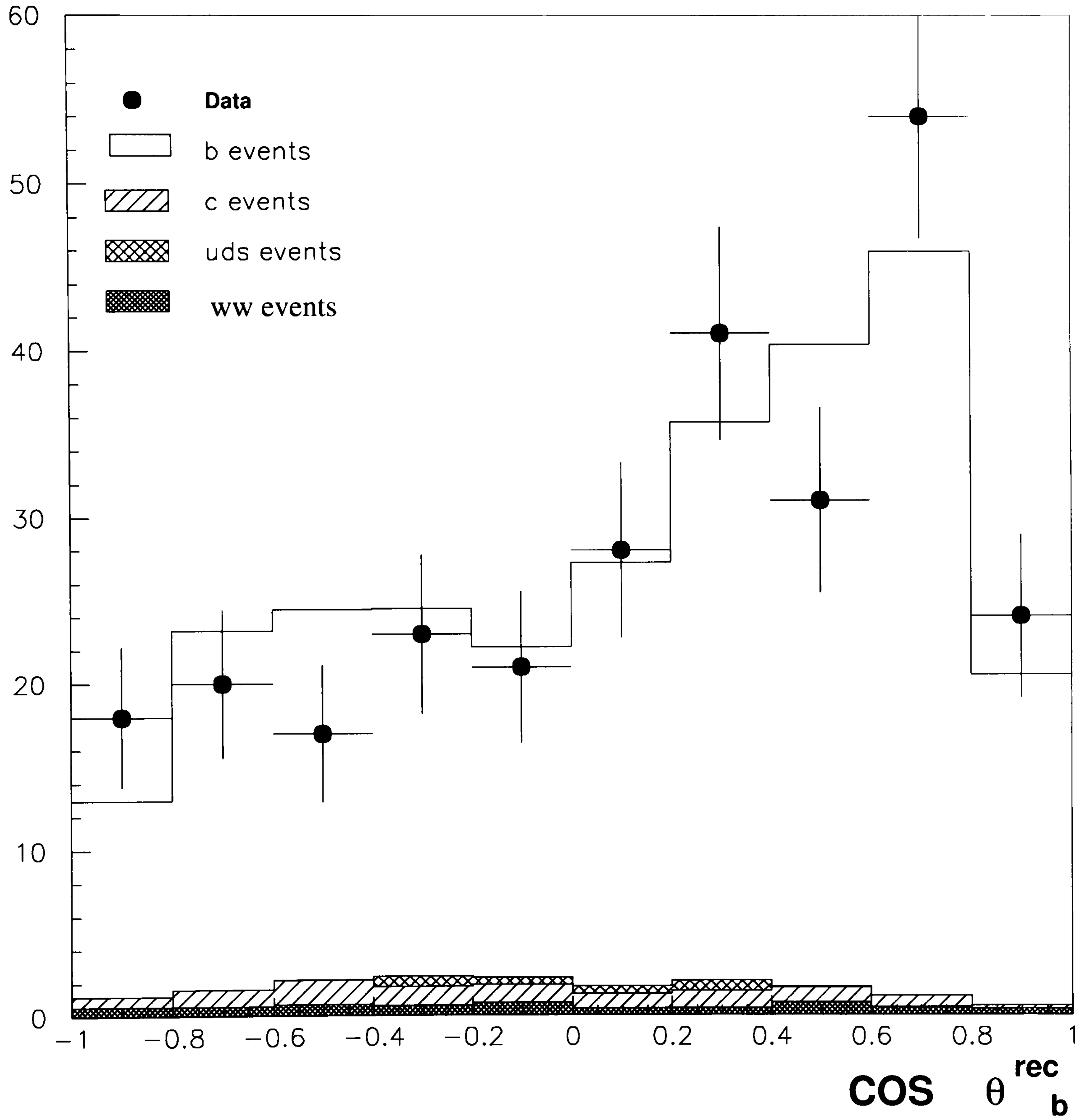

Figure 4.11: Distribution of the $\cos_b^{rec}$ variable: the cosine of the reconstructed b production angle for 1999 data.

4.3 Overview of the A^b_{FB} Measurement

The asymmetry is extracted from the $\cos^{rec}_b$ variable distribution using an unbinned log likelihood fit which maximizes, $\ln L$, the logarithm of the probability function:

$$\ln L = \sum_i \ln(1.0 + X_i^2 + \frac{8}{3} A^{mes}_{FB} X_i) \tag{4.4}$$

where $X = \cos^{rec}_b$ and i runs over all events. Note that it is not necessary to normalize the probability function as the normalization constant enters only as a constant in the fit. not affect the extracted asymmetry value.

The b dilution is defined as $D_b = 2 \cdot P_b - 1$, where P is the charge assignment purity from the jet charge. The value of D_b depends on the performance of the jet charge tagging variable which include detector resolution effects.

A^{mes}_{FB} includes the asymmetries from the background contaminations. The contributions from other quarks(uds,c) and w^+w^- background are accounted for using:

$$A^{mes}_{FB} = \sum_{q=uds,b,c,w^+w^-} D_q A^q_{FB(S\prime)} F_q \tag{4.5}$$

where F_q are the relative quark abundances ,$A^q_{FB(S\prime)}$ are the true quark asymmetries after the $S\prime$ cut and D_q the dilution factors for each quark flavour.

All the information about other flavours than the b are obtained from the MC. Table 4.1 shows the b dilution and the MC value of $AD^q_{FB} = D_q \cdot A^q_{FB(S\prime)}$ of the backgrounds applied in the correction procedure for all the data analyzed.

Table 4.2 summarizes the MC b efficiency and fractions F_q of b and the background events for all the data analyzed. One can see that for a fixed purity the efficiency drops from 0.71 to 0.63. This result is consistent with the Z^0 result shown in section 3.3.6.

The contamination from radiative events which survived the selection are accounted for in the fit. Due to imperfections in the $S\prime$ reconstruction some events with $\sqrt{S\prime} < 0.85\sqrt{S}$ survive the event selection. As these events are expected to have a different asymmetry than the non-radiative events a correction is required. This is introduced as follows:

$$A^b_{FB(S\prime)} = A^{low}_{FB} * F_{low} + A^b_{FB} * (1 - F_{low}) \qquad (4.6)$$

In this correction the fraction of low $\sqrt{S\prime}$ contamination is F_{low} and its expected asymmetry is A^{low}_{FB}. From the above expression we extract A^b_{FB}, where the rest of the values are taken from the simulation.

4.3.1 b purity correction

In the A^b_{FB} measurement the different signal and background purity values are needed to correct the measurement. In section 3.3.6 it was explained how Z^0 data and knowledge of R_b are used to correct the MC estimation of the b efficiency. This correction must now be propagated to the b purity to get the best possible estimation of F_b. The corrected purity is given by:

$$P_{COR} = \frac{(e_b + \Delta e_b)N}{[e_b + \Delta e_b]N + B} \qquad (4.7)$$

where N is the number of signal events prior to b tag, B is the number of background events after b tag, e_b is the MC efficiency for signal and Δe_b is the change in efficiency considered. This correction is made in each data set according to the Z^0 data taken in that year as shown in table 4.3.

4.3.2 Improving A^b_{FB} through Q_{FB} binning

The charge assignment purity, defined as the fraction of times the b direction is correctly identified according to the MC, varies with the value of Q_{FB}. As shown in figure 4.12 according to the MC the charge assignment is more likely to be correct for larger $|Q_{FB}|$ values. This dependence can be included in the fit in order improve the sensitivity to A^b_{FB}.

1997 data				
	b Dilution	AD^c_{FB}	AD^{uds}_{FB}	AD^{WW}_{FB}
$0.000 < \lvert Q_{FB}\rvert < 0.091$	0.081	-0.157	-0.028	0.054
$0.091 < \lvert Q_{FB}\rvert < 0.200$	0.252	-0.120	-0.008	0.113
$0.200 < \lvert Q_{FB}\rvert < 0.363$	0.421	-0.284	0.065	0.001
$0.363 < \lvert Q_{FB}\rvert < 2.000$	0.624	-0.354	-0.063	0.296
$0.000 < \lvert Q_{FB}\rvert < 2.000$	0.364 ± 0.016	-0.229	-0.035	0.116
1998 data				
	b Dilution	AD^c_{FB}	AD^{uds}_{FB}	AD^{WW}_{FB}
$0.000 < \lvert Q_{FB}\rvert < 0.095$	0.024	-0.054	0.046	0.129
$0.095 < \lvert Q_{FB}\rvert < 0.201$	0.257	-0.208	0.035	-0.004
$0.201 < \lvert Q_{FB}\rvert < 0.359$	0.361	-0.295	-0.012	0.458
$0.359 < \lvert Q_{FB}\rvert < 2.000$	0.583	-0.425	-0.116	0.319
$0.000 < \lvert Q_{FB}\rvert < 2.000$	0.339 ± 0.017	-0.245	-0.005	0.225
1999 data				
	b Dilution	AD^c_{FB}	AD^{uds}_{FB}	AD^{WW}_{FB}
$0.000 < \lvert Q_{FB}\rvert < 0.090$	0.114	-0.127	-0.132	0.134
$0.090 < \lvert Q_{FB}\rvert < 0.201$	0.284	-0.196	-0.217	0.160
$0.201 < \lvert Q_{FB}\rvert < 0.345$	0.405	-0.186	0.239	0.269
$0.345 < \lvert Q_{FB}\rvert < 2.000$	0.642	-0.303	-0.328	0.395
$0.000 < \lvert Q_{FB}\rvert < 2.000$	0.373 ± 0.018	-0.203	-0.109	0.240
2000 good TPC data				
	b Dilution	AD^c_{FB}	AD^{uds}_{FB}	AD^{WW}_{FB}
$0.000 < \lvert Q_{FB}\rvert < 0.104$	0.106	-0.120	-0.001	0.141
$0.104 < \lvert Q_{FB}\rvert < 0.204$	0.257	-0.092	0.040	0.265
$0.204 < \lvert Q_{FB}\rvert < 0.342$	0.381	-0.174	-0.019	0.312
$0.342 < \lvert Q_{FB}\rvert < 2.000$	0.631	-0.398	-0.084	0.455
$0.000 < \lvert Q_{FB}\rvert < 2.000$	0.381 ± 0.018	-0.195	-0.016	0.292
2000 bad TPC data				
	b Dilution	AD^c_{FB}	AD^{uds}_{FB}	AD^{WW}_{FB}
$0.000 < \lvert Q_{FB}\rvert < 0.082$	0.080	0.018	0.081	-0.044
$0.082 < \lvert Q_{FB}\rvert < 0.196$	0.290	-0.115	-0.019	-0.068
$0.196 < \lvert Q_{FB}\rvert < 0.353$	0.418	-0.233	-0.160	-0.088
$0.353 < \lvert Q_{FB}\rvert < 2.000$	0.630	-0.412	-0.073	0.407
$0.000 < \lvert Q_{FB}\rvert < 2.000$	0.387 ± 0.018	-0.185	-0.042	0.051

Table 4.1: Measurement corrections for 1997-2000 data sets in bins of $|Q_{FB}|$ as determined from MC.

	b efficiency	b fraction	c fraction	uds fraction	W^+W^- fraction
97	0.713 ± 0.007	0.910 ± 0.004	0.051 ± 0.003	0.013 ± 0.001	0.024 ± 0.002
98	0.721 ± 0.008	0.891 ± 0.005	0.063 ± 0.003	0.014 ± 0.001	0.032 ± 0.002
99	0.647 ± 0.007	0.907 ± 0.004	0.052 ± 0.003	0.014 ± 0.001	0.025 ± 0.002
00 (G)	0.630 ± 0.007	0.906 ± 0.004	0.052 ± 0.003	0.014 ± 0.001	0.027 ± 0.002
00 (B)	0.586 ± 0.007	0.901 ± 0.005	0.045 ± 0.003	0.017 ± 0.002	0.035 ± 0.002

Table 4.2: The b efficiency and signal and background fractions for 1997-2000 data sets. 00 (G) and 00 (B) refer to the good and bad TPC periods. The fraction values are after the purity correction was made.

	purity correction%
1997	-0.5
1998	+0.4
1999	-0.4
2000 (G)	+0.6
2000 (B)	+0.7

Table 4.3: The b purity correction for 1997-2000 data sets. The sign of the purity correction indicates whether it was added or subtracted to the raw MC value. (G) and (B) refer to the good and bad TPC periods.

The first attempt to exploit this purity-$|Q_{FB}|$ dependence proceeded in the following manner. The events were divided into subsamples according to their $|Q_{FB}|$ values. The asymmetry was measured in each subsample and then corrected using the dilution applicable to that subsample, to give individual asymmetry measurements, $A^b_{FB(i)}$ and error, σ_i, in each bin of $|Q_{FB}|$. Finally the different measurements were combined in a weighted mean, thus:

$$A^b_{FB} = (\sum_i A^b_{FB(i)}/\sigma_i^2)/(\sum_i \sigma_i^{-2}) \tag{4.8}$$

In such a combination the measurement in the purest $|Q_{FB}|$ bins with the smallest dilution correction gets a larger weight in the average, and the overall error is reduced accordingly. Performing the measurement this way gave a reduction in the assigned error over the unbinned method of typically 10-20% with 6 $|Q_{FB}|$ bins. In order to check the validity of this error reduction we used the following procedure. We

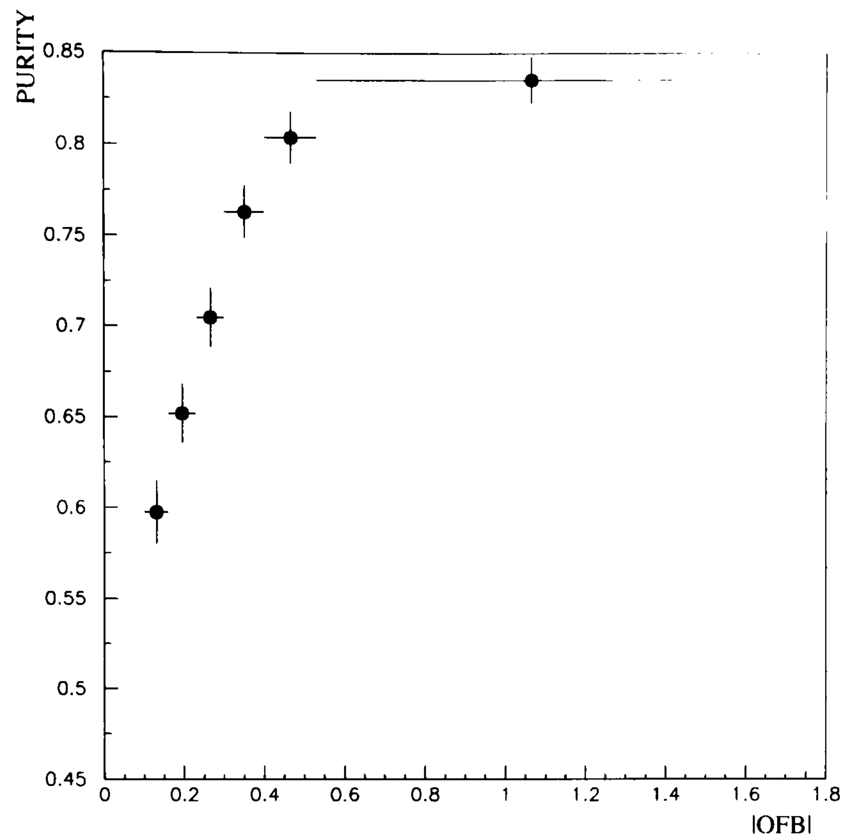

Figure 4.12: The variation of the b charge assigning purity with $|Q_{FB}|$ values as determined from the MC

selected a random sample of events similar in size to the real data sample from a large MC sample a large number of times and performed the asymmetry measurement on these samples. We used the pull value to check the accuracy of the error assigned in the fit. The pull is defined as:

$$PULL = \frac{A^b_{FB} - A^{true}_{FB}}{\sigma_{mes}}$$

where σ_{mes} is the error assigned to A^b_{FB} in the fit. This check revealed a problem in the procedure. Figure 4.13 shows the distribution of the A^b_{FB} measurement and its corresponding assigned error when the sample is divided into 6 Q_{FB} bins. The corresponding pull distribution is shown on the left in figure 4.15. The problem in the measurement is best observed in the pull distribution which has a width > 1 and is significantly offset from zero. This shows that the weighted mean is biased, and the accompanying error assignment is incorrect.

Investigation revealed that the problem was in the minimization program used to extract the asymmetry in small samples. Due to fluctuations in the small samples in the MC data sets, the asymmetry coming from the fit in certain bins can be large, which after correcting for the dilution, gives an unphysical value above 1. When the bins are combined these values distort the mean and bias the measurement.

A more robust approach is to apply the same principle of a weighted sum in the fit itself. The log likelihood function of expression 4.4 is modified to:

$$\ln L = \sum_{i,j} \ln(1.0 + X^2_{(i,j)} + \frac{8}{3} A^{mes}_{FB(j)} X_{(i,j)}) \tag{4.9}$$

where j runs over the number of $|Q_{FB}|$ bins, i runs over all events in the bin and $A^{mes}_{FB(j)}$ is given by:

$$A^{mes}_{FB(j)} = \sum_{q=uds,c,ww} D_{q,j} A^{q,j}_{FB(S\prime)} F_{q,j} \tag{4.10}$$

where $F_{q,j}$ are the relative quark abundances in each Q_{FB} bin ,$A^{q,j}_{FB(S\prime)}$ are the true quark asymmetries after the $S\prime$ cut and $D_{q,j}$ the dilution factors for each quark flavour in each Q_{FB} bin. This way all the sample is fitted simultaneously with a single A^b_{FB} for all bins. Figure 4.14 shows the distribution of the A^b_{FB} measurements and the corresponding assigned errors in the MC study for the 6 $|Q_{FB}|$ bin case. The figures show a better compatibility between the width of the A^b_{FB} distribution and the mean of the assigned error distribution than seen in figure 4.13 for the weighted sum approach. Figure 4.15(right) shows the corresponding pull distribution. The mean of the pull distribution is consistent with zero and the width consistent with 1 showing that the reconstructed asymmetry values and errors correctly represent the generated distribution.

Figure 4.16 shows the error reduction against the number of $|Q_{FB}|$ bins that the initial sample is divided into, for the 1998 data set. The bin divisions are chosen such that in each bin there are similar numbers of events. The maximum

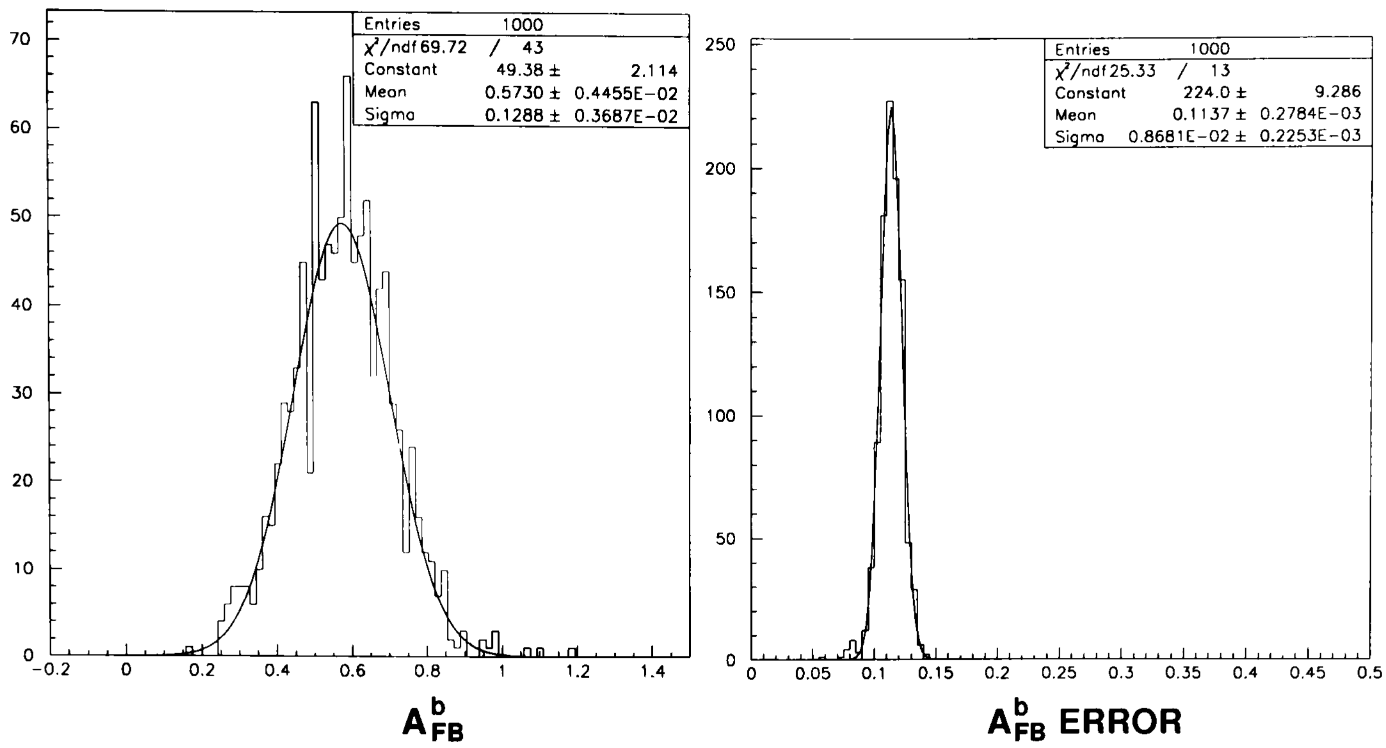

Figure 4.13: Results of the MC study for the weighted mean approach. Each entry corresponds to a separate MC experiment. On the left side is the distribution of A^b_{FB} measurements. On the right side is the distribution of the A^b_{FB} errors.

error reduction is 20% with respect to the unbinned approach using the 1998 data, and there is a good agreement in the error reduction observed in the data to that expected from the MC. For both the most significant error reduction is mostly observed when subdividing into 3 bins, and thereafter saturates. Similar behaviour is seen in the other years. We can learn from figure 4.16 using a more sensitive way to correct for the charge miassignment by using a function for the dilution correction is not really needed as the error reduction saturates after 4 bins in Q_{FB}.

4.3.3 Optimization of analysis working points

All results so far presented have assumed a specific choice of b tag working point for the event selection, and κ value for the jet charge reconstruction. This section justifies how these values are chosen.

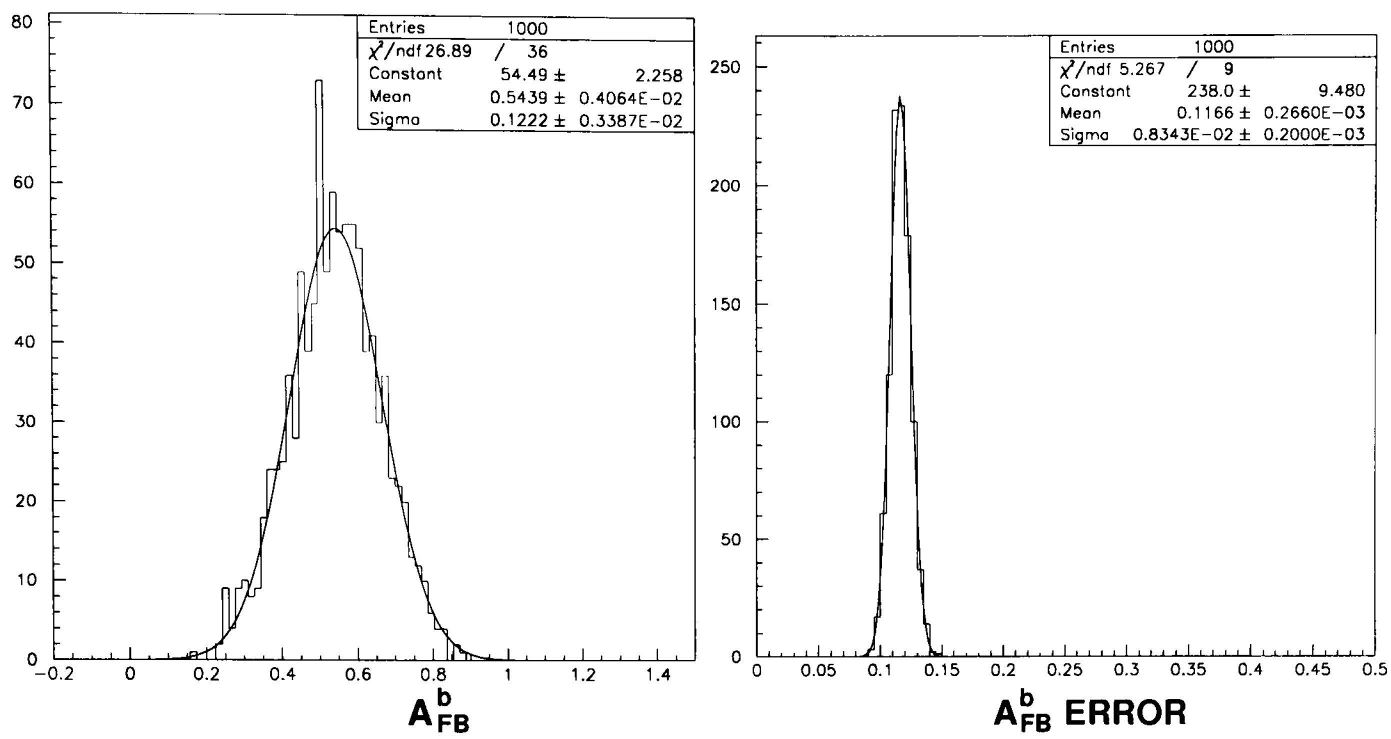

Figure 4.14: Results of the MC study for the weighted fit approach. Each entry corresponds to a separate MC experiment. On the left side is the distribution of A^b_{FB} measurement. On the right side is the distribution of the assigned Error coming from the fit.

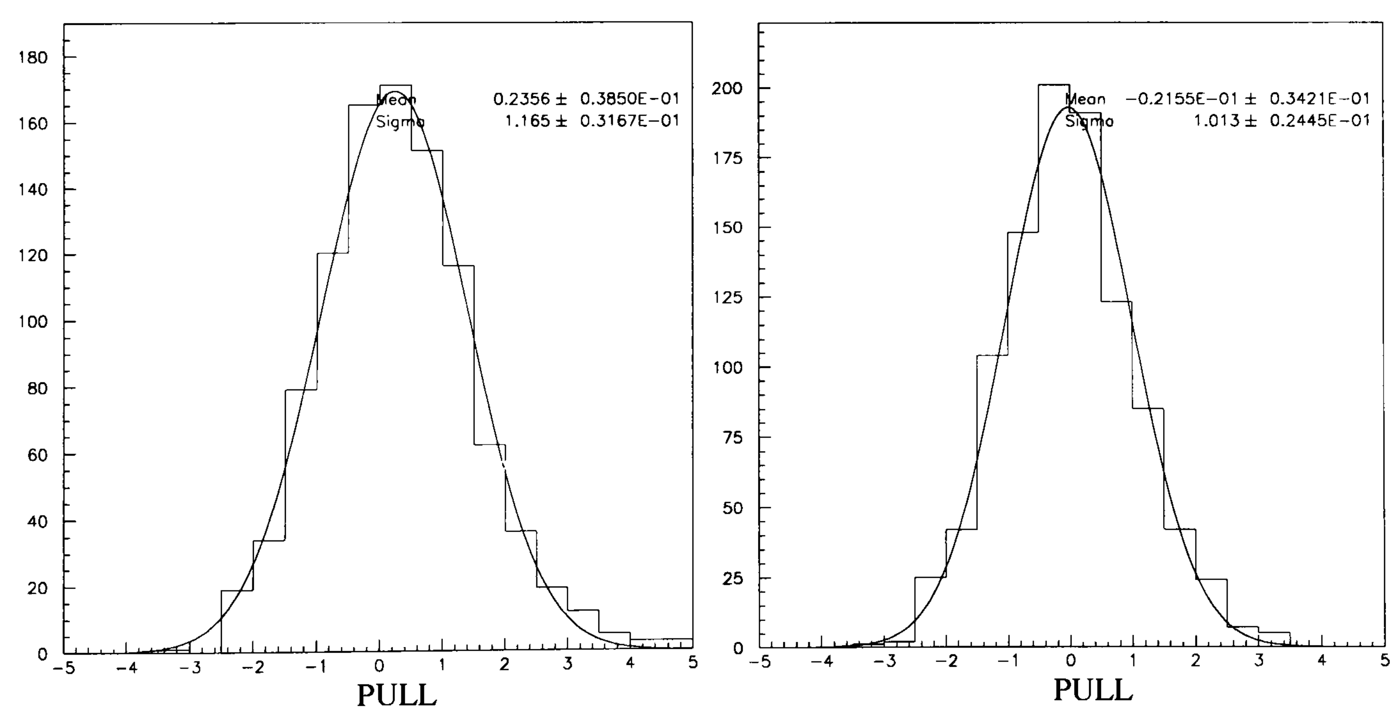

Figure 4.15: On the left side is the Pull Distribution for A^b_{FB} measurement obtained using a weighted combination. On the right side is the Pull Distribution for A^b_{FB} measurement obtained using a weighted fit.

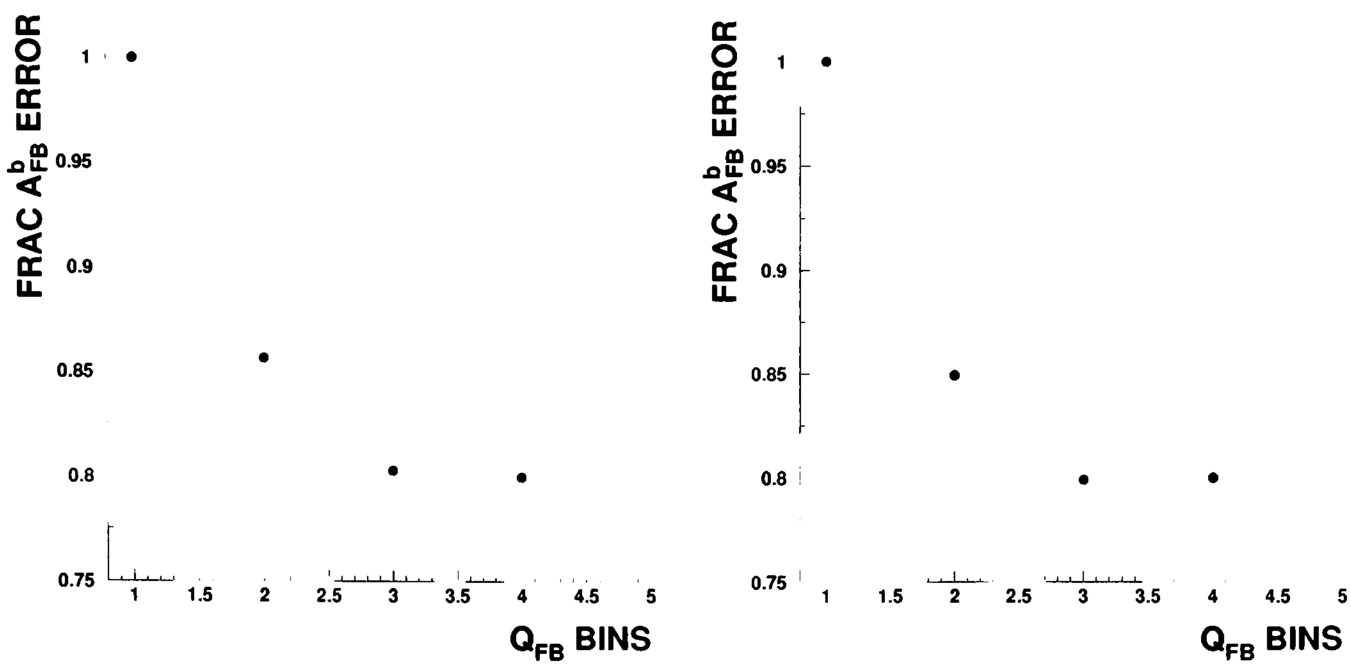

Figure 4.16: On the left side is the normalized error on the asymmetry obtained from MC against number of bins. On the right side is error reduction from real data against number of bins. The errors are normalized to the first bin. This study was done for the 1998 data set.

Choice of the b Tag Cut

The choice of the best place to make the b tag cut is made by first studying the A^b_{FB} statistical error obtained at different working points. This is shown in figure 4.17 for 1998 data set. This suggests placing the working point at a b tag cut of 1. In order to verify this conclusion remains valid when systematics are included the study was extended. The value of the background corrections for the W^+W^- and charm events was varied by 50% and 25% respectively, and the b fraction by 0.5%(the choice of these numbers is explained in section 4.5). The results of these changes on the measurement are shown in table 4.4 for the points of interest around the minimum error values. It can be seen that the systematic error is always much smaller than the statistical error and does not affect the conclusion drawn from figure 4.17. From this it is shown that the best working point is at cut of 1. The stability of the optimal b working point was checked in this manner for all the data analyzed. In all cases, the same working point value of b tag cut of 1 was found to be optimal. This is unsurprising as the b purity is similar for all years at this

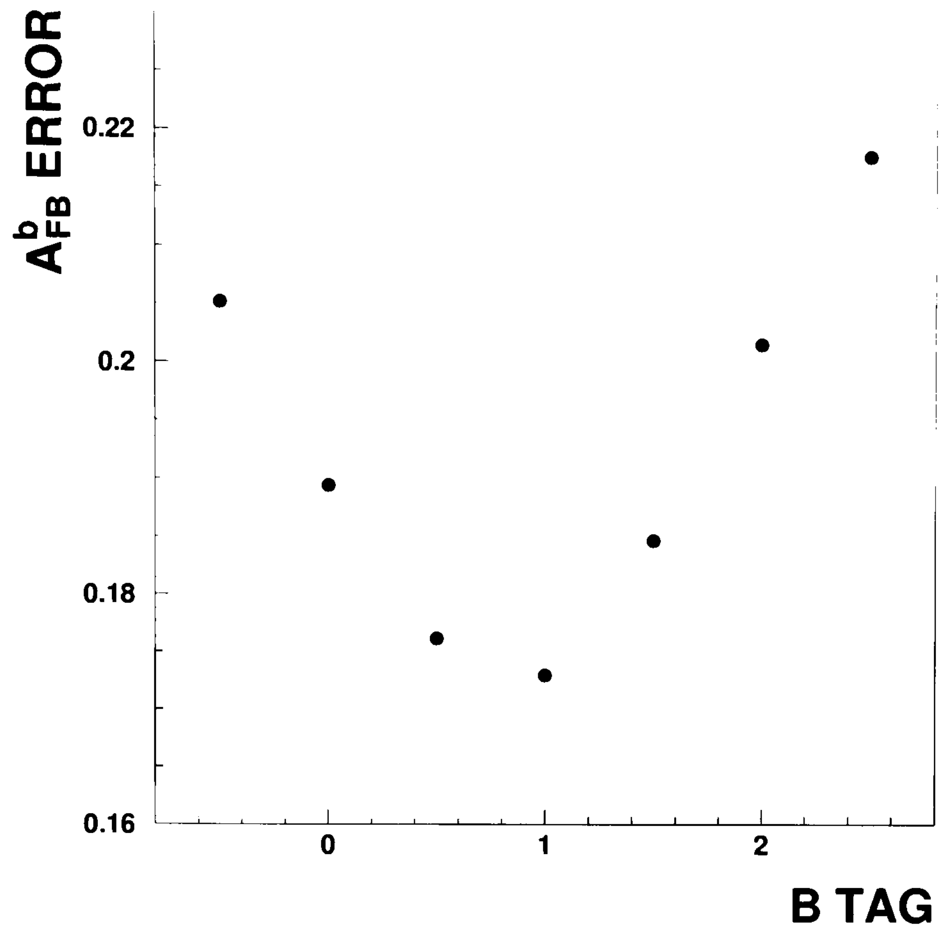

Figure 4.17: b tag cut versus A^b_{FB} statistical error for 1998 data.

working point, as seen in table 4.2.

Choice of the κ value

The choice of the best κ value to be used in the jet charge variable has been determined on real data. The value of the statistical error obtained from the A^b_{FB} measurement was studied with respect to the κ value used. Figure 4.18 shows the error against the κ value used for 2000 data. A similar result with the same min-

B tag point	0.5	1.0	1.5
Stat. error	0.1767	0.1735	0.1853
Syst. error	0.0474	0.0297	0.0243
Combined error	0.1829	0.1760	0.1868

Table 4.4: b tag working point study for 1998 data.

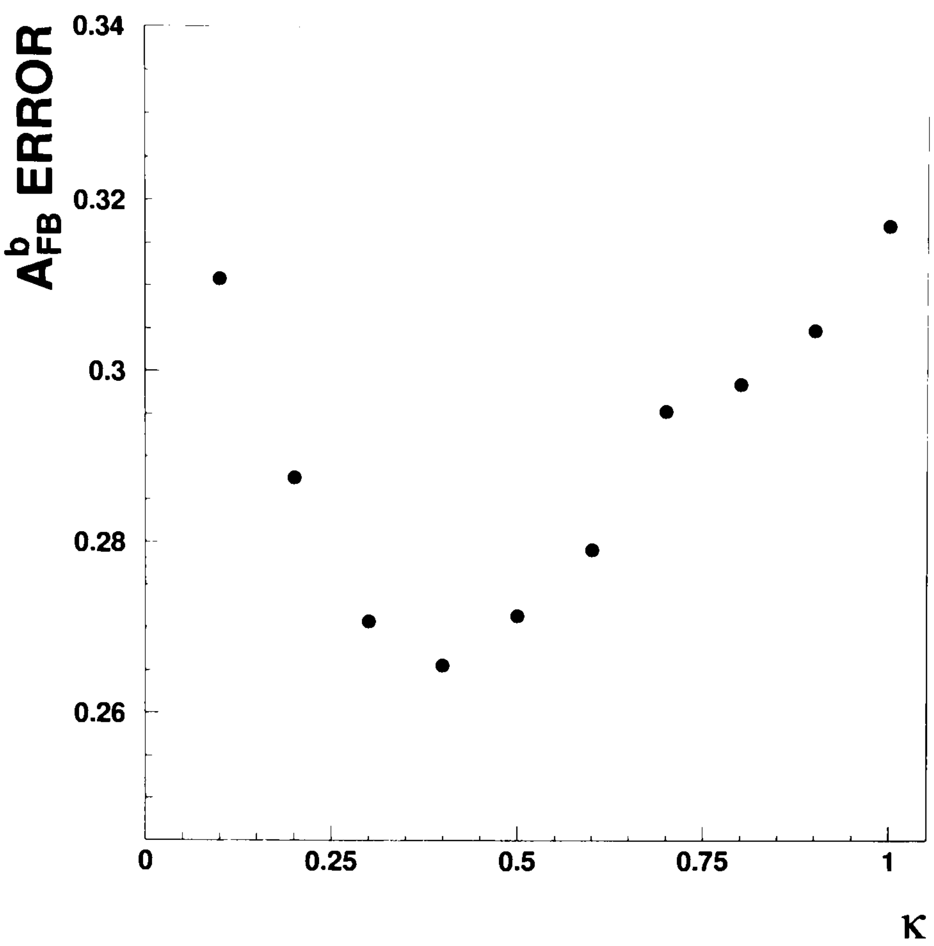

Figure 4.18: A^b_{FB} statistical error versus the κ value for 2000 data.

imum value is observed in all the data sets. The variation of the A^b_{FB} error with κ arises from the different dilution value associated with each κ value. The stability of this figure was checked with KK2F and ARIADNE MC simulations. Figure 4.19 shows the distributions of the κ against A^b_{FB} statistical error for KK2F and ARIADNE MC. The minimum in all curves is around 0.4. In the measurement a slightly larger κ value of 0.5 is chosen in order to avoid being close to the sharply rising trend at low κ values.

4.4 Results

The asymmetry values obtained for the different energies are presented in table 4.5. The asymmetry values for 2000 data split into the TPC bad and TPC good periods are presented in table 4.6. We can see that the central values of the TPC bad data are rather different from the TPC good data and also not always in the physical

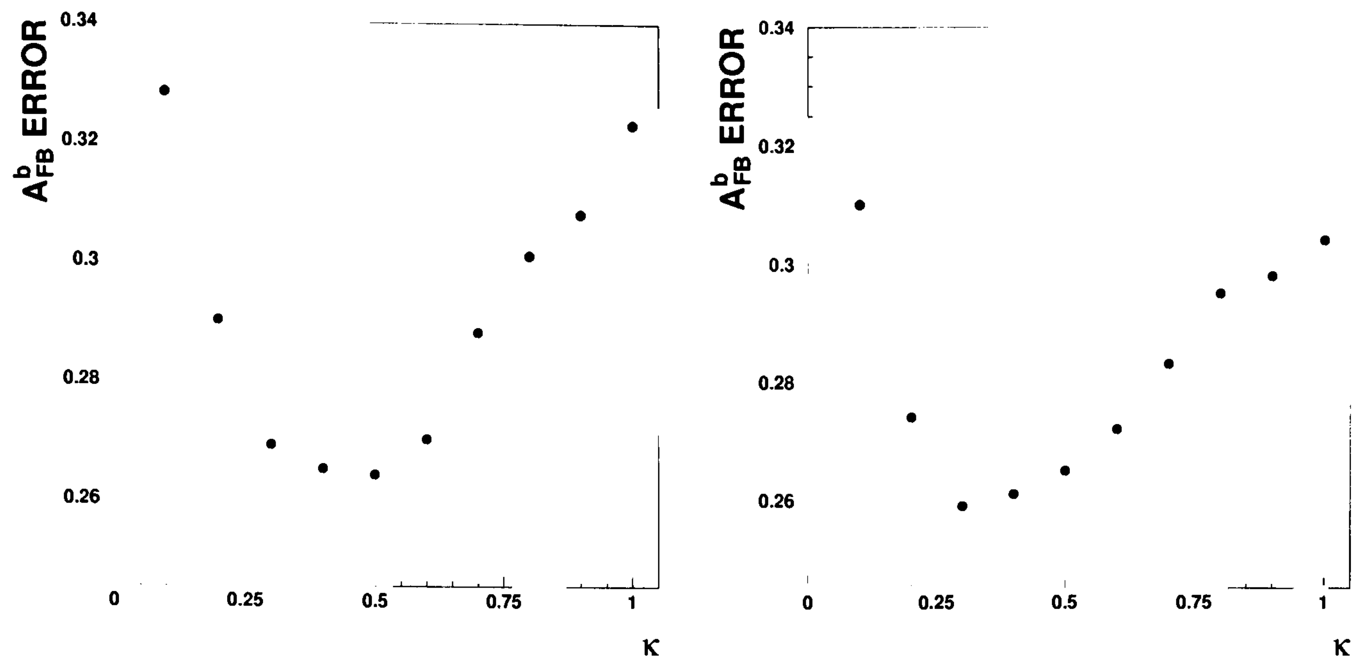

Figure 4.19: On the left is the A^b_{FB} statistical error against κ for KK2F MC. On the right is the A^b_{FB} statistical error against κ for ARIADNE MC.

Energy (GeV)	number of selected events	A^b_{FB} ± stat ± syst
183	119	-0.053 ± 0.213 ± 0.010
188.6	358	0.690 ± 0.173 ± 0.051
191.6	66	0.232 ± 0.277 ± 0.019
195.5	161	0.711 ± 0.166 ± 0.041
199.5	182	0.516 ± 0.160 ± 0.029
201.6	88	0.630 ± 0.225 ± 0.035
204.8	145	0.752 ± 0.254 ± 0.059
206.6	240	0.138 ± 0.200 ± 0.020

Table 4.5: A^b_{FB} results.

range. However this is not in itself worrying given the large value of the statistical uncertainty associated with these small sub-samples.

4.5 Systematic studies

4.5.1 Dilution related systematic

The main correction to the measurement comes from the dilution factor. Therefore potential dilution systematics require close attention. The systematic error on the dilution was assessed using the $Q_F + Q_B$ distribution (figure 4.8). This distribution

Energy (GeV)	number of selected events	$A^b_{FB} \pm$ stat
204.8 TPC (G)	133	0.684 $\pm$ 0.271
206.6 TPC (G)	166	0.142 $\pm$ 0.240
204.8 TPC (B)	13	1.595 $\pm$ 0.711
206.6 TPC (B)	72	0.045 $\pm$ 0.344

Table 4.6: A^b_{FB} results for 2000 data.

was used as it not sensitive to the value of the asymmetry, but rather illustrates the goodness of the data-MC agreement. Any discrepancy would be caused by one or more of the following errors in the MC:

1. Poor modeling of the detector response;

2. Poor description of the hadronisation process;

3. Poor description of the primary stage physics process; eg. b decay multiplicity.

The studies presented here in principle constrain all 3 effects. However to be conservative, source 3) is evaluated separately in section 4.5.2.

Figure 4.8 shows reasonable compatibility between data and MC but not perfect agreement as the data width is larger than the MC: the data RMS value is 0.299 and the MC RMS value is 0.278. By varying the κ parameter in the MC alone, the MC resolution may be degraded to match the data. The corresponding change in the dilution provides an estimate of the systematic associated with the initial data-MC discrepancy. This is performed on the combined distribution of $Q_F + Q_B$ from all the years, with the data κ parameter fixed at 0.5. Optimum agreement is achieved when the MC κ parameter is varied to $\kappa = 0.55$. The resulting distributions are seen in figure 4.21. The corresponding change in the dilution factor is 3%.

A further study is to compare the dilution values obtained from the ARIADNE MC to the KK2F MC. The ARIADNE dilution values for the different years are given in table 4.7 and should be compared to the KK2F values seen in table 4.1 for the one Q_{FB} bin. There is a good agreement between these sets of values within the statistical errors. This suggests that there are no severe systematics associated with the hadronisation process. The same κ fit procedure was repeated with ARIADNE MC. Figure 4.22 shows the $Q_F + Q_B$ distribution with the MC fitted to the data. The corresponding change in the dilution factor was of 2.5% which is consisted with the value obtained from the KK2F MC.

Another potential dilution systematic arises from the event's charged multiplicity and track momentum distributions presented in figures 4.9 and 4.10. In the multiplicity case, we can see that there is an excess of data at low and high multiplicity values. However, this disagreement is in regions of very low statistics and the effect of these on the analysis results is expected to be negligible. In the track momentum case, there is an excess of data events at low and high momentum values. In order to asses what effect these disagreements may have on the result we have recalculated the dilution value after discarding tracks with momentum less than 3 GeV and accounted for the disagreements at higher momentum values by fitting the offset and slope, as seen in figure 4.20. These results were then used to give each track a weight, w_i, according to:

$$w_i = 0.9851 + 0.00219 \cdot p_i \tag{4.11}$$

where p_i is the momentum of track i. This weight is inserted into the jet charge definition:

$$Q_{F(B)} = \frac{\sum_i |w_i p_i \cdot \hat{n}|^\kappa q_i}{\sum_i |p_i \cdot w_i \cdot \hat{n}|^\kappa} \tag{4.12}$$

The effect of these changes on the dilution value is 3%.

In summary, the systematic errors associated with the dilution are:

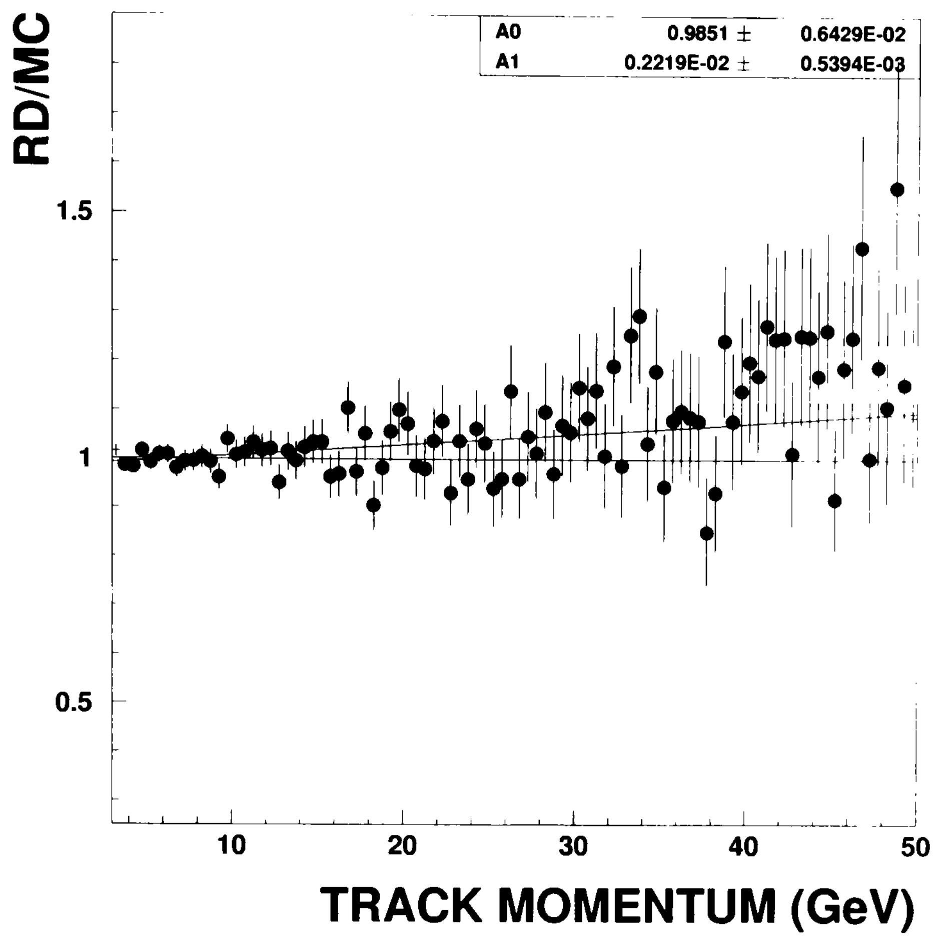

Figure 4.20: The ratio of data and MC for the track momentum variable for all data combined.

	1997	1998	1999	2000(g)	2000(b)
dilution	0.365 ± 0.023	0.355 ± 0.024	0.324 ± 0.027	0.351 ± 0.026	0.342 ± 0.026

Table 4.7: ARIADNE MC dilution values for all the data sets.

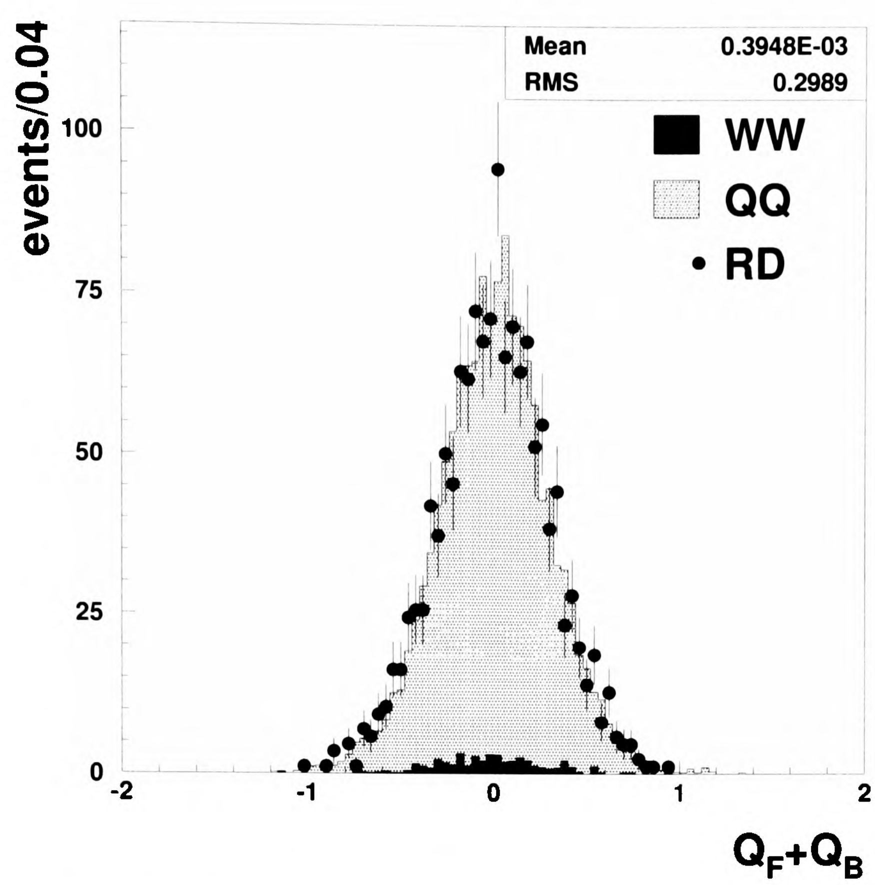

Figure 4.21: The distribution of $Q_F + Q_B$ variable with the KK2F MC κ parameter varied to optimally fit the data distribution.

- **Dilution(κ)**: the b dilution as determined from KK2F MC was varied by 3% according to the κ parameter fit in the $Q_F + Q_B$ distribution as explained above.

- **Dilution(p)**: The b dilution as determined from KK2F was varied by 3% to allow for the data and MC disagreement in the track momentum distribution as explained above. This observable may be correlated with the Dilution(κ) systematic but it is included as a separate error source since the dilution is such an important correction to the measurement.

- **Dilution statistics**: the dilution was changed by its statistical error taken from the MC.

Dilution related systematics associated with the description of the primary physics process are evaluated in next section.

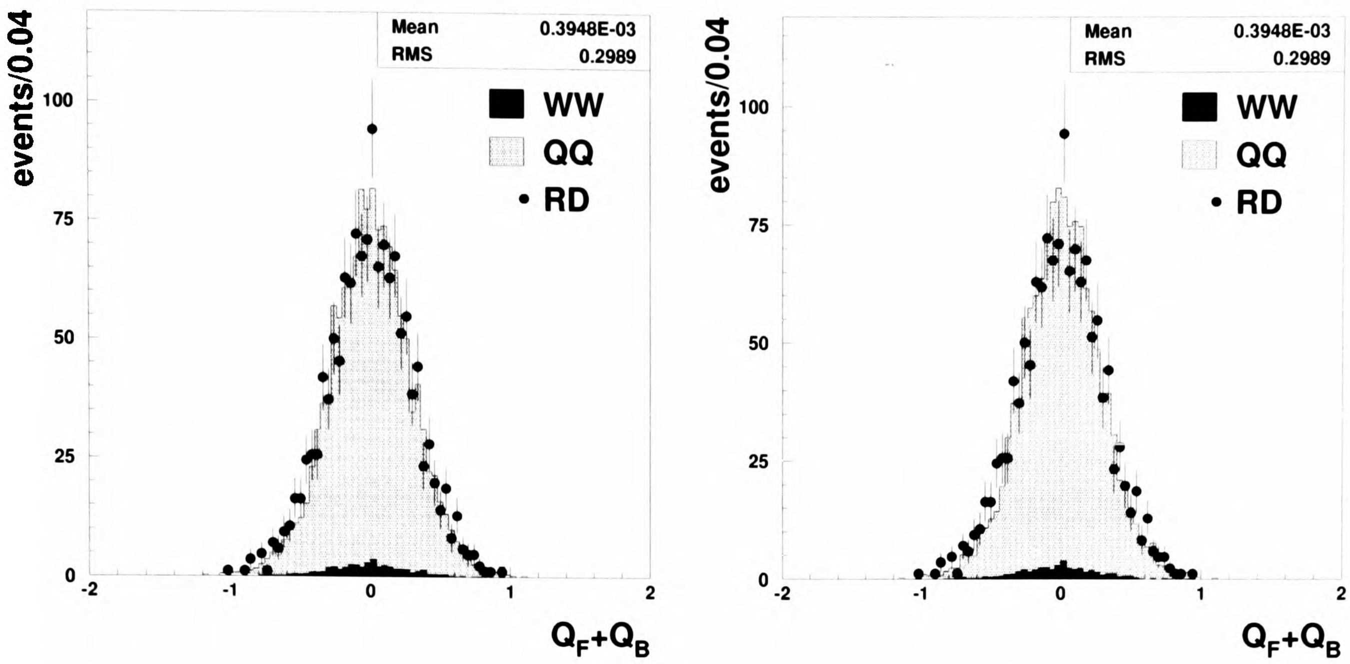

Figure 4.22: On The left: The distribution of $Q_F + Q_B$ variable with the MC κ parameter varied to optimally fit the data distribution for ARIADNE MC. On the right: The distribution of $Q_F + Q_B$ variable before the κ fit.

4.5.2 Physics parameters in the MC

There are key physics quantities used in the MC that have an effect on the measurement. In order to study the stability of the measurement these quantities have to be varied in the MC. The physics quantities considered are as below. Also shown are the world averaged measurements.

- mean b hadron decay multiplicity. The world average value is 4.955 ± 0.062[28].
- mean b lifetime. The world average value is 1.576 ± 0.016[28].
- b fragmentation: defined as the fraction of charged energy taken by the b hadron with respect to the beam energy. The world average value is 0.702 ± 0.008[28].
- b hadron composition. The b hadron types and rate of production at LEP2 are shown in table 4.8 [28].
- B mixing parameter. The world average value is $\chi = 0.1189 \pm 0.004$[28].

Hadron type	Rate of production
$B^{\pm}$	0.389 ± 0.013
B^0	0.389 ± 0.013
B^0_s	0.107 ± 0.014
B baryon	0.116 ± 0.002

Table 4.8: This table Shows the production rates that we expect for beauty flavour jets at LEP2[28]. B^0_c production can be neglected.

The default values of parameters in the MC are consistent with these world averages.

The main use of the MC in this measurement is for evaluating the dilution factor and the b purity. Therefore it is necessary to study how these corrections depend on key physics quantities.

In the decay multiplicity case, the MC is divided into 5 subsamples from low to high multiplicity. In each subsample the value of the dilution is evaluated. From these values the slope of dilution with decay multiplicity, $\frac{\Delta D}{\Delta M}$, is determined. This is seen in figure 4.23. One can see how the dilution decreases with multiplicity. This is due to the fact the the jet charge works better when the b charge information is carried by very few tracks from the b hadron. The dilution value corrected for a 1 σ change in the b multiplicity, is calculated as:

$$D_{cor} = D + \frac{\Delta D}{\Delta M} \cdot \sigma \tag{4.13}$$

where D is the uncorrected dilution, $\frac{\Delta D}{\Delta M}$ is the slope taken from the fit to figure 4.23 and σ is the change in the b hadron multiplicity that we are considering. The value of σ is taken to be the uncertainty on the world average as stated earlier. In a similar way the change in the b efficiency was calculated. Figure 4.24 shows the efficiency dependence on the b hadron multiplicity. One can see that the b efficiency increases with multiplicity . This is due to the fact that the life time information

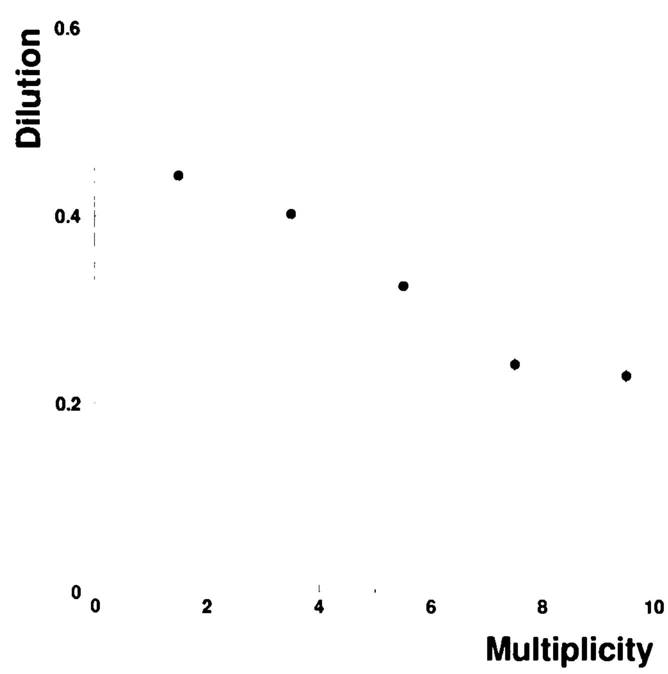

Figure 4.23: The variation of dilution against b hadron decay multiplicity for all MC combined.

carried by all the b hadron tracks increases the discrimination of the b tag. A similar procedure has been followed for the mean b life-time and fragmentation systematics.

In the composition case the procedure was different. Neglecting the very rare B_c decays, the b can hadronize into 4 possible hadrons: $B^{\pm}, B^0, B_s^0$ or a B baryon. The systematic study consists of varying the B_s^0 fraction with respect to the rest. For this, the event sample was divided into 3 categories: 2 B_s^0's, B_s^0 + others, neither B_s^0. For each subsample the dilution value and b efficiency are evaluated. From the fraction of events in each subsample one can calculate the mean dilution and efficiency for an assumed fraction of B_s^0 mesons. Changing the B_s^0 fraction changes the relative weight of each subsample and leads to new dilution and efficiency values.

A similar procedure has been performed in the b mixing case where the sample was subdivided into events where neither hadron oscillated, only one oscillated and both oscillated.

A summary of the physics parameters shifts and slopes are presented in table 4.9.

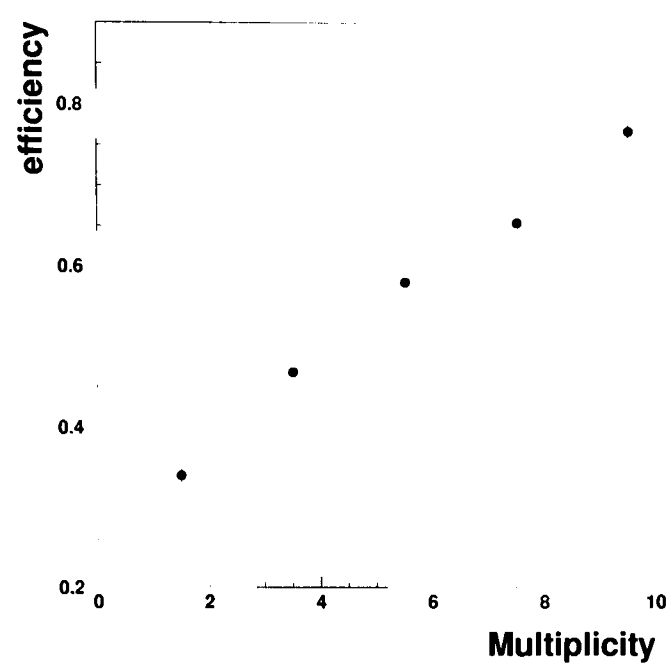

Figure 4.24: The efficiency against b hadron multiplicity for all MC combined.

4.5.3 Background related systematics

The systematic error associated with the background are evaluated by varying the listed parameters by the amount listed below, and refitting the asymmetry.

- b fraction: the fraction of b in the sample has been changed according to the efficiency change as measured on the Z^0 data of that year.
- c fraction: the c number of c events has been changed by 25%. The change of 25% is chosen after varying the charm fraction in the MC and comparing this to the number of real data event. A 25% change gives a difference between the data and total number of expected MC events at the 2 sigma level.
- W^+W^- fraction: the W^+W^- fraction has been changed by 50%. This has been a conservative error assignment.
- $S\prime$ correction: the error is taken as 50% of the total $S\prime$ correction on the measurement. This has been a conservative error assignment.

The systematic uncertainties for all the data sets are presented in table 4.10.

1997			
	amount varied by	fitted value of $\frac{\Delta D}{\Delta x}$	fitted value of $\frac{\Delta E}{\Delta x}$
b multiplicity	0.0619	-0.0261	0.0477
b fragmentation	0.0080	0.2313	0.2849
b life time	0.0159	-0.0072	0.0018
	amount varied by	shift in dilution	shift in efficiency
b hadron composition	0.0141	0.0019	0.0004
b mixing	0.0042	0.0055	0.0008
1998			
	amount varied by	fitted value of $\frac{\Delta D}{\Delta x}$	fitted value of $\frac{\Delta E}{\Delta x}$
b multiplicity	0.0619	-0.0346	0.0567
b fragmentation	0.0080	0.2611	0.3651
b life time	0.0159	-0.0159	0.1123
	amount varied by	shift in dilution	shift in efficiency
b hadron composition	0.0141	0.0015	0.0003
b mixing	0.0042	0.0025	0.0004
1999			
	amount varied by	fitted value of $\frac{\Delta D}{\Delta x}$	fitted value of $\frac{\Delta E}{\Delta x}$
b multiplicity	0.0619	-0.0287	0.0556
b fragmentation	0.0080	0.1501	0.2441
b life time	0.0159	-0.0112	0.1354
	amount varied by	shift in dilution	shift in efficiency
b hadron composition	0.0141	0.0021	0.0004
b mixing	0.0042	0.0020	0.0005
2000 TPC good			
	amount varied by	fitted value of $\frac{\Delta D}{\Delta x}$	fitted value of $\frac{\Delta E}{\Delta x}$
b multiplicity	0.0619	-0.0416	0.0533
b fragmentation	0.0080	0.1745	0.2751
b life time	0.0159	-0.0441	0.1412
	amount varied by	shift in dilution	shift in efficiency
b hadron composition	0.0141	0.0047	0.0006
b mixing	0.0042	0.0037	0.0005
2000 TPC bad			
	amount varied by	fitted value of $\frac{\Delta D}{\Delta x}$	fitted value of $\frac{\Delta E}{\Delta x}$
b multiplicity	0.0619	-0.0624	0.0531
b fragmentation	0.0080	0.4011	0.1971
b life time	0.0159	-0.3515	0.1393
	amount varied by	shift in dilution	shift in efficiency
b hadron composition	0.0141	0.0018	0.0005
b mixing	0.0042	0.0017	0.0005

Table 4.9: physics parameter shifts for all years of MC used. $\frac{\Delta D}{\Delta x}$ and $\frac{\Delta E}{\Delta x}$ are the dilution and efficiency slopes respectively.

E_{cm}(GeV)	183	189	192	196	200	202	205	207
dilution(κ)	0.14	2.10	0.74	2.20	1.59	1.93	2.33	0.48
dilution stat	0.24	2.50	1.15	1.25	0.39	0.56	3.79	1.14
dilution(p)	0.14	2.10	0.74	2.20	1.59	1.93	2.33	0.48
multiplicity	0.20	0.45	0.12	0.36	0.26	0.32	0.61	0.13
fragmentation	0.20	0.41	0.08	0.24	0.17	0.21	0.33	0.07
lifetime	< 0.01	0.05	0.01	0.03	0.02	0.02	0.17	0.04
composition	0.03	0.33	0.12	0.37	0.33	0.32	1.10	0.22
B-B mixing	0.07	0.55	0.13	0.38	0.28	0.34	0.87	0.18
b fraction	0.26	0.34	0.37	0.58	0.49	0.54	0.96	0.56
c fraction	0.68	2.94	1.00	1.59	1.26	1.54	2.03	1.14
W^+W^- fraction	0.36	0.28	0.29	0.11	0.11	0.27	0.39	0.55
S_f correction	0.46	1.37	0.03	1.57	0.94	1.30	1.47	0.64
Total	1.01	5.12	1.91	4.10	2.86	3.54	5.91	2.04

Table 4.10: Systematic errors on A^b_{FB} at each energy point, all in units of 10^{-2}.

The total systematic uncertainties have a dependence on the magnitude of the raw asymmetry they are evaluated on. This dependence arises from the dilution correction applied to the measurement. This dependence is most clearly seen in the dilution systematic. As the dilution correction essentially enters as a multiplicative factor, the size of the associated error will depend on the value of the raw asymmetry. This is not true however of the background related systematics. Therefore the relative importance of each error component varies from year to year, depending on the central value of the asymmetry and the proportion of background.

From table 4.10 we can see that in general the most important systematic errors are the dilution and c fraction. This is because the dilution is the main correction to the measurement and the c fraction is the main background. Although the c contamination is relatively small it has a large effect as the the c quark has a positive charge and therefore the events are measured with a negative asymmetry. This can be seen in table 4.1.

The errors have been assumed independent and are thus summed in quadrature. The value of the total systematic error is small with respect to the statistical error.

This is shown in table 4.5. This is due to the relatively small data sample collected which arises from the small cross section of the process $e^+e^- \to q\bar{q}$ at high energy.

4.5.4 A^b_{FB} at the Z^0

In order to verify the method used to measure A^b_{FB}, a cross check has been made using the Z^0 calibration data from the LEP2 running. The A^b_{FB} value at the Z^0 pole is a well known quantity from the LEP1 period and it is important to check that we get a consistent value using the measurement procedure described in this chapter. The A^b_{FB} numbers measured in each year are presented in table 4.11. These results should be compared to the DELPHI LEP1 results of $A^b_{FB} = 0.0982 \pm 0.0047$[27] and the Standard Model prediction obtained from ZFITTER[26] of $A^b_{FB} = 0.0990$. One can see that the results are consistent with these values, giving confidence in the method.

Year	$A^b_{FB} \pm$ stat
1997	0.092 ± 0.038
1998	0.173 ± 0.040
1999	0.020 ± 0.040
2000 (G)	0.065 ± 0.039
2000 (B)	0.115 ± 0.042
Mean	0.088 ± 0.019

Table 4.11: A^b_{FB} results at $\sqrt{S} = 91.2$ GeV for Z^0 running.

5. C Selection and A^c_{FB}

5.1 Introduction

This chapter presents a neural net based attempt to enrich the high $S\prime$ sample in charm events. The forward-backward asymmetry of these events is then evaluated for each data set separately.

The selection of b events discussed in chapter 3 provides a convenient basis for the selection of c events. However the c identification presents a unique challenge. Unlike b events where the long lifetime presents a clear signature, a c event has no outstanding characteristic to separate it from the rest of the background. In fact, by looking at figures 3.11 and 3.12 it is seen that in most of the variables the c events take intermediate values between those of the b and the light quarks. This makes c tagging a difficult, but not impossible, challenge.

In this study because of the lower statistical precision of the measurement the separate energy points of 1999 and 2000 have been combined into two mean energies of 197.5 GeV and 205.5 GeV.

5.2 Improved 4-fermion suppression

Four-fermion events make only a small contribution to the background in the $b\bar{b}$ selection because the decay of W to b quarks is highly suppressed. For the c selection, however, the situation is very different as W's can decay into $\bar{c}s$. Therefore it is necessary to develop further cuts to suppresses this background. The total 4-fermion contamination after applying the event selection cuts described in chapter 3 is shown in table 3.2. Taking 1998 as an example, the relative contamination is 0.146. The 4 fermion background as evaluated in the MC corresponding to the 1998 data set subdivides as follows: 38% fully hadronic W^+W^- decays, 54% semi-leptonic W^+W^- decays and 7% Z^0Z^0 decays. The semi-leptonic decays are themselves made up of: 35% electrons, 36% muons and 29% tau decays. In order to boost the c-purity, cuts have been developed to target the W^+W^- component of this contamination.

5.2.1 Semi-leptonic events

In a semi-leptonic W^+W^- event , where one W decays hadronically and the other into a charged lepton and an anti-neutrino, the lepton is expected to be an isolated track with high momentum. This is not the case for a semi-leptonic quark decay within a jet, where the lepton is close to other tracks. The W^+W^- suppression attempts to use this signature.

The electron channel

The electrons are identified using the REMCLU[25] package discussed in chapter 2. In order for an event to be vetoed as an electron semi-leptonic W^+W^- event:

- At least one track has to be tagged as a 'loose' electron. If more than one track is tagged the track with the highest momentum is chosen.
- The track should have a momentum greater than 15 GeV.
- For the chosen electron candidate an isolation angle is calculated. In this procedure the angle of the track to all the other charged tracks in the event is evaluated and the smallest angle is defined as the isolation angle. An event is tagged as a semi-leptonic W^+W^- electron decay if the angle is bigger than 20°. The distribution of the electron isolation angle is shown in figure 5.1 together with the position of the cut. The distribution shows that W^+W^- events have higher values for the isolation angle.

The muon channel

The muons were identified using the MUFLAG[13] package as discussed in chapter 2. For an event to be classified a semi-leptonic W^+W^- muon decay a track with a 'very loose' or 'HCAL' tag is required. The momentum and isolation angle requirements are similar to the electron case with cuts at 15 GeV and 12° respectively. The distribution of the muon isolation angle is shown in figure 5.2 together with the position of the cut. A very clear separation can be observed between the W^+W^- and the $\overline{q}q$ events.

The tau channel

The cuts designed for the $W \rightarrow \mu\overline{\nu}$ and $W \rightarrow e\overline{\nu}$ events also suppress many of the $W \rightarrow \tau\overline{\nu}$, $\tau \rightarrow e/\mu\nu\overline{\nu}$ decays. However additional background remains from the other single prong and higher multiplicities decays. In an effort to reject semi-leptonic decays which do not have an electron or muon tag, and also to reduce the single prong hadronic decays, a further cut is applied. The aim is to again look for isolated tracks but without the lepton identification requirement. The procedure is to calculate for each track in the event the isolation angle ,as defined above, and to select the track with the largest isolation angle in each event. This was defined as the 'tau isolation angle'. The distribution of the tau isolation angle is shown in figure 5.3. An event is vetoed if the angle was above 80°. This loose cut was chosen to maximize the amount of signal remained.

Hadronic cut

The fully hadronic W^+W^- decays are further suppressed by a cut made on the event thrust. The distribution of the event thrust is shown in figure 5.4. Events with a thrust less than 0.77 are rejected.

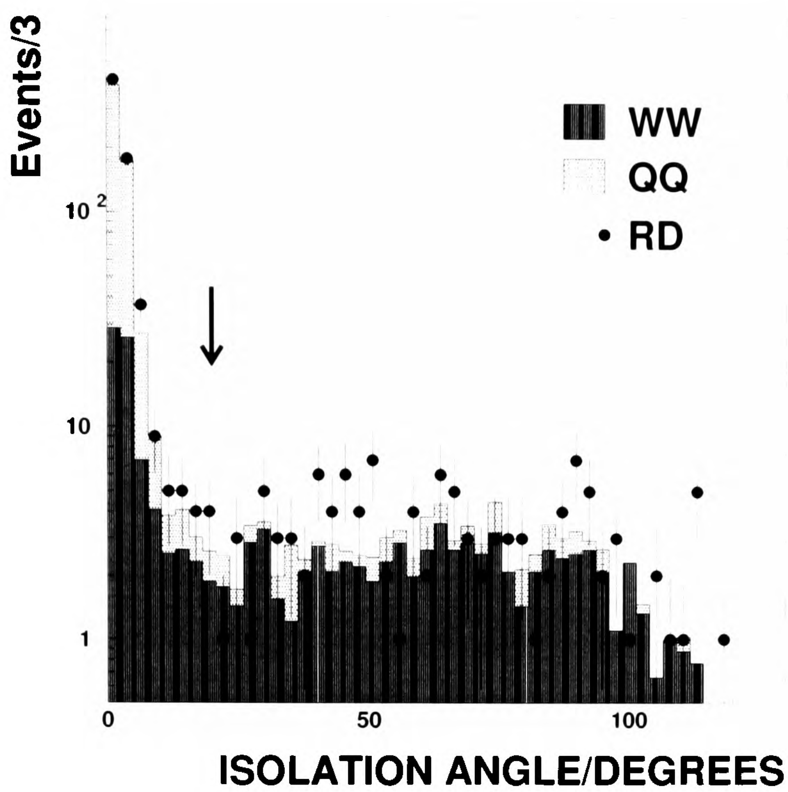

Figure 5.1: The distribution of the isolation angle for the electron channel. The arrow shows the cut above which the event is rejected from the sample.

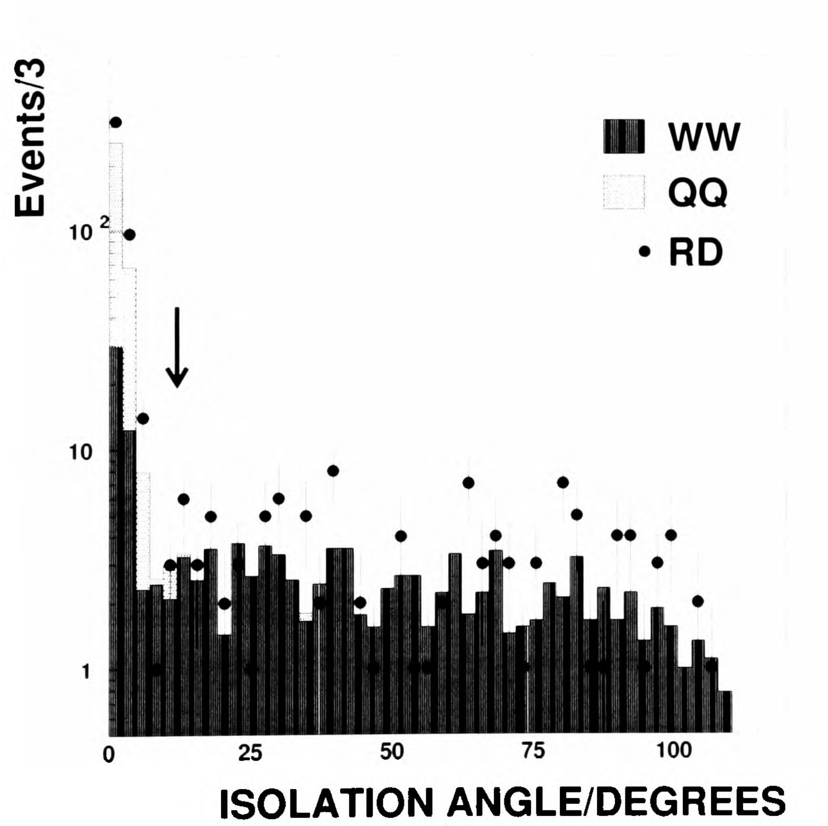

Figure 5.2: The distribution of the isolation angle for the muon channel. The arrow shows the cut above which the event is rejected from the sample.

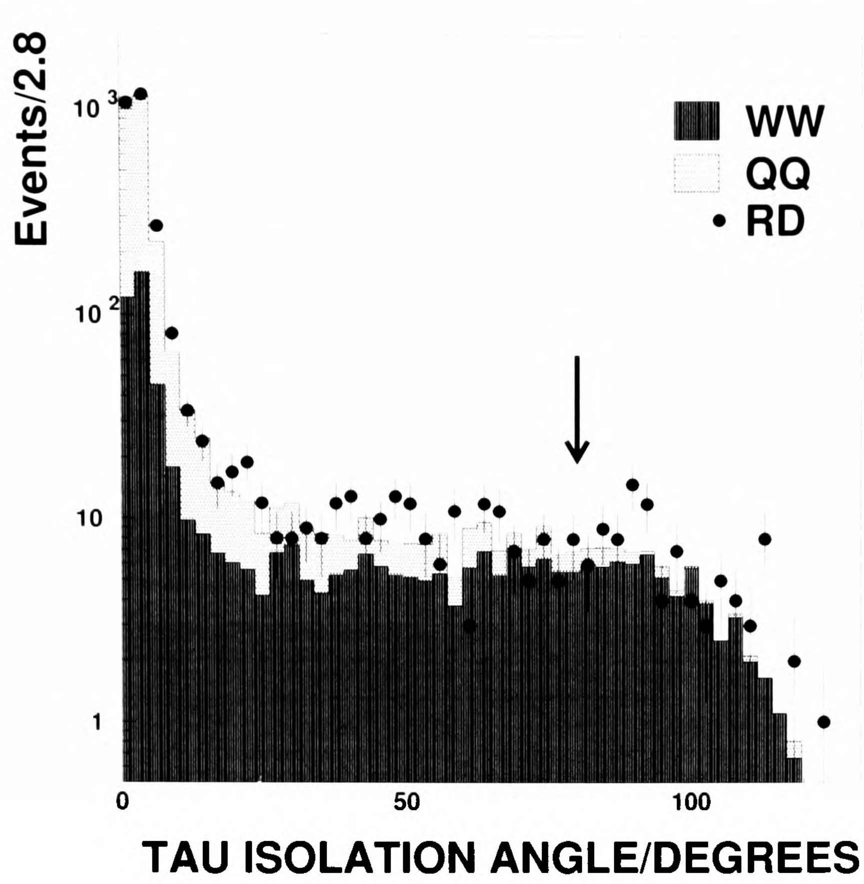

Figure 5.3: The distribution of the largest isolation angle in the event. The arrow at 80° shows the cut above which the event is rejected from the sample. This distribution is made before the electron and muon channels suppression.

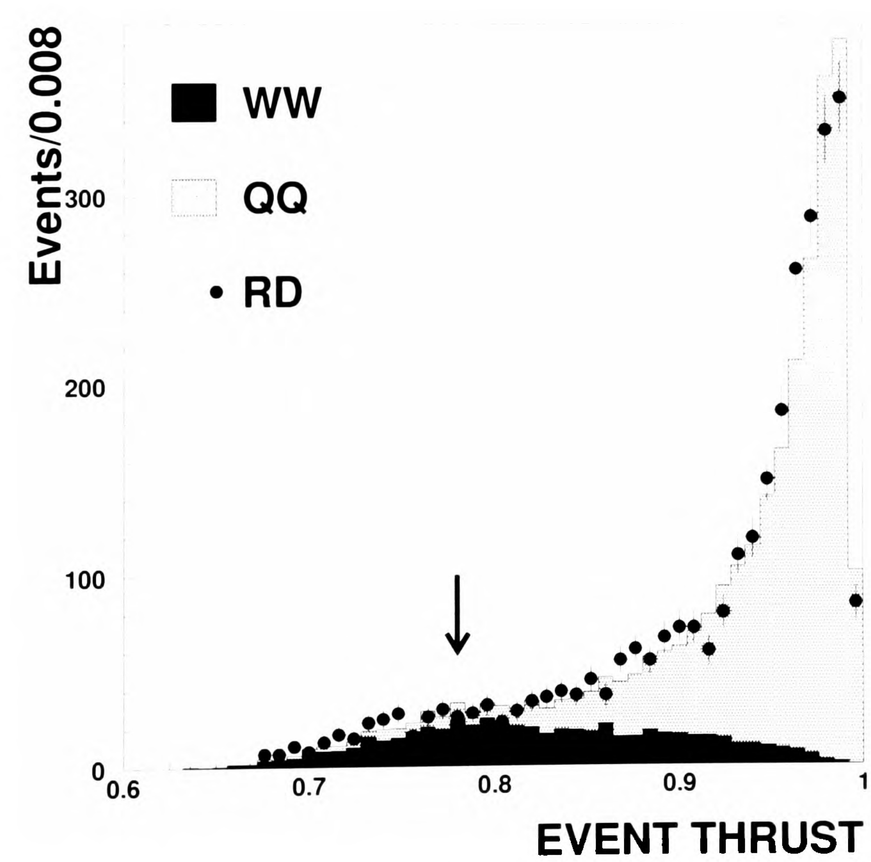

Figure 5.4: The distribution of the event thrust for 2000 data. The arrow shows the cut below which the event is rejected from the sample.

	Z^0Z^0	W^+W^-	uds fraction	c fraction	b fraction
1997	0.009	0.080	0.594	0.250	0.064
1998	0.010	0.087	0.588	0.253	0.060
1999	0.012	0.103	0.560	0.249	0.073
2000 good	0.015	0.123	0.547	0.244	0.068
2000 bad	0.015	0.121	0.542	0.242	0.077

Table 5.1: The hadronic sample composition 1997-2000 data sets after the improved W^+W^- rejection and the b veto.

The above set of cuts applied to the 1998 data set reduced the 4 fermion background from 14.6% to 8.2%, whilst keeping 97.5% of the charm events from the original sample. A similar performance is observed for the other years.

5.3 b veto

Events clearly identified by the b tag package as containing b quarks are removed from the sample. This b tag veto is an essential step in preparing a sample on which a NN could be trained to select c events. The cut is placed at a b tag variable value of 1.5. This suppressed 64% of the b events without any loss in c signal.

5.4 Sample composition prior to c tag

After applying all the cuts above the hadronic sample composition for the data sets used is shown in table 5.1. The number of events surviving in data and MC is shown in table 5.2. There is a reasonable agreement between data and MC, with a suggestion of a small data excess, similar to that discussed in section 3.2.4.

5.5 Additional variables used for C tagging

The variables used in the c tagging are all the same as those exploited in the b tagging, discussed in chapter 3, with two additional quantities:

	Int. Lum (pb^{-1})	Events after:			
		event cuts	4-f suppression	b tag veto	c tag cut
RD 1997	53.67	1353	1243	1148	582
MC 1997		1285	1196	1068	518
RD 1998	154.99	3570	3262	2982	1413
MC 1998		3462	3174	2829	1308
RD 1999	228.33	4681	4213	3812	1934
MC 1999		4483	4092	3719	1910
RD 2000 (G)	161.88	3033	2690	2461	930
MC 2000 (G)		2961	2693	2527	860
RD 2000 (B)	58.01	1057	956	890	288
MC 2000 (B)		1088	965	893	283
Tot RD/MC		1.031 ± 0.012	1.020 ± 0.013	1.023 ± 0.014	1.055 ± 0.021

Table 5.2: Steps in the c event selection. The 'event cuts' stage refer to the set of cuts described in chapter 3.

- **A mass cut variable.**

  In this variable we compute the invariant mass of a group of selected tracks, ordered in turn by decreasing inconsistency with the primary vertex. This inconsistency is based on IP information. Whenever the mass exceeds the value of 1.8 GeV, close to the mass of the D meson, a new variable is defined, P_m, being a linear sum of the probability of the latest added track to the mass computation, P_{tk}, and the jet probability P^{+}_{jet} :

$$P_m = 0.3 \log_{10}(P^{+}_{jet}) + 0.7 \log_{10}(P_{tk}) \tag{5.1}$$

  The exact definition of P^{+}_{jet} and P_{tk} can be found in chapter 3. The track probability is calculated in 3D from the probabilities in the rϕ and z projections. The values of the weights 0.3 and 0.7 are chosen in order to optimize the variable. The distribution of the mass cut variable is shown in figure 5.5.

- **The number of secondary vertices in the event.**

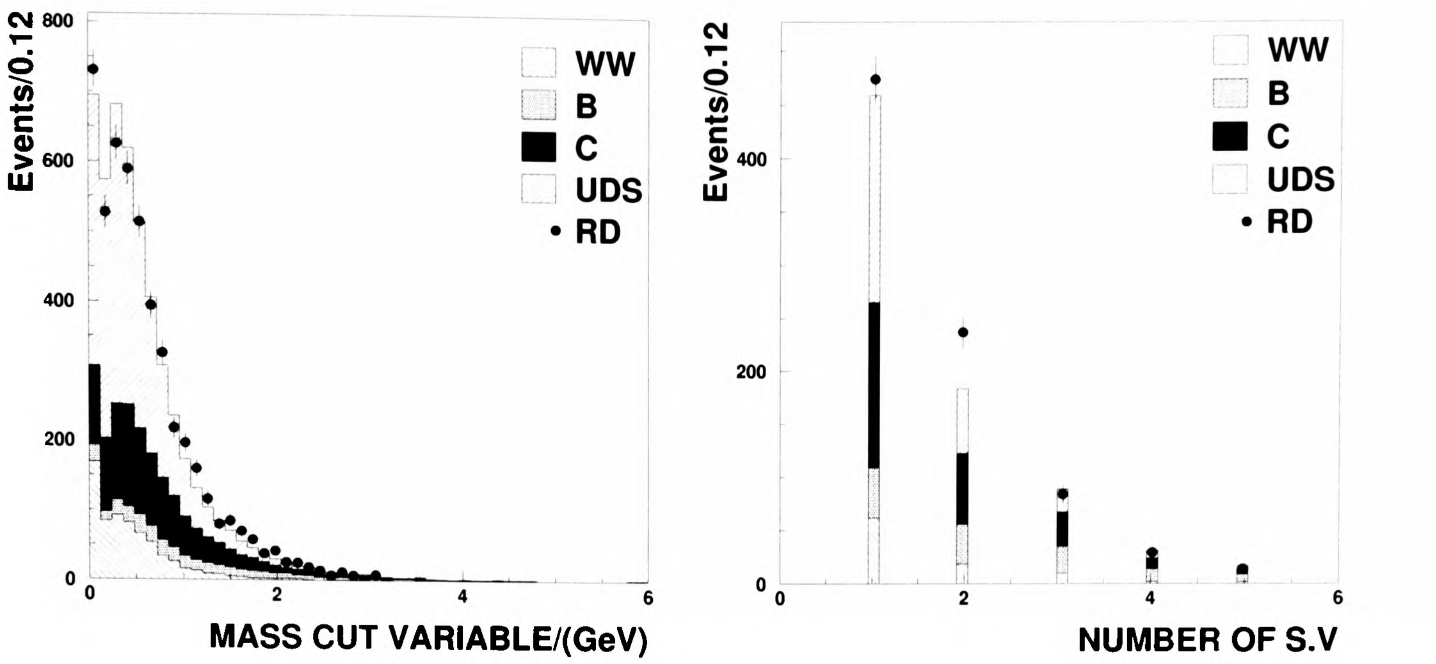

Figure 5.5: The distribution of the mass cut variable is shown on the left. On the right, the number of secondary vertices's in b,c uds and W^+W^- events. These distributions are made after applying the W^+W^- suppression and b veto cuts. These distributions are for 2000 data.

The purpose of this quantity is to distinguish between secondary vertices involving b decays, and those with charm decays. In the ideal case a $c\bar{c}$ event will be distinguished by 2 SVs, one corresponding to each D hadron decay point. A b event on the other hand will have 4 vertices, as each B will decay into a D which will in turn produce another secondary vertex. In uds events we expect no SVs. In reality, detector resolution will make the distinction much less clear, and there will be inefficiency and fake vertices. However the variable is still expected to be useful in selecting c events. The number of secondary vertices candidates is shown in figure 5.5 for b,c,uds and W^+W^- events.

5.6 C Tagging with a Neural Network

The method used to form the c tag is a Neural Network(NN). The advantage of using a NN as compared with other techniques such as the one used in the b case is that it has the ability to take into account the various correlations between different variables and combine them into one output variable.

5.6.1 How the NN works

When we want to separate a particular population of events from its background we usually make various cuts in our set of discriminating variables x_k. This procedure can often be quite tedious. In order to separate one population of events we can instead use a separating function $F(x_k)$ in terms of our variables x_k. This strategy is used in the operation of a NN. In this analysis we use a NN program called JETNET[22]. More details on JETNET and how it is used in this analysis can be found in Appendix A.

5.6.2 An illustrative example

The NN used in this analysis to tag c events includes many variables and has a detailed internal structure. This makes it hard to see how exactly the NN works. If we reduce the number of input variables to 2 and simplify the NN structure it is easier to follow the tagging procedure.

The two variable NN layout is shown in figure 5.6. The first layer corresponds to the input variables. The role of the second (or hidden) layer is to build up the internal representation of the observed data. The third layer is the output layer.

The two input quantities chosen are the lifetime and rapidity variables. These are the key signatures in c tagging. Figure 5.7 shows the distribution of the two variables one against the other for c, b, and uds events. The c events are concentrated in a region on the plane between the b and uds events. Figure 5.8 shows how the contour lines of the NN output optimally separate the c events in this case. Each contour line corresponds to a function value between 0 to 1 which are the target values for the net.

5.6.3 Use of variables in the net

The full NN layout used for the analysis proper is 4 layers with 10 variables as inputs in the first layer arranged as follows 10:6:3:1. This layout is chosen in order

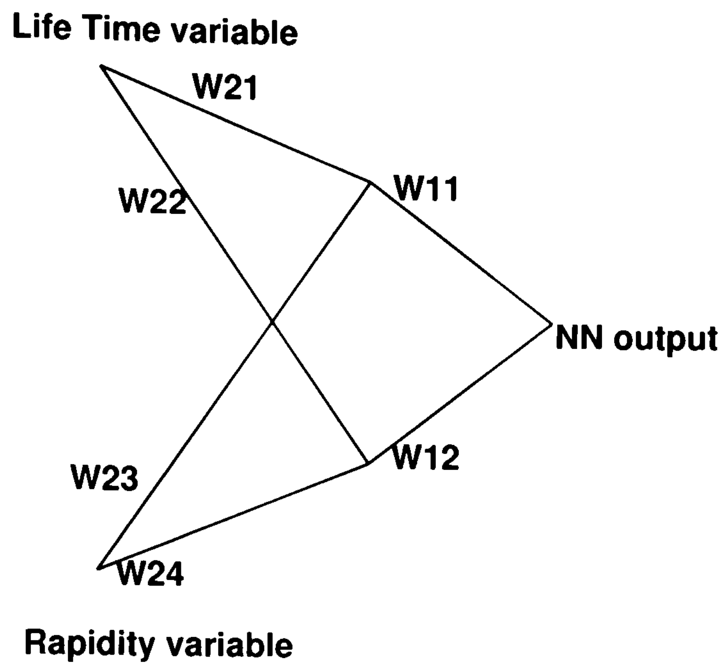

Figure 5.6: The NN layout: 2:2:1 used to illustrate the charm tagging procedure.

to give a smooth distribution in the NN output. The layout is shown in figure 5.10 together with the variables used in the NN. In each event two jets are chosen from those reconstructed in the events according to a jet quality tag. Jets are assigned to one of 3 classes: jets containing a secondary vertex; jets without a secondary vertex but with some tracks with a track probability,P_{tk}, as defined in chapter 3, less than 0.5; the remainder. Jets from the first class are preferred over the other classes. Each variable is scaled to a number between 0 and 1 before it is fed into the NN. The NN output is also constructed to be between 0 and 1. In some events , some of the variables had no values. For example, the mass of the secondary vertex variable is only available in events where a secondary vertex is found. In such cases the variables are entered into the NN with a value of zero. This is done in order to separate these events from the rest of the variables.

The variables used in the NN are:

- The life time variables as presented in chapter 3.

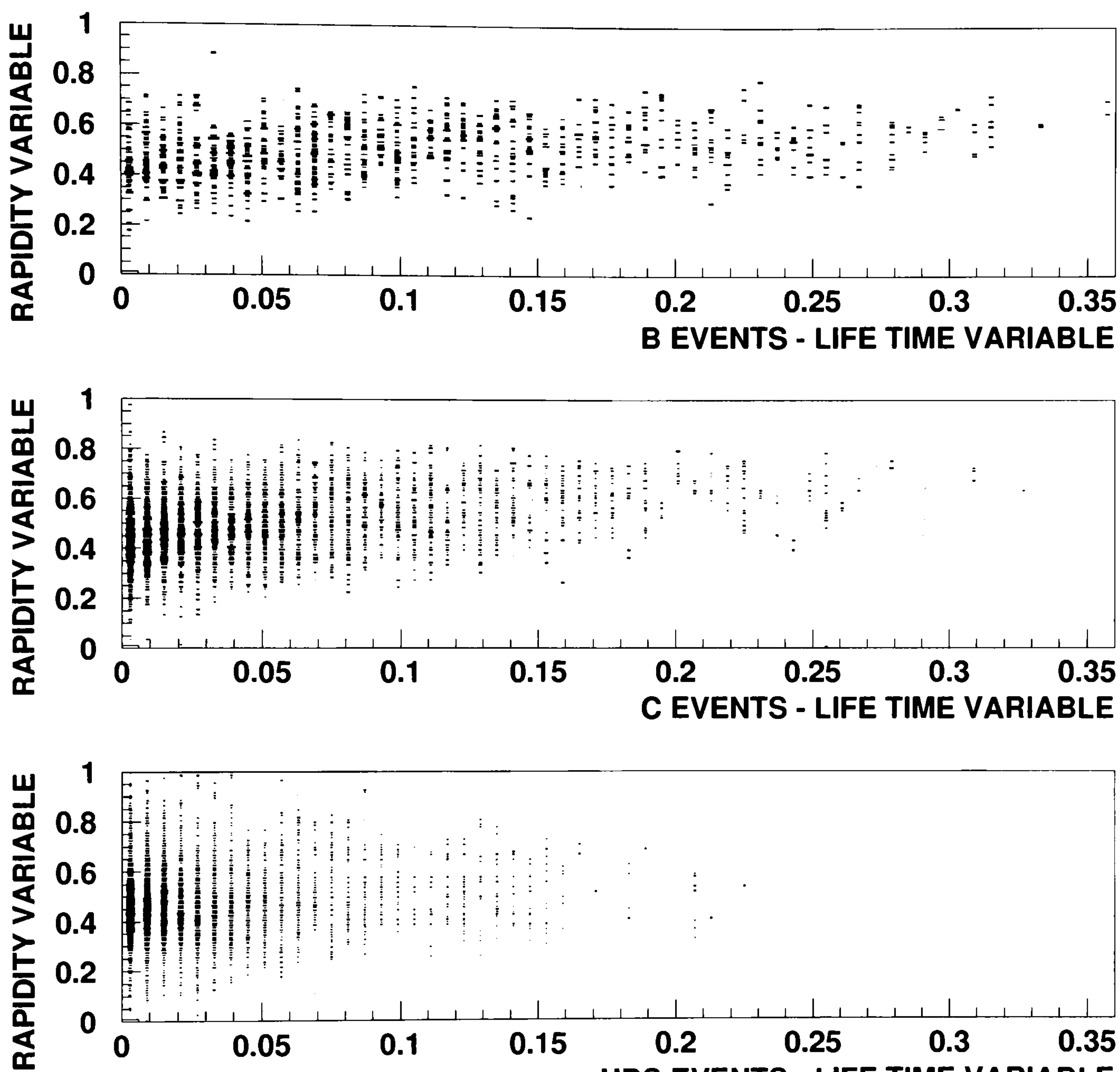

Figure 5.7: The distribution of the life time against rapidity variables for b,c and uds events. It can be seen that the b events are separated by the life time variable. The charm events are best separated in the region around 0.05 in the Life Time variable and 0.7 in the rapidity variable.

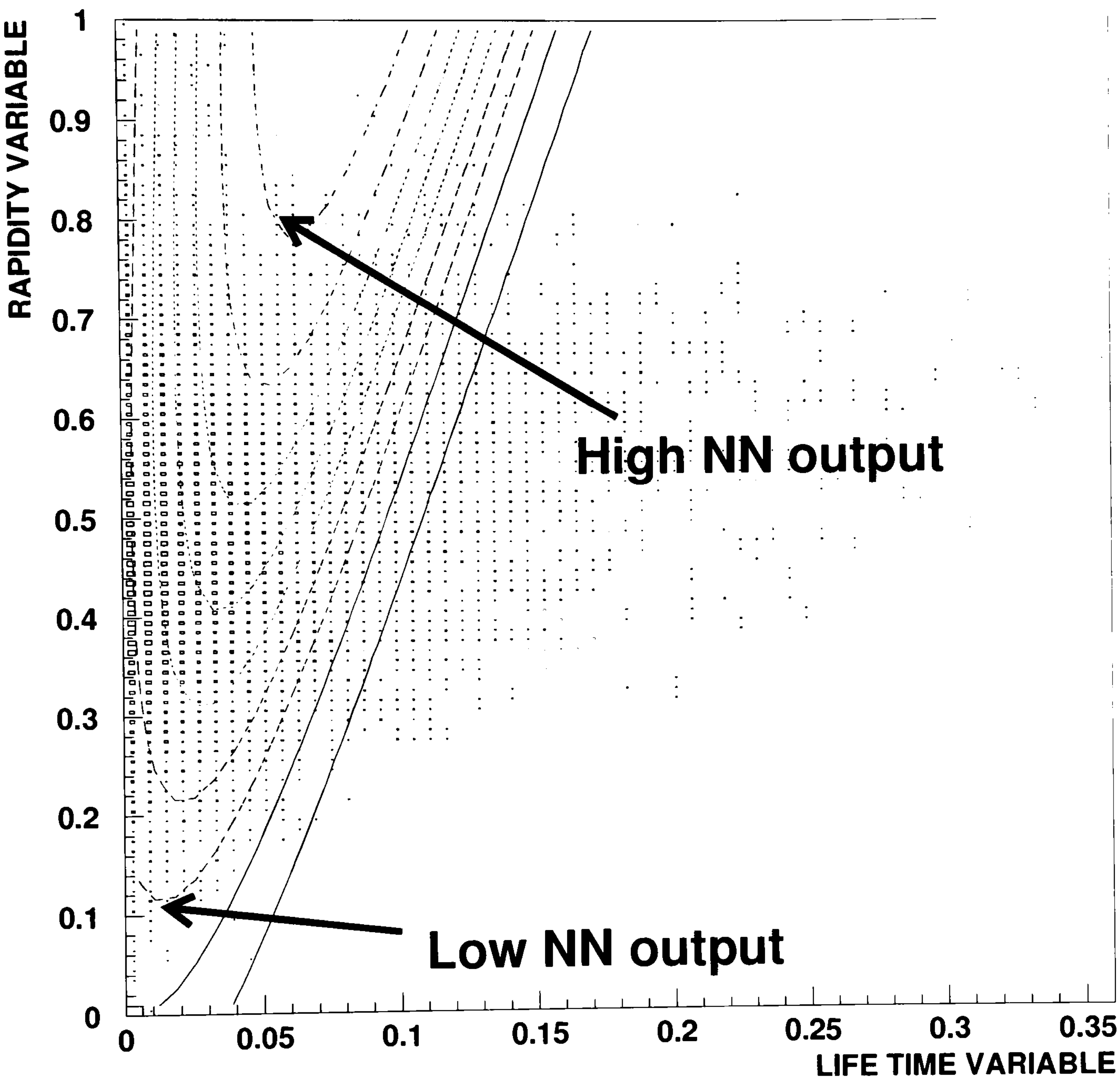

Figure 5.8: The contour line of the function used to optimize the separation in a 2-D case. The points are of c,b and uds events. By referring to figure 5.7 we can see that the c events are best separated in the region around 0.05 in the Life Time variable and 0.7 in the rapidity variable. As can be seen here, the high NN output is in this region.

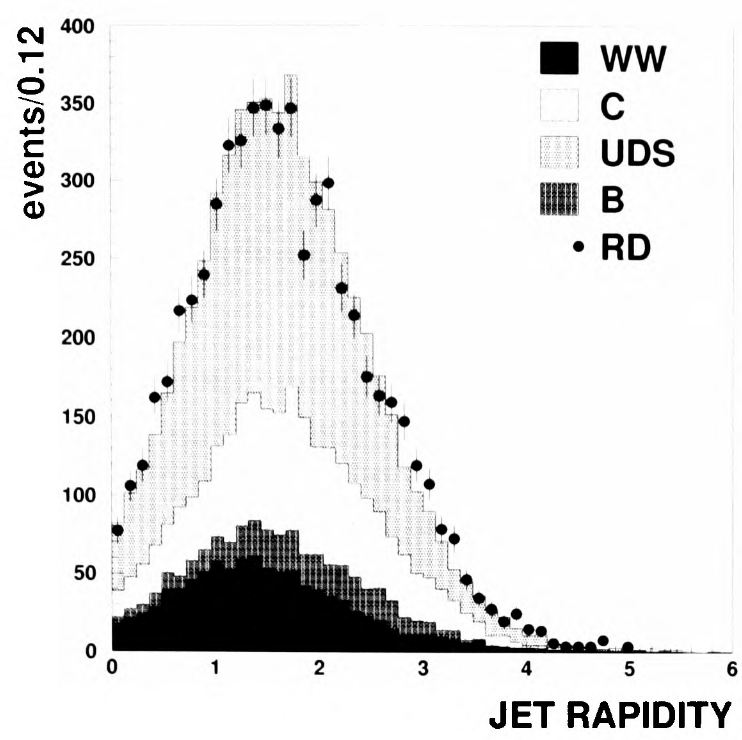

Figure 5.9: The distribution of the jet rapidity variable for 2000 data. These distributions are made after applying the W^+W^- suppression and b veto cuts.

- The jet rapidity variable. This variable is constructed especially for the charm analysis. In this variable, the average of all the tracks rapidities in the jet is taken. The distribution of this variable is shown in 5.9.
- The mass variable as presented in chapter 3.
- The mass cut variable presented in this chapter.
- The event thrust as shown in this chapter. This is done in an effort to help separating the W^+W^- events from c events.
- The number of SV, as presented in this chapter.

For each year two MC samples are used of 15,000 $q\bar{q}$ events each: the training sample, used in training the net, and the testing sample, used for evaluating the trained net's performance.

In order to know the number of cycles needed for optimal training the cost(see apendix A) is plotted as a function of the number of cycles. This is shown in figure 5.11. The value of the cost stabilizes around 140 cycles.

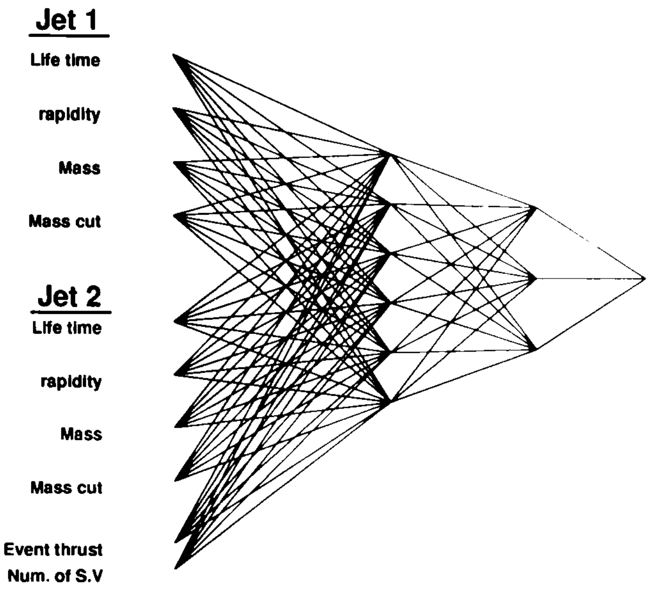

Figure 5.10: The NN layout for c tagging: 10:6:3:1.

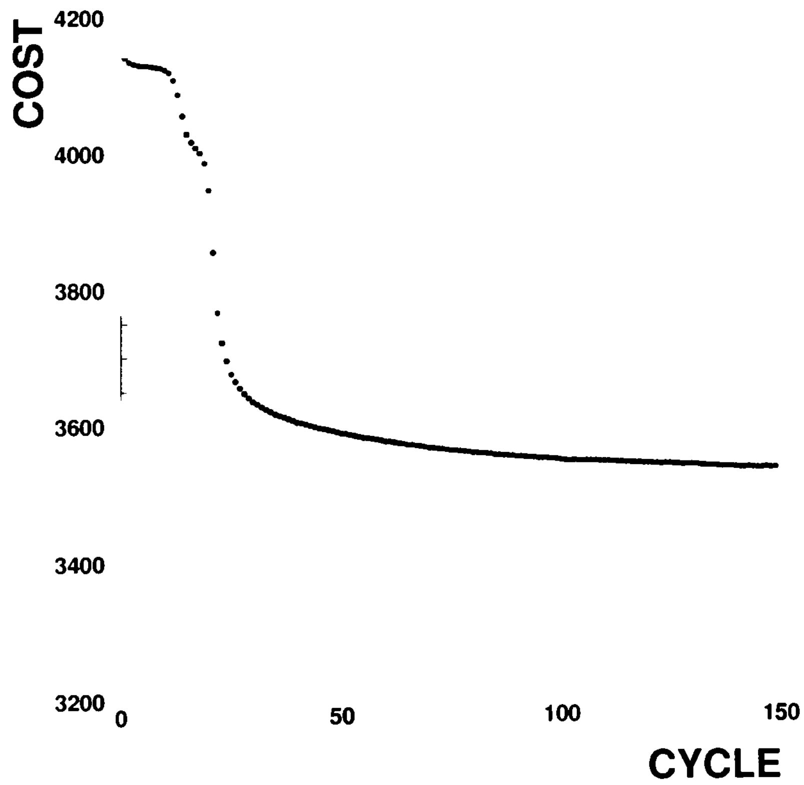

Figure 5.11: The event cost, E, against the number of cycles used in the training.

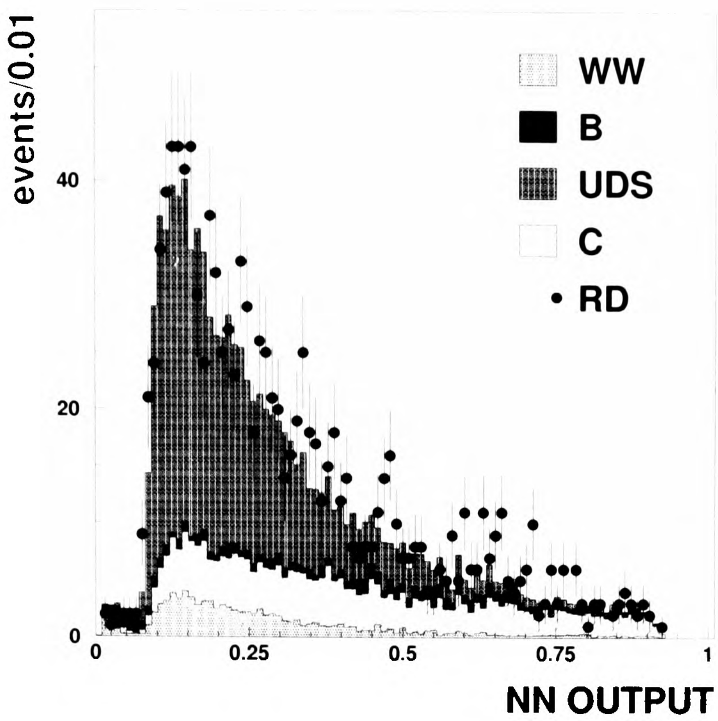

Figure 5.12: The distribution of the c tag NN output for the 1997 data set.

5.7 Performance

The NN output distribution is shown in figure 5.12 - 5.16 for the data sets analyzed. The data and MC agreement is generally reasonable but there are years in which it is less good, such as 2000. Note that there are no events with an output > 0.9. This is due to the fact that there is no region in the variables hyperspace in which there are only c events, and thus the NN can not totally separate the c events from the background. Nevertheless the performance is quite good. Figure 5.17 shows the efficiency-purity curve for the 2000 NN output. One can see that for c purity of 40% the efficiency is 60%. This corresponds to a NN output of 0.25. The efficiency and purity values for all the years at a NN output 0.25 are shown in table 5.4. The performance of the c tagging degrades with energy. For example, in the 1997 data set, for a purity of 40% the efficiency is 67%.

5.8 A^c_{FB} measurement

Now that the data sets have been enhanced in c events the A^c_{FB} values can be measured. The procedure for the A^c_{FB} measurement is identical in principle to that

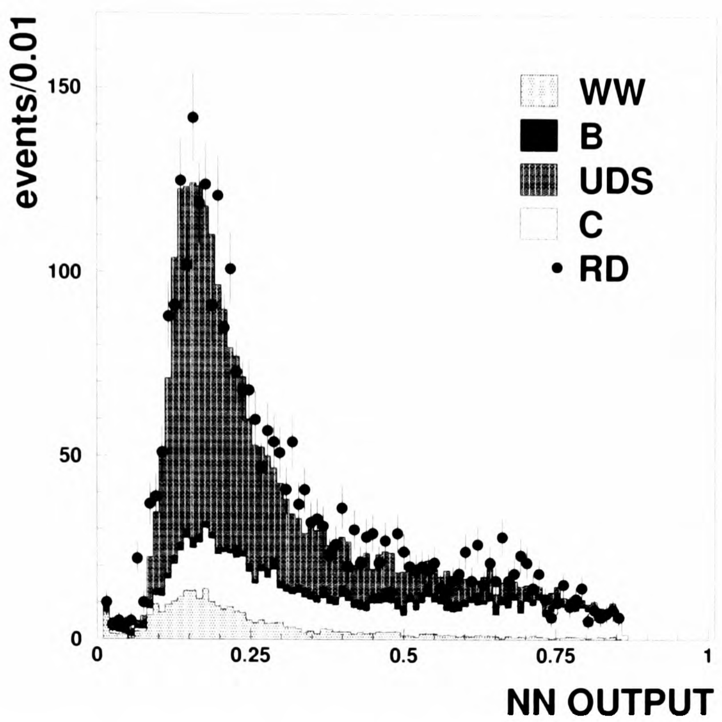

Figure 5.13: The distribution of the c tag NN output for the 1998 data set.

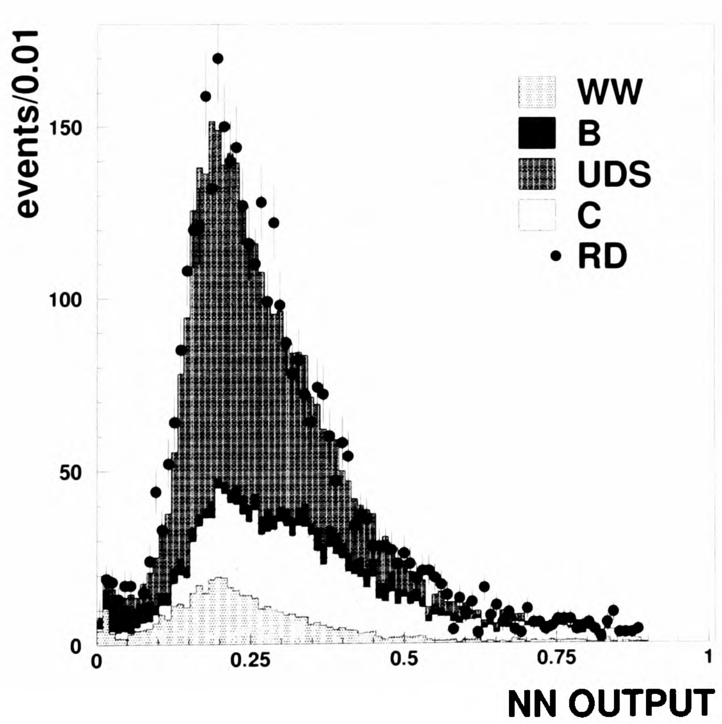

Figure 5.14: The distribution of the c tag NN output for the 1999 data set.

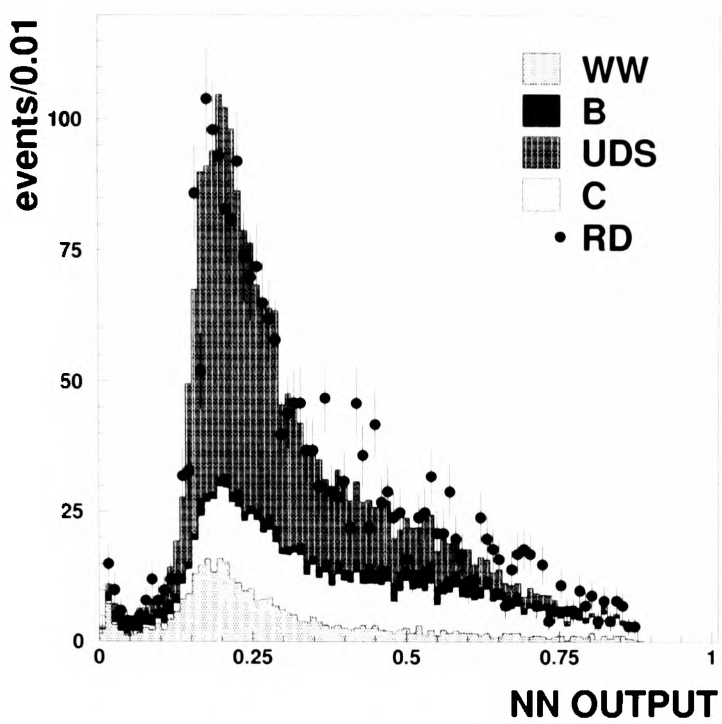

Figure 5.15: The distribution of the c tag NN output for the 2000 good TPC data set.

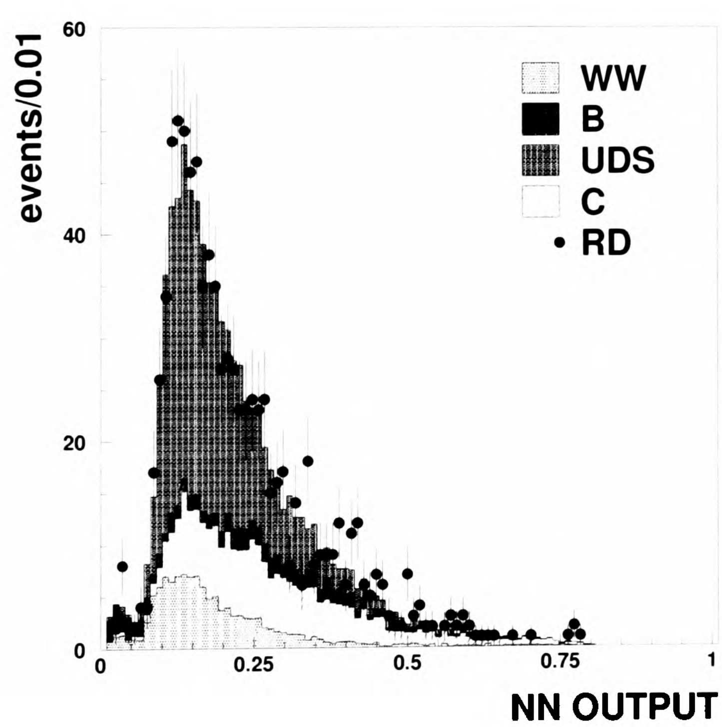

Figure 5.16: The distribution of the c tag NN output for the 2000 bad TPC data set.

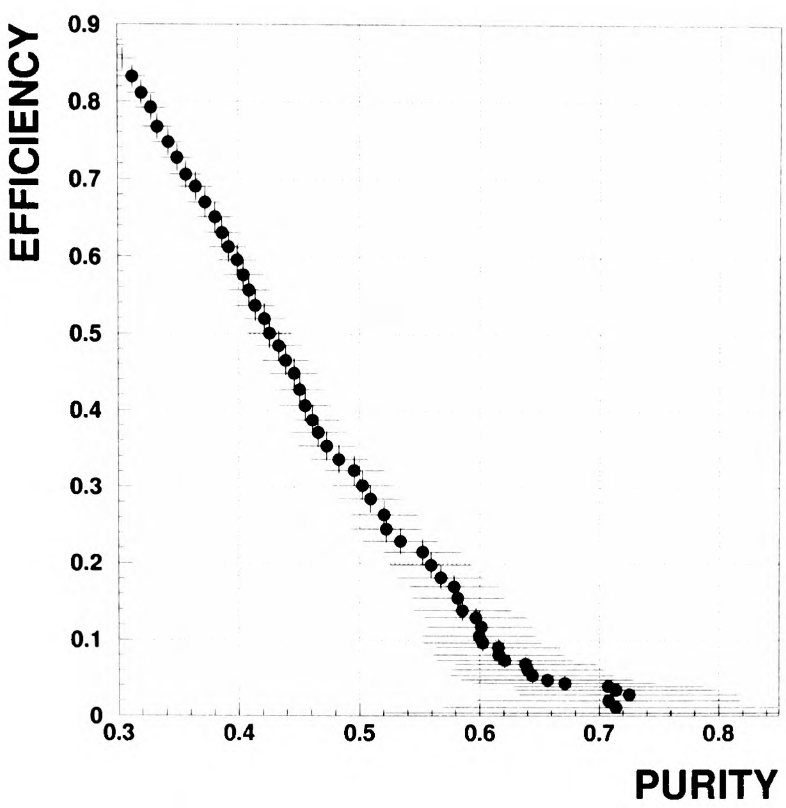

Figure 5.17: The efficiency purity curve for the c tag NN output in 2000.

described in chapter 4 for the b case. All the information about other flavours than the c was obtained from the MC. As in the b case the measurement was performed in 4 bins of Q_{FB}. The distributions of $Q_F - Q_B$ and $Q_F + Q_B$ for all the years are shown in figures 5.18-5.23. $c\bar{c}$ production is expected to have a positive asymmetry, however it is not possible to observe a tendency towards positive values in the $Q_F - Q_B$ data distributions as the sample is only 40% pure. In the $Q_F + Q_B$ distributions one can observe a mean value which is 0.0087 ± 0.0031 for the combined data set, therefore consistent with 0 at the 2 sigma level. Table 5.3 show the c dilution and the measured $AD^q_{mes} = D_q \cdot A^q_{FB(s')}$ of the backgrounds applied in the correction procedure for all the data analyzed. The contamination from events with lower $\sqrt{S'}$ which survived the selection was accounted for in the fit in the same way as in the b case.

The choice of the best place to make a cut on the NN output was studied against the A^c_{FB} statistical error . Figure 5.24 shows the A^c_{FB} statistical error against the NN output for all years combined. This curve indicates that the best place to measure is at a NN output cut of 0.25. In order to check that this conclusion remains valid additional checks were performed. The value of the background corrections of the

W^+W^- and uds events was varied by 50% and 10% respectively and the b fraction by 10%. The results of these changes on the measurement error are shown in table 5.5 for the points of interest around the minimum error values. From this it is clear that 0.25 is indeed the optimum working place.

The c efficiency and purity values for NN cut of 0.25 for all years are shown in table 5.4. The changes in the efficiency-purity working point throughout the years demonstrate the degradation in the c tagging performance with energy discussed in the performance section.

The choice of the κ value was determined from a study of the variation in A^c_{FB} statistical error obtained from real data. Figure 5.25 shows the A^c_{FB} statistical error of all data combined against the value of κ. This curve shows that the optimum place to make the measurement is at $\kappa = 0.2$. This κ value is significantly lower than the one used in the b case($\kappa = 0.5$). This can be explained by the different fragmentation properties of c and b quarks. As shown in figure 1.11 the c hadron is on average considerably less energetic than the b hadron. This makes the momentum of the tracks coming from the c hadron much closer in value to the rest of the tracks in the event than in the b case. Therefore, the significance of the c hadron track's momentum as a discriminating variable decreases with respect to the b case. This is reflected in the lower κ value which reduces the dependence of the jet charge on the momentum of the track's and increases the significant of the charge of each track.

5.9 Results

The asymmetry values obtained for the different energies are presented in table 5.6. The asymmetry values for 2000 data split into the TPC bad and TPC good periods are presented in table 5.7. The good agreement indicates no incompatibility between the two periods. Therefore the two results may be combined.

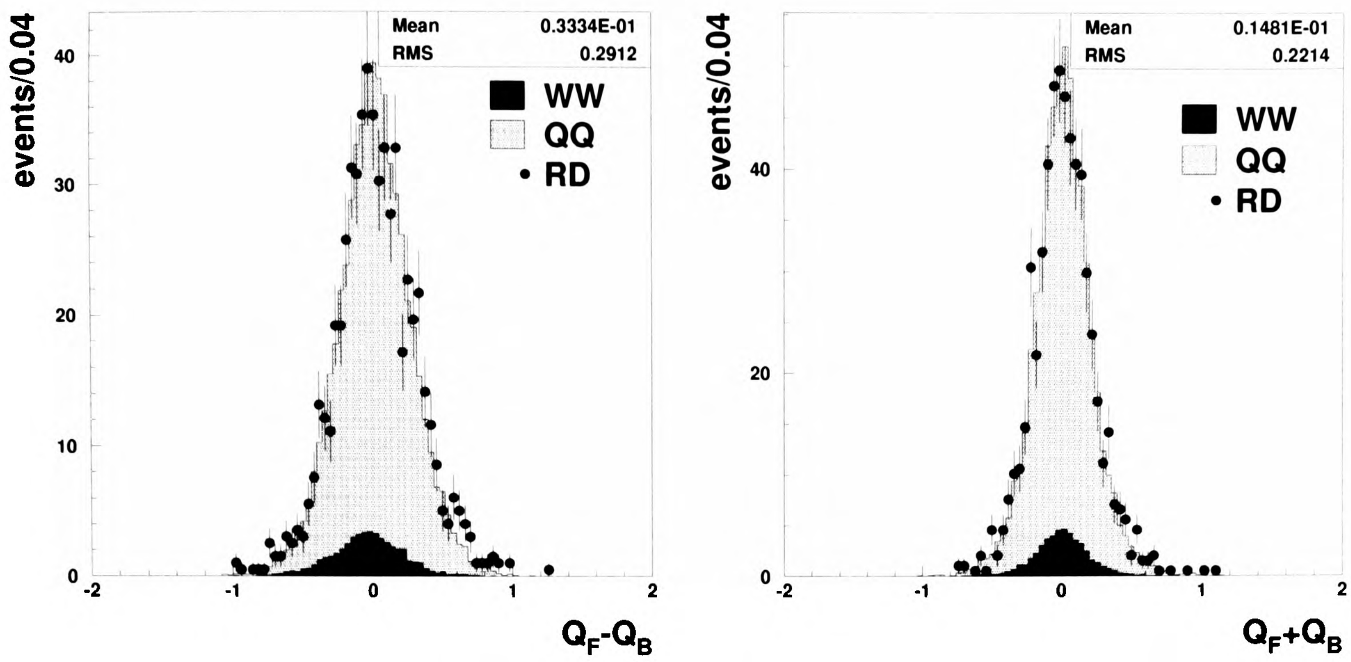

Figure 5.18: Left:Distribution of the $Q_F - Q_B$. Right: Distribution of the $Q_F + Q_B$. This is for the 1997 data and after the c tag was performed.

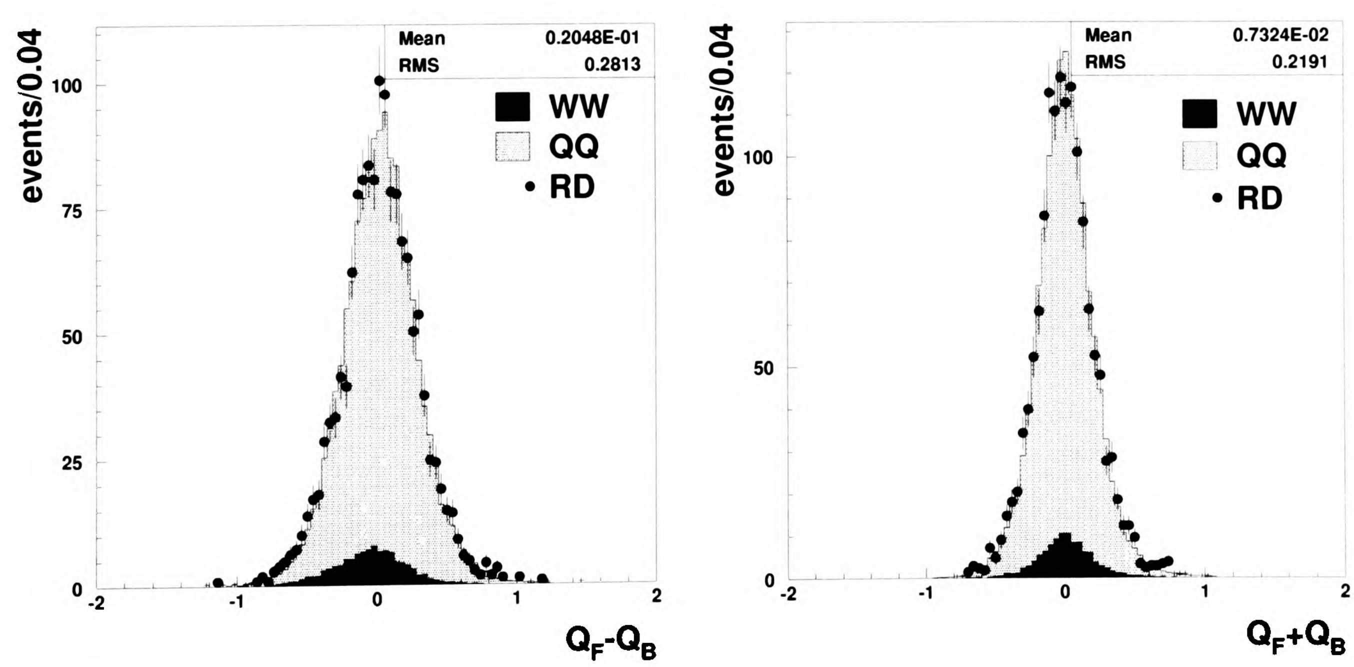

Figure 5.19: Left:Distribution of the $Q_F - Q_B$. Right: Distribution of the $Q_F + Q_B$. This is for the 1998 data and after the c tag was performed.

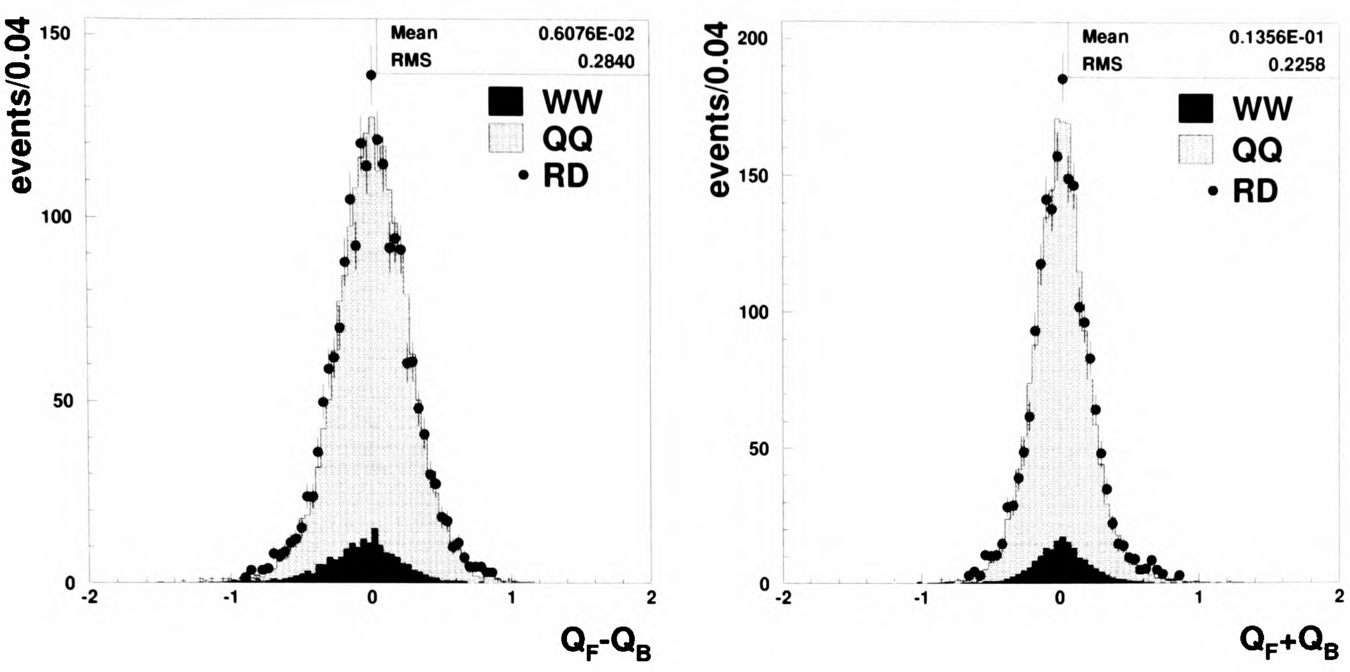

Figure 5.20: Left:Distribution of the $Q_F - Q_B$. Right: Distribution of the $Q_F + Q_B$. This is for the 1999 data and after the c tag was performed.

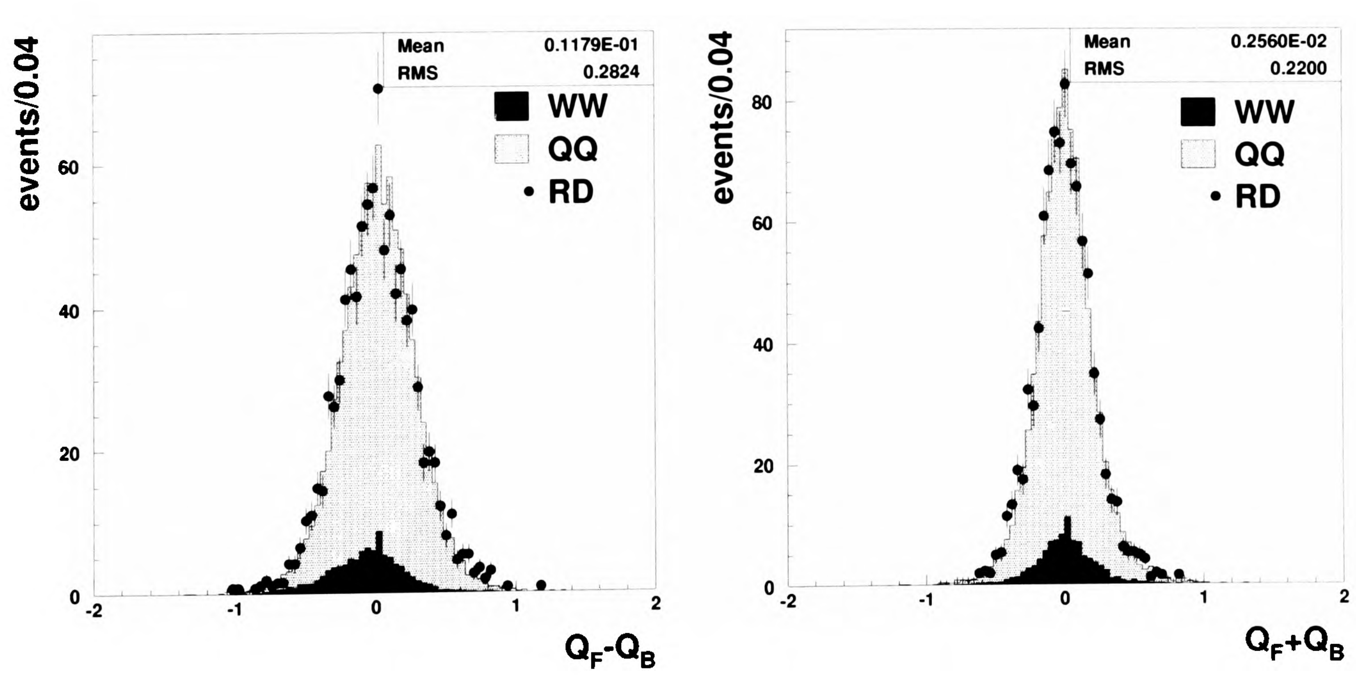

Figure 5.21: Left:Distribution of the $Q_F - Q_B$. Right: Distribution of the $Q_F + Q_B$. This is for the 2000 TPC good data and after the c tag was performed.

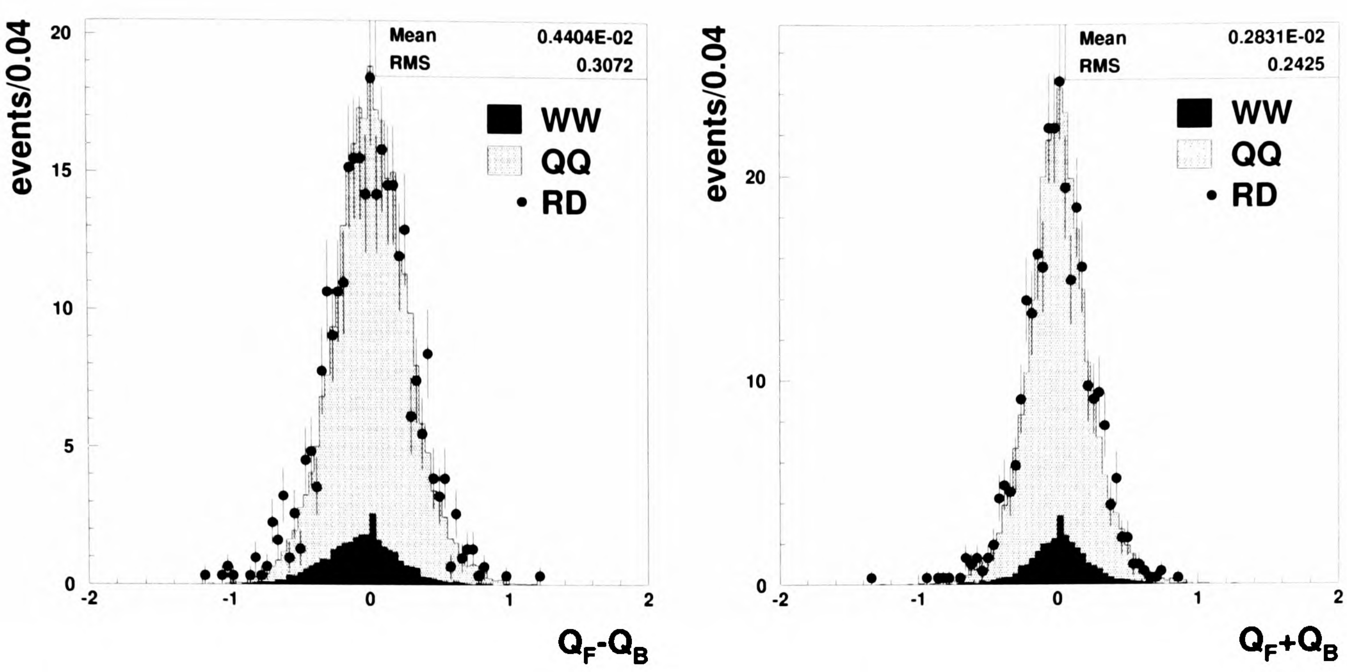

Figure 5.22: Left:Distribution of the $Q_F - Q_B$. Right: Distribution of the $Q_F + Q_B$. This is for the 2000 TPC bad data and after the c tag was performed.

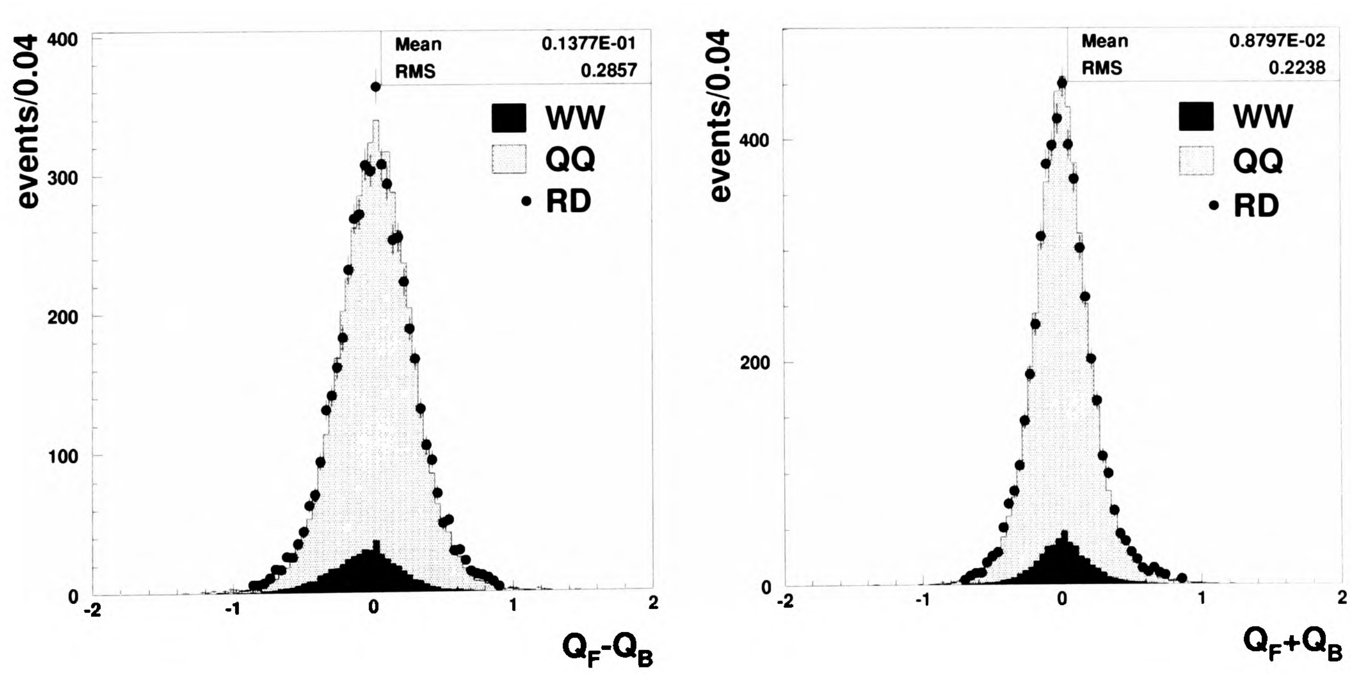

Figure 5.23: Left:Distribution of the of $Q_F - Q_B$. Right: Distribution of the $Q_F + Q_B$. This is for all data combined.

1997 data				
	c Dilution	AD^{b}_{FB}	AD^{uds}_{FB}	AD^{WW}_{FB}
$0.000 < \|Q_{FB}\| < 0.072$	0.112	0.059	0.033	0.077
$0.072 < \|Q_{FB}\| < 0.158$	0.314	0.003	-0.070	0.128
$0.158 < \|Q_{FB}\| < 0.280$	0.421	0.115	-0.095	0.052
$0.280 < \|Q_{FB}\| < 2.000$	0.650	0.150	-0.087	0.244
$0.000 < \|Q_{FB}\| < 2.000$	0.430	0.081	-0.054	0.125
1998 data				
	c Dilution	AD^{b}_{FB}	AD^{uds}_{FB}	AD^{WW}_{FB}
$0.000 < \|Q_{FB}\| < 0.075$	0.116	0.012	-0.040	0.073
$0.075 < \|Q_{FB}\| < 0.160$	0.328	0.075	0.006	-0.042
$0.160 < \|Q_{FB}\| < 0.280$	0.450	0.082	-0.026	0.146
$0.280 < \|Q_{FB}\| < 2.000$	0.687	0.095	-0.089	0.232
$0.000 < \|Q_{FB}\| < 2.000$	0.458	0.066	-0.037	0.102
1999 data				
	c Dilution	AD^{b}_{FB}	AD^{uds}_{FB}	AD^{WW}_{FB}
$0.000 < \|Q_{FB}\| < 0.073$	0.092	0.030	0.019	0.072
$0.073 < \|Q_{FB}\| < 0.164$	0.311	0.118	-0.003	0.127
$0.164 < \|Q_{FB}\| < 0.282$	0.354	0.049	-0.016	0.110
$0.282 < \|Q_{FB}\| < 2.000$	0.601	0.180	-0.096	0.319
$0.000 < \|Q_{FB}\| < 2.000$	0.395	0.094	-0.024	0.155
2000 TPC good data				
	c Dilution	AD^{b}_{FB}	AD^{uds}_{FB}	AD^{WW}_{FB}
$0.000 < \|Q_{FB}\| < 0.078$	0.090	0.022	0.011	0.114
$0.078 < \|Q_{FB}\| < 0.165$	0.250	0.033	-0.004	0.091
$0.165 < \|Q_{FB}\| < 0.283$	0.330	0.081	-0.091	0.072
$0.283 < \|Q_{FB}\| < 2.000$	0.610	0.115	-0.087	0.270
$0.000 < \|Q_{FB}\| < 2.000$	0.389	0.062	-0.042	0.136
2000 TPC bad data				
	c Dilution	AD^{b}_{FB}	AD^{uds}_{FB}	AD^{WW}_{FB}
$0.000 < \|Q_{FB}\| < 0.076$	0.112	0.010	-0.068	-0.044
$0.076 < \|Q_{FB}\| < 0.164$	0.272	0.019	-0.034	0.171
$0.164 < \|Q_{FB}\| < 0.282$	0.301	0.041	-0.045	0.223
$0.282 < \|Q_{FB}\| < 2.000$	0.584	0.029	-0.135	0.214
$0.000 < \|Q_{FB}\| < 2.000$	0.371	0.024	-0.070	0.139

Table 5.3: Measurement corrections for 1997-2000 data sets.

	c efficiency	c fraction	uds fraction	b fraction	W^+W^- fraction
97	0.691 ± 0.007	0.371 ± 0.005	0.450 ± 0.005	0.089 ± 0.003	0.082 ± 0.003
98	0.672 ± 0.007	0.391 ± 0.006	0.438 ± 0.005	0.094 ± 0.003	0.075 ± 0.003
99	0.674 ± 0.007	0.351 ± 0.005	0.473 ± 0.005	0.082 ± 0.003	0.092 ± 0.003
00(G)	0.609 ± 0.008	0.394 ± 0.006	0.393 ± 0.006	0.110 ± 0.004	0.089 ± 0.003
00(B)	0.576 ± 0.008	0.401 ± 0.006	0.373 ± 0.006	0.121 ± 0.004	0.090 ± 0.007

Table 5.4: The c efficiency and signal and background fractions for 1997-2000 data sets. (G) and (B) refer to the good and bad TPC periods.

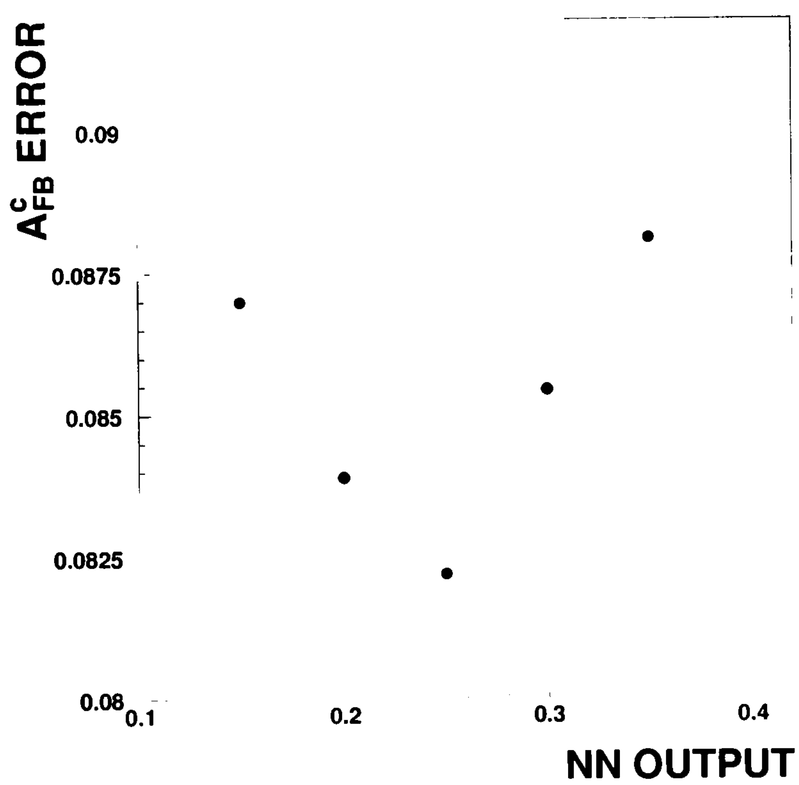

Figure 5.24: The A^c_{FB} statistical error against the NN output evaluated from real data for all years combined.

NN cut	0.2	0.25	0.3
stat. error	0.0839	0.0822	0.0854
syst. error	0.0555	0.0553	0.0524
combined error	0.1005	0.0990	0.1002

Table 5.5: c tag working point study for all data combined.

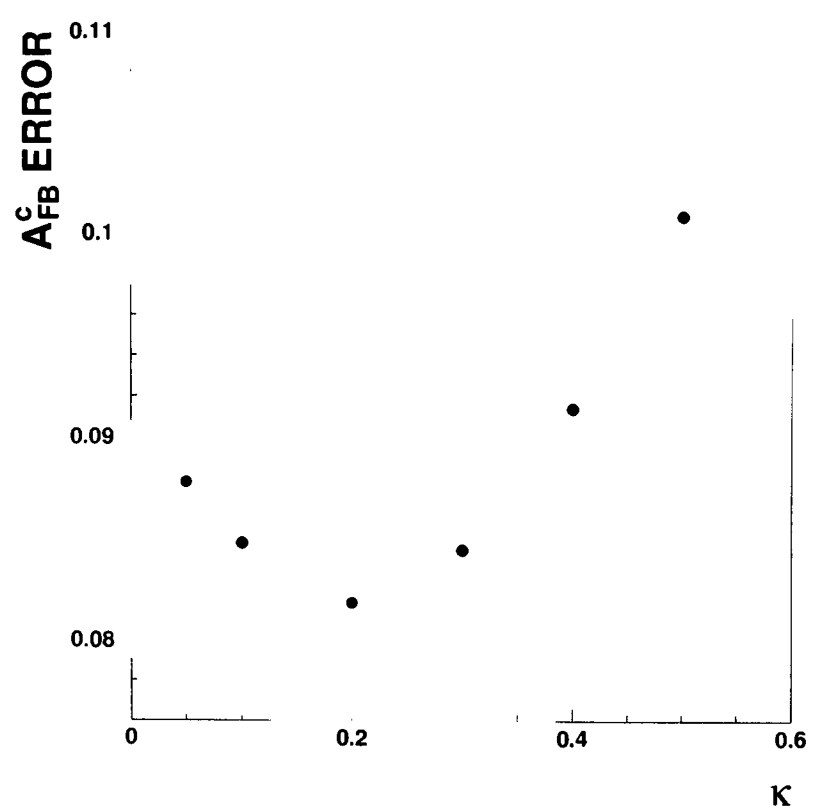

Figure 5.25: The A^c_{FB} statistical error against the κ value used evaluated from real data combining all data sets.

Energy (GeV)	number of selected events	A^c_{FB} ± stat ± syst
183	582	0.800 ± 0.230 ± 0.156
188.6	1413	0.494 ± 0.156 ± 0.096
197.5	1934	0.541 ± 0.139 ± 0.141
205.5	1218	0.511 ± 0.164 ± 0.116

Table 5.6: A^c_{FB} results for 1997-2000 data sets.

5.10 Systematic study

The systematic errors considered are the c dilution factor and the uncertainty on the background corrections made in the measurement. The knowledge of the background is especially important in this analysis as the measurement is made at a low purity working point which makes the result very sensitive to uncertainty in the background value which means relying heavily on MC. The data and MC agreement of the NN output for the 1999 data set shown in figure 5.14 is good; however for the other years it is less good as can be seen in particular in figure 5.15 for the 2000 data set.

Energy (GeV)	number of selected events	$A_{FB}^c \pm$ stat
205.5 TPC (G)	930	0.484 ± 0.178
205.5 TPC (B)	288	0.678 ± 0.339

Table 5.7: A_{FB}^c results for 2000 data. (G) and (B) refer to the good and bad TPC periods.

This discrepancy motivates a conservative error assignment.

5.10.1 Dilution systematics

The dilution systematic is evaluated in the same way as in the b case. The data and the MC distribution of the $Q_F + Q_B$ variable are made to agree exactly by varying the MC κ parameter. From the change in the κ parameter we calculate the change in the dilution factor which provides the dilution systematics. Figure 5.23 shows the $Q_F + Q_B$ variable for data and MC for $\kappa = 0.2$. Figure 5.27 shows the $Q_F + Q_B$ variable where in the data $\kappa = 0.2$. and in the MC $\kappa = 0.25$. The data RMS value is 0.223. The MC RMS values before and after the κ change are 0.214 and 0.223 respectively. This corresponds to a 1% change in the c dilution factor. This procedure gives a lower variation on the dilution than in the b case(3%) because of the lower dependence of the jet charge on the momentum.

For this reason, and because of the reduced significance of the dilution uncertainty in this analysis, no explicit systematic has been evaluated to cover the differences between data and MC as a function of momentum. The c dilution is also varied by its statistical error from the MC sample.

5.10.2 Background systematics

The background is varied substantially to estimate the sensitivity of the measurement to errors in the purity estimation. For each change in the background the total number of expected MC and data events are compared to check that the magnitude of the change was reasonable. The differences in the data and expected MC events

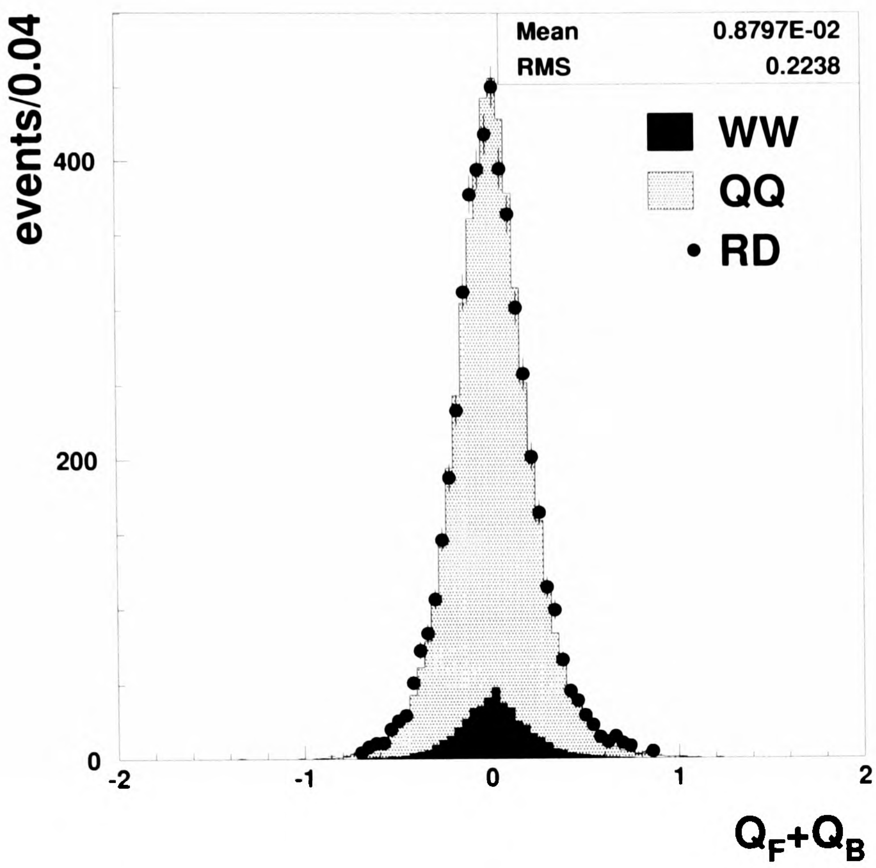

Figure 5.26: The distribution of $Q_F + Q_B$ variable for all the data combined.

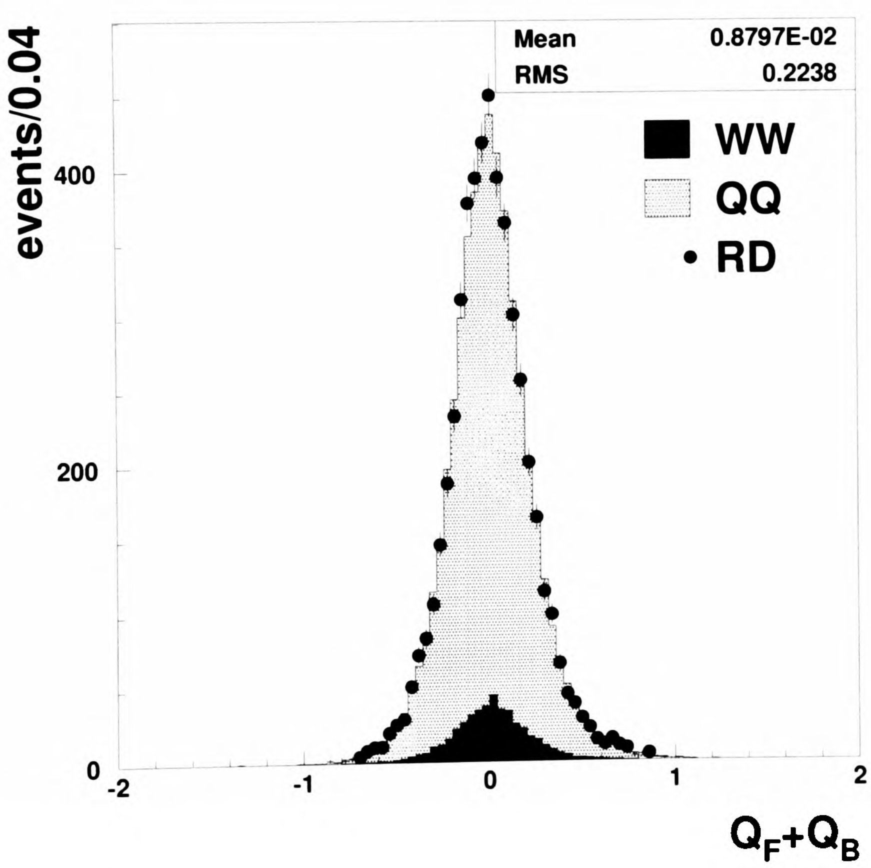

Figure 5.27: The distribution of $Q_F + Q_B$ variable with MC κ parameter varied to optimally fit the data distribution. This distribution is for all data combined.

after the considered background changes are at the 2 sigma level.

The background variation was:

- b fraction: the b fraction is varied by 50%.
- uds fraction: the uds fraction is varied by 10%.
- W^+W^- fraction: the W^+W^- fraction is varied by 50%.

In addition, the c fraction itself is varied by 10%. The changes made to both signal and all backgrounds are unlikely to occur in the data simultaneously but they are done as an extra precaution for a measurement made in a low signal working point. Table 5.8 shows the systematics for all the data analyzed.

E_{cm} GeV	183	189	198	206
dilution (κ)	0.007	0.004	0.005	0.005
dilution stat	0.026	0.014	0.018	0.020
b fraction	0.073	0.030	0.033	0.063
c fraction	0.056	0.038	0.044	0.032
uds fraction	0.067	0.044	0.061	0.028
W^+W^- fraction	0.101	0.067	0.112	0.084
S_f correction	0.024	0.016	0.016	0.017
Total	0.156	0.096	0.141	0.116

Table 5.8: systematics results for all years.

5.10.3 Summary

All systematics are shown in table 5.8. It can be seen that those associated with the background uncertainties are dominant. Because these errors are large, no attempt has been made to evaluate other uncertainties, such as those associated with the physics modeling which were considered in the b case. Further to that experience with the b analysis showed these uncertainties to be small. The errors have been combined assuming them to be independent. The total systematic error is similar in magnitude to the statistical, as is clear from table 5.6.

6. Interpretation and Conclusions

6.1 Introduction

This chapter compares the measurements A^b_{FB} and A^c_{FB} with the Standard Model predictions. The asymmetry results are also used to put limits on physics beyond the Standard Model in the form of Contact Interactions. Finally, consideration is given to how the measurement could be improved.

6.2 A^b_{FB} comparison with the SM

The A^b_{FB} results and the Standard Model predictions are shown in table 6.1 and in figure 6.1. The SM values come from the ZFITTER[26] program.

Energy (GeV)	A^b_{FB} $\pm$ error	SM expectation
183	-0.053 $\pm$ 0.213	0.542
188.6	0.690 $\pm$ 0.179	0.547
191.6	0.232 $\pm$ 0.277	0.548
195.5	0.711 $\pm$ 0.169	0.551
199.5	0.516 $\pm$ 0.161	0.553
201.6	0.630 $\pm$ 0.226	0.554
204.8	0.752 $\pm$ 0.259	0.555
206.6	0.138 $\pm$ 0.200	0.556

Table 6.1: A^b_{FB} results SM expectation.

The results are all in the allowed physical range with a positive value as expected from the SM. An exception is provided by the 183 GeV measurement which has a small negative value and lies 2.5 σ below the expectation. A combination was made, in which the energy dependence was assumed to follow that predicted by the SM and the difference between prediction and measurement was averaged over all

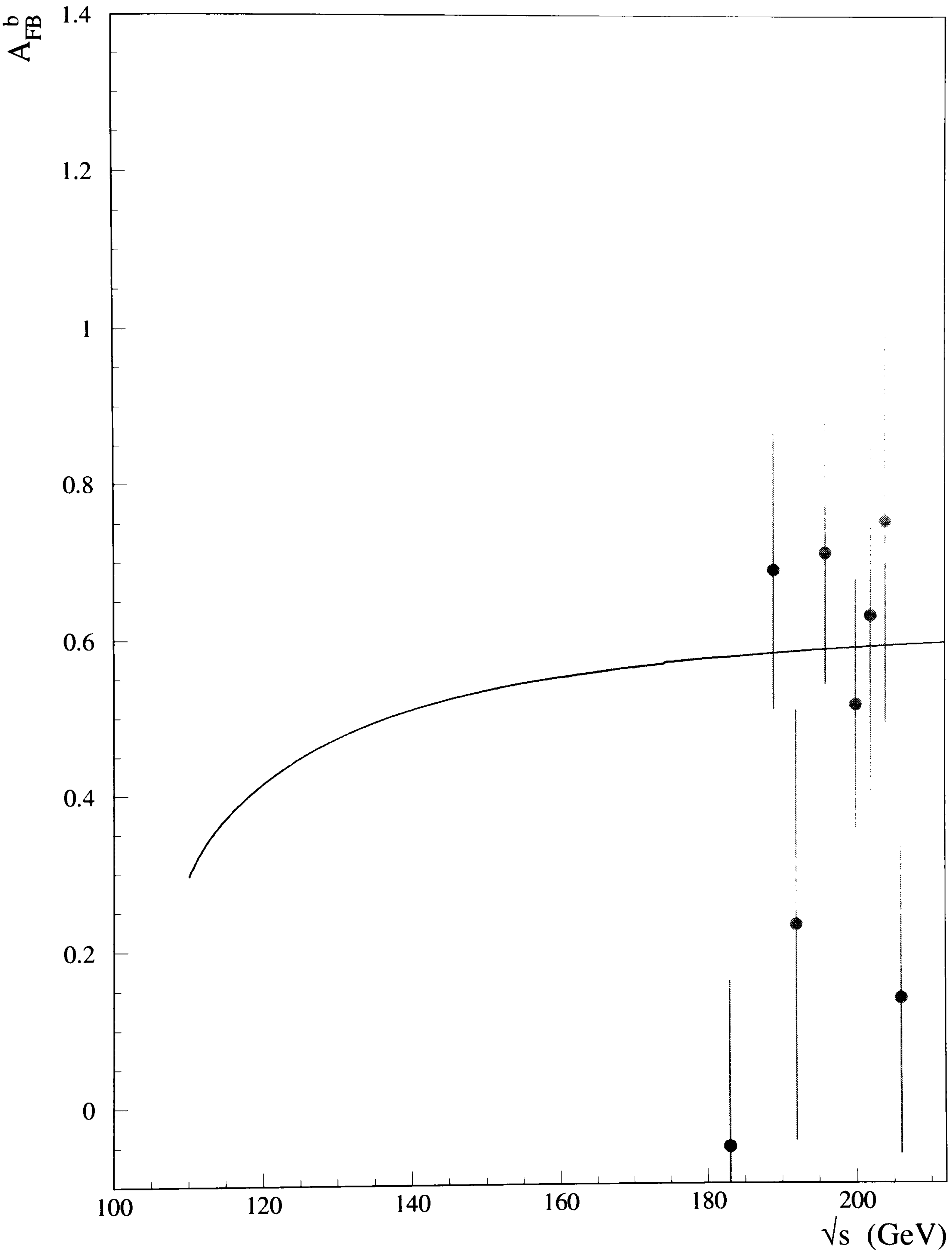

Figure 6.1: Results of A^b_{FB} for the different energy points. The theoretical prediction curve comes from the ZFITTER[26] program.

energies. This combination was performed with a χ^2 fit. The parameter fitted was the difference between the A^b_{FB} measurement and the predicted SM values shown in table 6.1. Some of the errors were known to be correlated between the years, whereas others were independent. This was accounted in the fit by building up a full covariance matrix. The uncorrelated component of the error included the statistical error on the dilution and the b purity knowledge cross-checked each year on the data. The rest of the systematic errors were assumed to be correlated. The fit output is the average offset in the A^b_{FB} value (ΔA^b_{FB}) between the measured values and the SM predictions:

$$\Delta A^b_{FB} = -0.089 \pm 0.076.$$

The ΔA^b_{FB} value is compatible with a zero deviation from the SM at a mean collision energy of 196.6 GeV. The χ^2 of this combination is 14.4 for 7 degrees of freedom. The quality of the χ^2 result is degraded by the low asymmetry values measured at 183 and 206.6 GeV.

6.3 A^c_{FB} comparison with the SM

The A^c_{FB} results and the Standard Model prediction are shown in table 6.2 and in figure 6.2. The SM values come from the ZFITTER[26] program.

Energy (GeV)	$A^c_{FB} \pm$ error	SM expectation
183	0.800 $\pm$ 0.277	0.653
188.6	0.494 $\pm$ 0.182	0.650
197.5	0.541 $\pm$ 0.198	0.645
205.5	0.511 $\pm$ 0.201	0.640

Table 6.2: A^c_{FB} results and SM expectation .

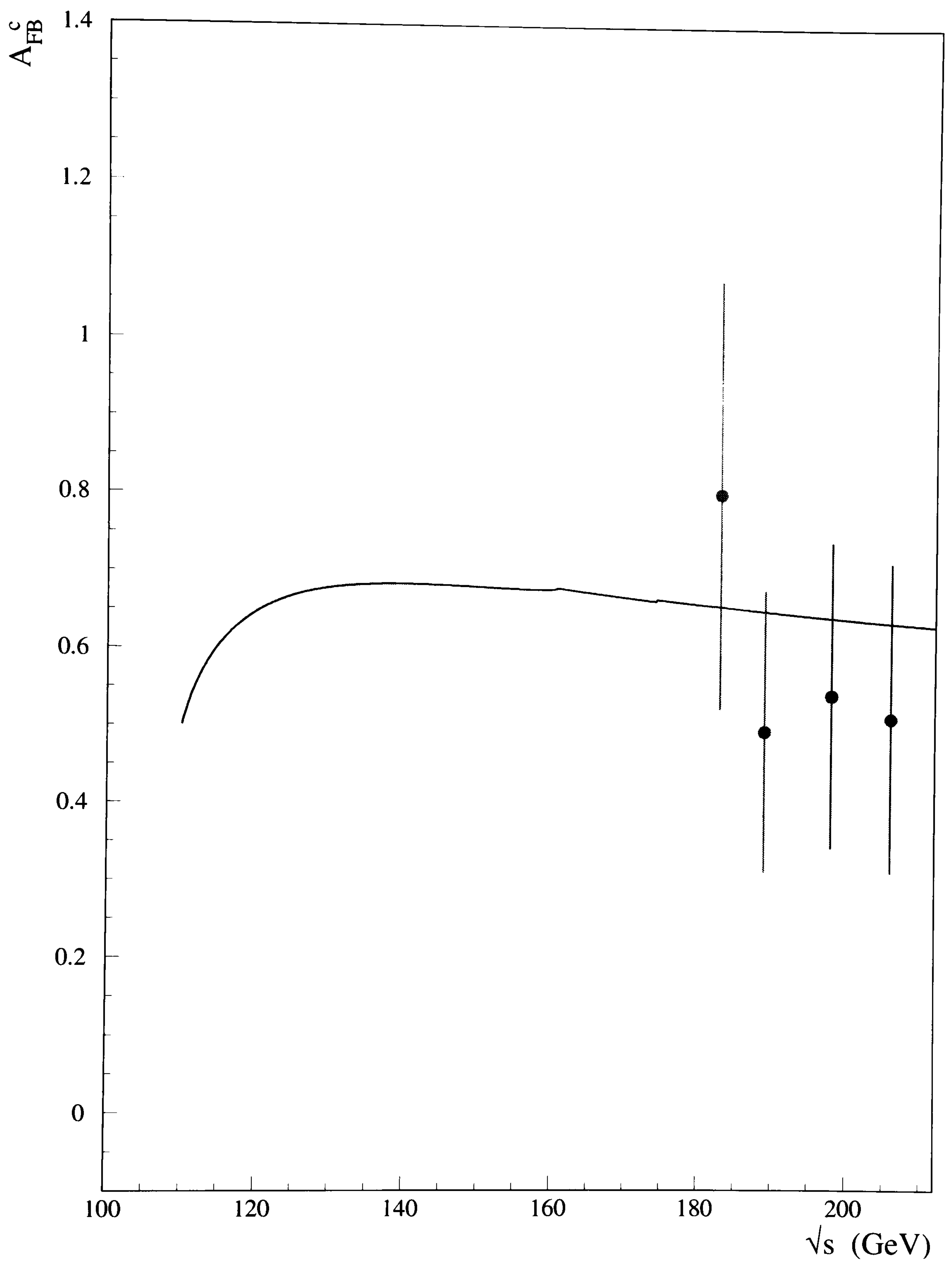

Figure 6.2: Results of A^c_{FB} for the different energy points. The theoretical prediction curve comes from the ZFITTER[26] program.

The measurement are all in the physical range, and individually consistent with expectations. As in the b case, a χ^2 fit was made to evaluate, ΔA^c_{FB}, the average deviation from the SM predictions using the 4 A^c_{FB} measurements presented in table 6.2. The same assumptions were made regarding the correlated and uncorrelated errors. The fit output is:

$$\Delta A^c_{FB} = -0.116 \pm 0.143.$$

This value is consistent with a zero deviation from the SM at a mean collision energy of 196.6 GeV. The χ^2 of this combination is 1.2 for 3 degrees of freedom.

6.4 Contact interaction fits

As explained in chapter 1, new physics can be introduced in 8 contact interaction models. These are fitted to the data in this section. The method of fitting works by calculating the theoretical value of the cross section or asymmetry from expression 1.27 and evaluating the χ^2 to the data. The theoretical values depend on the ϵ parameter as can be seen in expression 1.27, and the ϵ value is obtained from a likelihood curve made up from these χ^2 values as explained in Appendix A. The ϵ parameter can take both positive and negative values in the fit and is 0 in the limit that no contact interaction exist. In order to increase the sensitivity, DELPHI R_b measurements were also included in the fit together with the A^b_{FB} and A^c_{FB} results. These measurements were made at the same energy points as the asymmetries and were taken from [30]. The R_b values used are given in table 6.3. The fit includes the correlated systematics between the measurements at the different energy points.

The results of ϵ for each of the models are shown in table 6.4 together with their 68% Confidence Level(CL) uncertainty. They are all compatible with the SM expectation of $\epsilon = 0$. Details on how these uncertainties were obtained can be found in Appendix A.

Energy (GeV)	R_b ± error
182.25	0.137 ± 0.015
188.3	0.156 ± 0.011
191.6	0.168 ± 0.026
195.5	0.165 ± 0.015
199.5	0.183 ± 0.016
201.64	0.177 ± 0.023
204.8	0.166 ± 0.019
206.6	0.156 ± 0.015

Table 6.3: DELPHI R_b results for different energies[30].

As can be seen in table 6.4 the ± uncertainties on ϵ can be different in size since the shape of the likelihood curve can be asymmetric. The uncertainties on ϵ are lower on the VV, AA and V0 models. This is consisted with results published in [39]. The results for positive and negative interference with the SM(i.e the sign of the η_{ij} parameters) are equivalent under the transformation of $\epsilon \rightarrow -\epsilon$. Therefore it is sufficient to fit only for the case of positive interference but to allow ϵ to take both positive and negative values. The limits on the energy scale(Λ) are obtained by assuming $\epsilon \rightarrow -\epsilon$ for Λ^- and $\epsilon \rightarrow +\epsilon$ for Λ^+. This corresponds respectively to a destructive and constructive interference with the SM. 95% Contact Interaction(CI) limits on Λ are shown in table 6.4 and are illustrated graphically in figure 6.3. More details regarding the calculation of these limits can be found in Appendix A. The CI limits presented in table 6.4 are compatible with limits obtained by other processes such as $e^+e^- \rightarrow l\bar{l}$ presented in [39].

The fit results, in most of the models, are more sensitive to the R_b numbers than to the A^b_{FB} and A^c_{FB} measurements. This was checked by making the fit separately using the R_b, A^b_{FB} and A^c_{FB} measurements as can be seen from tables 6.5-6.7. The fit results using only the A^b_{FB} and A^c_{FB} measurements is shown in table 6.8. Since the theoretical $A^{b,c}_{FB}$ values may depend in a non-linear way on the ϵ parameter, the likelihood curves obtained from the χ^2 fits will not follow Gaussian statistics.

Model	ϵ TeV^{-2}	Λ^- TeV	Λ^+ TeV
LL	$0.0002^{+0.0066}_{-0.0070}$	8.49	8.60
RR	$-0.1608^{+0.1650}_{-0.0382}$	2.16	5.83
VV	$0.0011^{+0.0059}_{-0.0063}$	8.54	9.73
AA	$0.0003^{+0.0043}_{-0.0043}$	10.96	10.96
LR	$-0.0309^{+0.0453}_{-0.0412}$	3.28	4.40
RL	$0.1016^{+0.0465}_{-0.1102}$	5.43	2.47
V0	$0.0001^{+0.0050}_{-0.0050}$	10.05	10.18
A0	$0.0174^{+0.0433}_{-0.0335}$	5.40	3.62

Table 6.4: Fitted values of ϵ and 95% Confidence Limits on the scale, Λ, for constructive(+) and destructive (-) interference with the Standard Model, for contact interaction models discussed in the text. This is calculated from all $b\bar{b}$ and $c\bar{c}$ results with centre of mass energies between 183 and 207 GeV.

Therefore the errors assigned to ϵ may vary between the different fits shown in tables 6.5-6.8 also in a non-Gaussian way.

6.5 Possible Improvements in the Analysis

There are two areas in which the asymmetry measurements could possibly be improved. Firstly, it might prove possible to improve the purity of the charge direction assignment. Prompt leptons information could be used to the information coming from the jet charge. It would however require the correlation of the two methods to be understood. Secondly, the performance of the b-tag could be improved for the A^b_{FB} analysis. An obvious way to attempt this could be to use a NN technique as in the $c\bar{c}$ section, thereby accounting for the correlations between the variables. Lepton information could also be included.

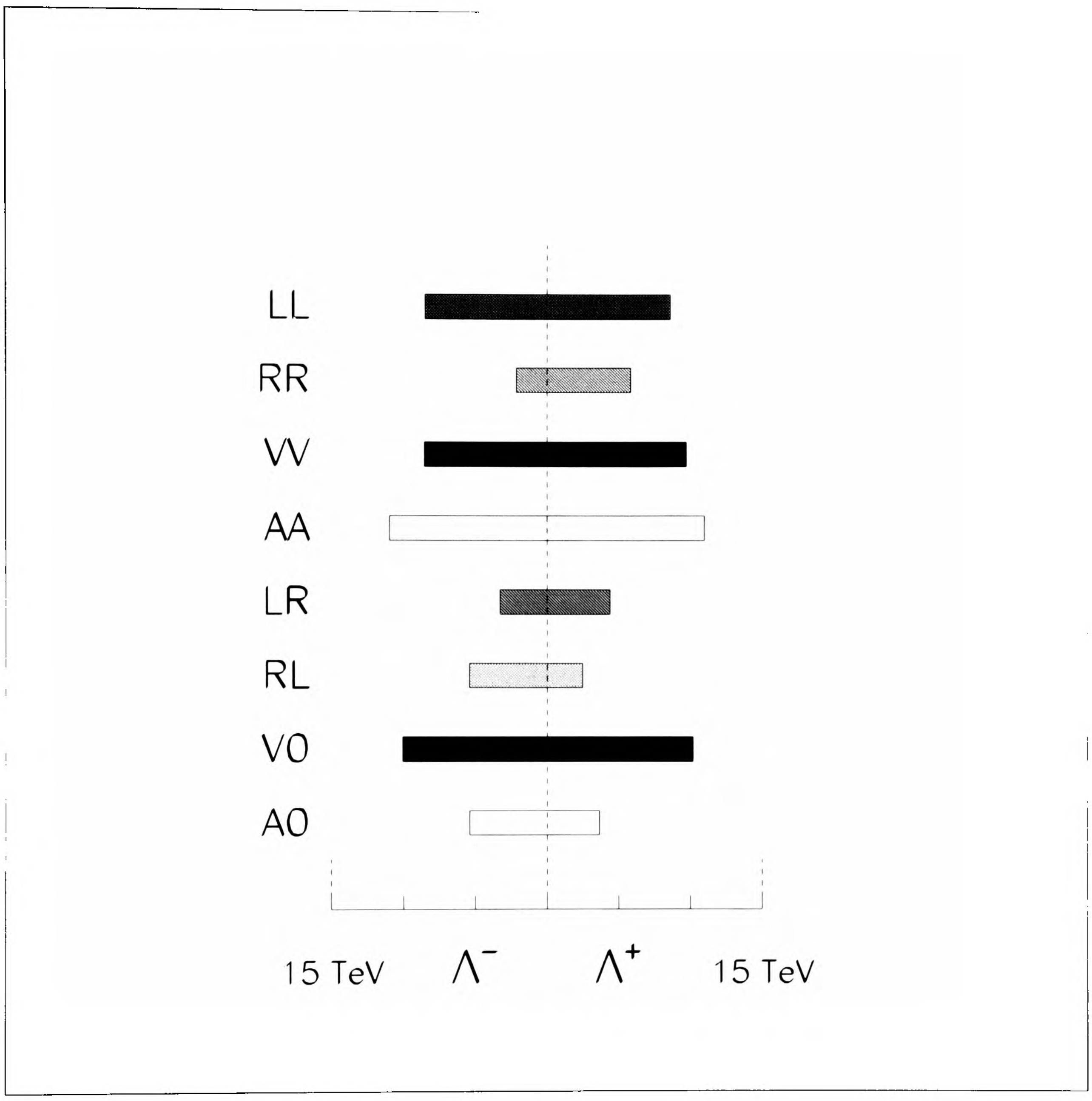

Figure 6.3: Graphical display of the excluded values for the scale Λ for each model (95% CL). Positive (negative) values denote constructive (destructive) interference with the SM. This is calculated from all $b\bar{b}$ and $c\bar{c}$ results with centre of mass energies between 183 and 207 GeV.

Model	ϵ TeV^{-2}	Λ^- TeV	Λ^+ TeV
LL	$-0.0023^{+0.0084}_{-0.0084}$	7.37	8.28
RR	$-0.1470^{+0.1416}_{-0.0468}$	2.18	5.60
VV	$-0.0055^{+0.0086}_{-0.1360}$	2.57	9.39
AA	$-0.0015^{+0.0052}_{-0.0055}$	9.04	10.41
LR	$-0.0429^{+0.0555}_{-0.0504}$	2.90	4.34
RL	$0.1029^{+0.0547}_{-0.0925}$	5.35	2.38
V0	$-0.0016^{+0.0060}_{-0.0060}$	8.72	9.79
A0	$0.0256^{+0.0331}_{-0.0362}$	4.95	3.67

Table 6.5: Fitted values of ϵ and 95% Confidence Limits on the scale,Λ for constructive(+) and destructive (-) interference with the Standard Model, for contact interaction models discussed in the text. This is calculated from R_b results alone from centre of mass energies between 183 and 207 GeV.

Model	ϵ TeV^{-2}	Λ^- TeV	Λ^+ TeV
LL	$-0.1715^{+3.2346}_{-2.8916}$	0.45	0.44
RR	$-0.0831^{+7.1562}_{-6.9898}$	0.30	0.30
VV	$0.2163^{+0.2902}_{-0.1816}$	4.36	0.99
AA	$0.1447^{+0.4068}_{-0.1486}$	0.41	0.50
LR	$-0.0367^{+0.1037}_{-0.1037}$	2.28	2.80
RL	$0.0325^{+0.1636}_{-0.0874}$	3.09	2.01
V0	$-0.1242^{+2.2674}_{-2.0224}$	0.54	0.53
A0	$0.0113^{+0.0758}_{-0.0682}$	3.24	2.82

Table 6.6: Fitted values of ϵ and 95% Confidence Limits on the scale,Λ for constructive(+) and destructive (-) interference with the Standard Model, for contact interaction models discussed in the text. This is calculated from A^b_{FB} results with centre of mass energies between 183 and 207 GeV.

Model	ϵ TeV^{-2}	Λ^- TeV	Λ^+ TeV
LL	$0.1592^{+9.9230}_{-10.241}$	0.26	0.26
RR	$0.1079^{+13.107}_{-13.304}$	0.23	0.23
VV	$-0.0874^{+0.1398}_{-0.1698}$	1.22	2.98
AA	$-0.0874^{+0.1398}_{-0.1698}$	1.12	4.08
LR	$0.0838^{+0.1411}_{-0.1558}$	2.64	1.88
RL	$0.0206^{+0.1236}_{-0.1373}$	2.32	2.16
V0	$0.0085^{+3.7980}_{-3.8151}$	0.43	0.43
A0	$0.0479^{+0.1011}_{-0.1011}$	3.08	2.29

Table 6.7: Fitted values of ϵ and 95% Confidence Limits on the scale,Λ for constructive(+) and destructive (-) interference with the Standard Model, for contact interaction models discussed in the text. This is calculated from A^c_{FB} results with centre of mass energies between 183 and 207 GeV.

Model	ϵ TeV^{-2}	Λ^- TeV	Λ^+ TeV
LL	$-0.0282^{+6.8747}_{-6.8072}$	0.308	0.307
RR	$-0.0181^{+7.4652}_{-7.4289}$	0.296	0.296
VV	$0.0150^{+0.0798}_{-0.0484}$	4.343	2.971
AA	$-0.04^{+0.601}_{-0.682}$	0.015	0.011
LR	$-0.0415^{+0.0885}_{-0.0664}$	2.611	2.773
RL	$0.0101^{+0.1602}_{-0.0744}$	3.023	2.143
V0	$-0.0658^{+4.8744}_{-4.7351}$	0.371	0.370
A0	$0.0238^{+0.0823}_{-0.0762}$	2.35	2.80

Table 6.8: Fitted values of ϵ and 95% Confidence Limits on the scale,Λ for constructive(+) and destructive (-) interference with the Standard Model, for contact interaction models discussed in the text. This is calculated from A^b_{FB} and A^c_{FB} results with centre of mass energies between 183 and 207 GeV.

6.6 Conclusions

6.6.1 A_{FB}^b measurement

The A_{FB}^b has been measured and found to be in good agreement with the predictions of the Standard Model. The Q_{FB} binning technique has enabled the error on the measurements to be reduced with respect to the unbinned method, thereby allowing a more precise test of the SM predictions.

6.6.2 C tagging and the A_{FB}^c measurement

A procedure for tagging c events using a NN has been developed. The performance of the resulting c tag has made it possible to measure A_{FB}^c. A_{FB}^c has been measured at several LEP2 energy points and found to be in good agreement with the predictions of the Standard Model.

6.6.3 Contact Interactions

The A_{FB}^b and A_{FB}^c measurements performed in this thesis together with DELPHI R_b measurements, have been used to put limits on physics beyond the Standard Model in the form of Contact Interactions. The results show that there is no indication for physics beyond the SM at the energies the measurements were performed, and give limits for new physics in the TeV range.

Appendix A - The JETNET program and its use

The JETNET program uses the following function as its separating function:

$$F(x_k) = g[\frac{1}{T}\sum_k w_k x_k + \theta] \tag{6.1}$$

where T is the temperature setting the gain of $g(x)$, w_k are the weights for variable k, θ is the threshold , and $g(x)$ is the non-linear neuron transfer function, given by:

$$g(x) = \frac{1}{1 + \exp(-2x)}. \tag{6.2}$$

In the minimization process w_k and θ are varied. T is a constant set to 1.

A given set of values of the parameters w_k and θ defines the function $F(x_k)$. The aim of the NN training is to find values for w_k and θ such that for the signal events the value of $F(x_k)$ would be 1 and for background events the value of $F(x_k)$ be zero. In order to do this the NN starts with random values for these parameters and changes them through a procedure that is called the back-propagation learning process. In order to know by how much to change these parameters we evaluate the gradient of E, which is also known as the cost. A step in w_k is given by:

$$\Delta w_k = -\eta \frac{\partial E}{\partial w_k} \tag{6.3}$$

where

$$E = \frac{1}{2} \sum_{\mathrm{p}} (\mathrm{o} - \mathrm{t})^2 \tag{6.4}$$

where o and t are the obtained and target(0 for background and 1 for signal) values of the NN, p is the number of events and η is called the learning rate.

The Back-propagation Learning Algorithm

The procedure in which the weights and thresholds are found is through the minimization of the cost ,E. The actual value obtained from the NN depends on the discriminating power of the input variables. The minimization(or training) is done with respect to the weights and thresholds. The weights are changed by an amount computed from the gradient. The training is controlled by the learning strength parameter η. In each updating step of the weights the gradient is multiplied by η which is given a value of 0.2 in this analysis. This can be seen in equation 6.3.

In the training procedure the NN is given a set of variables which form a multi-dimensional space. The weights and thresholds are varied in order to find a set of functions with the greatest separation of signal and background or, expressed in a more graphic way in a 2 dimensional case, to find curves passing through regions of maximum signal and minimum background events.

There are a few practical implementation issues that are of interest :

- Number of layers: Most classification tasks can be performed with one or two hidden layers. However, experience with the NN showed that using more layers makes the output distribution more smooth. Therefore in this analysis a NN with 4 layers was used. Equation 6.1 shows a NN set up with only input and output layers. The 4 layers set up is achieved by substituting equation 6.2 instead of x_k. This has to be done twice for the 4 layers case.

- Initial weight values(w_0): The weights are initialized at random.

- Updating frequency: The simple approach is to update the weights after the complete data set is read. This requires many training cycles. An alternative approach, used in this analysis, is to update the weights after a small subset of patterns, 100 in this case. This is a much faster approach.

The learning procedure includes two event samples. One sample is used for learning and the other sample is used for testing. The number of training cycles is determined by the value of the cost. Through the training procedure the cost values decreases until it stabilizes at some value which is the point for the end of training. The role of the testing sample is to check that the separation obtained in the learning sample is valid for an independent set of events and also to check the point for the end of training.

Appendix B - Errors and limits

The ϵ value was obtained by integrating under the likelihood curve, $\mathcal{L}(\epsilon)$, obtained from the χ^2 fits using:

$$\mathcal{L}(\epsilon) = \exp - \frac{1}{2}\chi^2(\epsilon) \tag{6.5}$$

from -∞ to ϵ such that the integrated area would amount to 50% of the total area.

The uncertainties on ϵ were also obtained by integrating under the likelihood curve. The negative error on ϵ, σ^-, is obtained by first integrating from -∞ to ϵ_{n68} such that the integrated area would amount to 16% of the total area. The error than is calculated using: $\sigma^- = |\epsilon - \epsilon_{\mathrm{n68}}|$. The positive error on ϵ, $\sigma+$, is obtained by first integrating from - ∞ to ϵ_{p68} such that the integrated area would amount to 84% of the total area. The error is calculated using: $\sigma+ = |\epsilon - \epsilon_{\mathrm{n68}}|$.

95% confidence level(CL) limits on Λ are obtained by integrating under the likelihood curve. Λ^- is obtained by integrating in the region of $\epsilon < 0$ from - ∞ to $-\epsilon_{\mathrm{neg}}$ such that the integrated area would amount to 5% of the total negative area. Λ^+ is obtained by integrating in the region of $\epsilon > 0$ from 0 to ϵ_{pos} such that the integrated area would amount to 95% of the total positive area. The Λ values are obtained using $\Lambda = \frac{1}{\sqrt{\epsilon}}$.

References

[1] P.B. Renton. Electroweak Interactions C.U.P (1990).

[2] Proceeding of the School For Young High Energy Physicists. RAL-TR-2001-016

[3] Halzen and Martin. Quarks and Leptons

[4] G 't .Hooft *Renormalizable Lagrangians for massive Yang-Mills fields.* Nucl. Phys. **B35** (1971) 167

[5] Particle data group(PDG) booklet. K.Hagiwara et al., Physical Review **D66** 010001, 2002.

[6] C.Jarlskog, CP violation, (World Scientific)

[7] S.Stone, *Weak decays, CKM and CP violation*, Hep-ph 9904350(1999)

[8] C.Peterson, D. Schlatter, I. Schmitt and P.M. Zerwas, Phys. Rev **D27** (1983) 105.

[9] DELPHI Collaboration (P. Aarino et al). *The DELPHI Detector at Lep.* Nucl. Instr. and Meth. in Phys. Res **A303** (1991) 233-276

[10] DELPHI Collaboration. *Performance of the DELPHI Detector.* Nucl. Inst. and Meth. **A378**(1996) 57.

[11] DELPHI Collaboration. *The DELPHI silicon tracker at LEP2.* Nucl. Inst. and Meth. Volume 412, 2-3,(1998), 304-328.

[12] M.Feindt, C.Kreuter, O.Podobrin. *ELEPHANT reference manual.* DELPHI 96-82,1996.

[13] H. de Boeck, G.R Wilkinson. *MUFLAG : a framework for muon identification.* DELPHI 93-13, 1993.

[14] F. Stichelbaut, G.R Wilkinson. *Performance of the muon identification in DELPHI for the 93 and 94 data.* DELPHI 95-140, 1995.

[15] DELPHI Collaboration. *THE DELPHI trigger system at LEP2 energies.* Nucl. Inst. and Meth. A515(2003) 782-799.

[16] *DELPHI data analysis program (DELANA) user's guide.* DELPHI 89-44. 1989.

[17] D*ELSIM: DELPHI event generation and detector simulation user's guide.* DELPHI 89-67, 1989.

[18] T. Sjostrand, L. Lonnblad, S. Mrenna, P. Skands, Pythia 6.2 Physics and Manual. hep-ph/0108264

[19] T. Sjostrand, M. Bengtsson, *The LUND monte carlo for jets fragmetation and e^+e^- physics: jetset version 6.3.* Comp. Phys. Commun. **43** (1987) 367.

[20] M.Elsing et al . *Changes in the tracks reconstruction to recover from the TPC sector 6 failure*, DELPHI internal note 2001-004 TRACK 95

[21] *B Tagging in DELPHI at LEP.* Eur.Phys.J. C32(2004),185-208.

[22] C. Peterson, T. Rognvaldsson, *The JETNET manual.* CERN-TH 7135/94. 1993

[23] E.Eichten, K. Lane and M. Peskin, Phys. Rev. Lett. **50** (1983) 811.

[24] H. Kroha. Phys. Rev. **D46** (1992) 58.

[25] F.Cossutti, A.Tonazzo, F.Mazzucato *REMCLU: A package for the reconstruction of electromagnetic clusters at LEP2.* DELPHI 2000-164, 2000.

[26] D. Bardin et al. *ZFITTER. v.6.21. A semi-analytic program for fermion pair production in e^+e^- annihilation*, DESY 99-70-hep-ph/9908433.

[27] *Measurement of the A^b_{FB} in hadronic Z decays using a jet charge technique.* CERN-EP/98-189

[28] LEP Electroweak working group. http://lepewwg.web.cern.ch/LEPEWWG/

[29] DELPHI collaboration. Measurement of the partial decay width R_b with the DELPHI detector at LEP. DELPHI 95-115. CONF 41, 1996.

[30] *A Measurement of the cross section ratio R_b and the forward-backward asymmetry A^b_{FB} for bb events with the DELPHI detector at LEP.* DELPHI 2001-095

CONF 523, 2001.

[31] M*easurement of* R_b, A^b_{FB} *and* A^c_{FB} *in* e^+e^- *collisions at 130 189 GeV.* CERN-EP/99-170, 1999.

[32] A Denner et al. *Electroweak radiative corrections to* $e^+e^- \rightarrow WW \rightarrow 4$ *fermions in double-pole approximation: The RACOONWW approach.* Nucl. Phys. **B587** (2000) 67.

[33] W.Placzek et al. W *pair production with YESWW/KoralW*, hep-ph/0012094, 2000.

[34] D. Jeans. D.Phil thesis. *A study of* $e^+e^- \rightarrow W^+W^-$ *at centre-of-mass energies between 161 and 209 GeV.* Oxford University, 2001.

[35] ARIADNE. LU-TP 88-5,1988.

[36] CERN Yellow Book. "Physics at LEP2 " Volume 1, CERN 96-01.

[37] kk2f Generator. hep-ph/9912214.

[38] F.Cossutti et al, *Improvements to SKELANA for version 2.0.* DELPHI 99-175, 1999.

[39] OPAL Collaboration. Eur.Phys.J.C33:173-212,2004.

[40] LEP2FF/02-03